Mapping Myocardial Structure-Function Relations with Cardiac Diffusion and Strain MRI

by

Jiangang Dou

B.S., Applied Physics, Wuhan University, 1994
M.S., Biophysics, Tsinghua University, 1997

SUBMITTED TO THE HAVARD-MIT DIVISION OF HEALTH SCIENCES AND TECHNOLOGY AND THE DEPARTMENT OF NUCLEAR ENGINEERING IN PARTIAL FULFILLMENT OF THE REQUIREMENTS FOR THE DEGREE OF

DOCTOR OF PHILOSOPHY IN RADIOLOGICAL SCIENCES
AT THE
MASSACHUSETTS INSTITUTE OF TECHNOLOGY

SEPTEMBER 2002

Signature of Author: .....
Harvard-MIT Division of Health Sciences and Technology
and Department of Nuclear Engineering
August 15, 2002

Certified by: .....
Van J. Wedeen
Associate Professor of Radiology at Harvard Medical School
Thesis Supervisor

Certified by: .....
David G. Cory
Professor of Nuclear Engineering
Thesis Reader

Accepted by: .....
Jeffrey A. Coderre
Associate Professor of Nuclear Engineering
Chairman, Department Committee on Graduate Students

Accepted by: .....
Marsha L. Gray
Edward Hood Taplin Professor of Medical and Electrical Engineering
Co-Director, Harvard-MIT Division of Health Sciences and Technology

Mapping Myocardial Structure-Function Relations with Cardiac Diffusion and Strain MRI

by

Jiangang Dou

Submitted to Harvard-MIT Division of Health Sciences and Technology and Department of Nuclear Engineering on August 15, 2002 in Partial Fulfillment of the Requirements for the Degree of Doctoral of Philosophy in Radiological Sciences

Abstract

The myocardial structure-function relation is the key to understand the functional design of the ventricular myocardium. While the function of myocardial fibers has been extensively studied, the recently observed laminar organization (sheets) of myocardial fibers is not well understood. This thesis establishes noninvasive MRI methods, registered cardiac diffusion and strain MRI, to acquire information about myocardial sheet structure and myocardial strain under identical *in vivo* conditions, and thus defines the functional role of myocardial sheets. This methodology solves limitations of existing methods that require postmortem dissection, and can be applied to living humans at multiple time horizons in the cardiac cycle.

To establish valid MRI methods to map myocardial structure, we present a new method for diffusion MRI in the beating heart that is insensitive to cardiac motion and strain. Using phantom and *in vivo* validations, we demonstrate that this method addresses the problem of motion sensitivity of diffusion MRI in the beating heart. We also map myocardial sheet and fiber structure during systole in normal humans and find evidence that sheet architecture undergoes remarkable changes during contraction.

To establish valid MR methods to quantify myocardial strain, we present a new 3D phase contrast strain imaging using single-shot 3D EPI. Compared to previous phase contrast 3D strain methods, the new method realizes potential sensitivity of phase contrast EPI. It significantly improves image quality regarding noise and artifact, requires much shorter acquisition time, and can be quickly and automatically processed without operator supervision. Following validation using a strain phantom, we demonstrate the validity of our 3D single-shot strain method in healthy *in vivo* human heart and brain.

Using these methods, we acquire registered diffusion and strain MRI to provide quantitative maps of myocardial structure-function relations in living humans. From these quantitative maps, we are able to define for the first time accurate images of the functional role of myocardial sheets. We find that myocardial sheets contribute to ventricular thickening through all three cross-fiber strain components: sheet shear, sheet extension, and by previously undocumented sheet-normal thickening. Each of these mechanisms demonstrates remarkable spatial non-uniformity as well as inter-subject variability. In all cases, the contributions to thickening of fiber strains are small. Sheet function in normal humans is found to be heterogeneous and variable, contrasting with the previously demonstrated uniformity of fiber shortening. Future studies on myocardial structure-function relations must investigate the causes and extent of such heterogeneous properties of the myocardium. This thesis shows that MRI is a valid and effective tool for noninvasive study of myocardial mechanical function in humans.

Thesis Supervisor: Van J. Wedeen, M.D.
Title: Associate Professor of Radiology at Harvard Medical School

Acknowledgements

I am grateful for the past five years of my Ph.D. study at MIT and Harvard. The excellent education and research environment in the two institutes has benefited me a lot, which I can not express in words. All I want to say is that the five years study constitutes the most precious wealth in my life.

I would like to express my sincere gratitude to my advisor Professor Van Wedeen. His extraordinary insightful and inspiring guidance, his continuous support and encouragement, are indispensable to the accomplishment of this thesis. He cultivates my appreciation for sciences, and shows me through his own life how to be a researcher for truth. I also thank his wife Dr. Lauren Abbate for her understanding of my frequent calls for Van.

I thank Dr. Wen-Yih Isaac Tseng. His patient teaching and inspiring guidance at the beginning of this thesis and his continuous support thereafter are indispensable to the success of this thesis.

I thank my colleague Dr. Timothy Reese. His professional pulse programming and technical support is an indispensable part for the success of this project. I also appreciate his lecture that familiarizes me with the MR machine and his guidance on my technical writing.

I thank Professor David Cory, my academic supervisor at MIT and thesis committee member. His support and supervision in the past five years has been indispensable to the completion of my thesis. His professional knowledge on MR engineering is always respectful and inspiring to learn from.

I thank Professor Sow-Hsin Chen, my thesis committee member. His teaching on quantum theory forms the foundation of my knowledge on NMR. His continuous support and guidance is indispensable to the success of my thesis.

I thank Professor Bruce Rosen for his warm support and his teaching on MRI.

I thank Dr. David Tuch and Dr. Mette Wiegell for their warm helps during my study.

I thank my parents, their endless love and support is the greatest inspiration for me to finish this thesis.

This work is supported by NIH 1RO1-HL56737 and by American Heart Association Established Investigator Grant EIG9740208N.

Contents

List of Figures

List of Tables

Chapter 1

Introduction

1.1 General Introduction

The heart is a sophisticated organ that can continuously pump blood for 70 years or more at a rate varying from 5 to 35 liters/min in humans. Because of its importance to human health, the heart has been extensively studied. The most important tissue of the heart is the myocardium, which provides the mechanical force for the heart to pump blood. The myocardium is an electromechanical syncytium of cardiac muscle cells (myocytes) which resemble ellipsoid cylinders with a major axis dimension of 10 to 20 μm and a length of 80 to 100 μm. Myocytes insert end to end and each is connected with several others to form a complex 3D network of myofibers, which is coupled by another network of collagen and other extracellular matrix proteins. When electrically stimulated during a heartbeat, the muscle fibers shorten and develop tension along their axes. This causes the heart to contract so that the ventricular wall thickens and the blood is pumped. Cardiac mechanical functions, from the myofibers and cellular issues to the global pressure-volume relationship, have been extensively studied. However, the picture of how the system is mechanically integrated, which is essential for a complete understanding of the heart's physiological functions, is still unclear. To understand how the system is mechanically integrated, macroscopic studies of myocardial structure-function relations are required.

The study of myocardial structure has been carried on for several hundred years, but the work on relating structure to function has been carried out mainly in the past several decades. Progress, has been slow due to the complexity of the myocardial structure and also to technical difficulties involved in the study. In the past, the myocardium was viewed as a continuous structure composed of a 3D network of fibers. It was only within the last 10 years that

investigators began to realize that the myocardium is actually organized as a laminar hierarchy of myocardial fibers. Accordingly, in earlier decades, the study of myocardial structure-function relations was mostly focused on the fiber functions. Only recently have researchers begun to explore the functional role of myocardial sheets. The largest difficulty in studying myocardial structure-function relations is the registration of myocardial structure with its functional data. In most studies, functional data, such as myocardial strain, can be obtained *in vivo* either by invasive or by noninvasive methods; however, structural data normally can only be obtained by the invasive histological method under non-physiological conditions, which may cause tissue distortion and compromise the reliability of data registration. In addition, the traditional histological method is invasive, complex, and lab-intensive, and the scope of its investigation is limited as a result. To study functions of the newly discovered myocardial sheet architecture, such hurdles are most obvious, since defining sheet structure is much more difficult than defining fiber orientations. In order to perform more reliable and insightful studies of myocardial structure-function relations, new innovative methods that can overcome the above technical difficulties needs to be developed. MRI is a promising tool for this purpose. It is noninvasive and capable of obtaining structural and functional information under the same physiological conditions. Moreover, it is efficient and easy to perform. This thesis will explore and establish innovative MRI techniques for the purpose of studying myocardial structure-function relations. Specifically, we will focus on the investigation of the new paradigm of myocardial structure-function relations – the functional role of the myocardial sheets.

This chapter reviews previous research and progress relating to the understanding of myocardial structure and functions, and also introduces basic principles of MRI to be used in the study of myocardial structure - function relations.

1.2 Myocardial Architecture

The understanding of myocardial architecture has come a long way since the 17th century, when people first began to recognize that the heart is an organ with a very complex architecture of myocardial fibers. This complex structure has attracted the interest of many investigators, who have made great efforts to understand this mystery over the past 400 years. The following sections will review the extensive historical work on myocardial architecture.

1.2.1 The era of fibers

The exploration of myocardial architecture started from the observation of the myocardial fiber pathway. As early as 1664, Stensen first observed that the ventricular muscle had a helical course (1). Five years later, Lower further stated that the most superficial subepicardial fibers invaginated the apex and became subendocardial or trabecular (2). In 1749, Senac carried out more extensive studies and found that though the inner and outer fibers were organized in helical fashion, the fibers at midwall were most circumferential (3). These original ideas on fiber pathways incurred further investigations. In the 19th century, more progress was made. In 1849, Ludwig found that any block of the heart wall extending from the pericardium to the endocardium was composed of fibers with smooth transition of the orientations across the wall (4). He also stated that the midwall fibers formed a cylinder and the outer wall fibers connected to the inner wall fibers at the apex as well as base in a figure-eight fashion. These ideas were then integrated by Pettigrew into his work in 1864 (5). Based on his study, Pettigrew proposed a new principle of the fiber arrangement based on his study: that the fibers of the ventricular wall could be separated into seven layers, with fibers of each layer having a different direction. In the three outer layers, fibers ran in spiral fasion from left to right downwards, with gradation of fiber pitch across the wall. The fourth layer was at midwall and consisted of circumferential fibers. In the three inner layers, fibers ascended in the reverse direction as a balance to the outer layers. The outermost and innermost layers were continuous at the apex, the second and the sixth were continuous somewhat above the apex, and the third and fifth layers were at a still higher level. In 1891, Krehl proposed a simple model that explained the features of the fiber organization described by Ludwig and Pettigrew. In his model, he systematized the ventricular fibers as two compartments: a myocardial circular collar in the middle layer, and the inner and outer oblique fibers lying on a nested set of virtual toroidal shells (6).

In the 20th century, anatomists tried to establish better ways to dismantle the heart so as to reveal the myocardial fiber architecture in more detail. Two complementary approaches were developed for this purpose. The first was blunt dissection of the heart on a large scale in the belief that the myocardium was composed of a few distinct muscular bundles, and assumed that individual bundles can be revealed by tearing the muscle along the plane of minimum resistance. The other method was the micrometric method for through-wall blocks, which focused on observing orientations of fibers at each location by histology of serial sections. By systematically

sampling the tissue blocks over the left ventricle, 3D fiber pathways could be reconstructed based on reasonable assumptions of the ventricular geometry.

The blunt dissection method was first used by MacCallum in 1900 (7). He dissected macerated embryo porcine hearts by following the main paths of fibers through the ventricular wall, ripping side branches, and unrolling the myocardium into separate large masses of muscle tissue. In 1911, Mall used this method on human hearts and described a series of complex spirals and loops of muscle within the ventricular mass (8). He separated four main groups of fibers: the superficial and deep bulbo-spiral bands and the superficial and deep sino-spiral bands. Mall's and MacCallum's concept of myocardial organization visualized the unrolled heart muscle as a skeletal muscle of tendinous origin that inserted into the valve rings, which was easy to accept and also in some sense realized the abstract models developed in the previous century.

However, in 1956, the method of blunt dissection was challenged by Lev and Smikins (9). Using a modification of Mall's method, they were unable to identify the cleavage between superficial and more deeply located fasciculi, and they also found no evidence of distinct muscle layers separated by fibrous tissue. In 1965, Grant offered another challenge to the blunt dissection method (10), indicating how subjective judgments of the dissector might influence the distribution of apparent muscle bundles. He showed that fiber matrix could be partitioned into different bundles depending on the orientation of the tearing forces applied, so he concluded that the results of blunt dissection were not reproducible, and the concept of separate muscles constituting the ventricular mass was untenable. Recognizing these problems, in 1973 Torrent-Guasp improved the blunt dissection technique, which had revealed only the individual muscle pathways in the principal fiber direction (11). He claimed that his technique was objective and reproducible. Using this improved protocol, he was able to show successive layers with a raked turban-like appearance within the ventricular myocardium, which resembles Pettigrew's principle of fiber rearrangement.

The other approach, the micrometric method for through-wall blocks, was first used by Hort in 1957 (12). His procedure was to make serial frozen sections parallel to the wall surface, then perform microscopic examinations to quantify local fiber orientations. His results on the fiber orientation from various sites of the heart wall confirmed the mid-19th century idea of continuous transition of fiber angle across the wall. Ten years later, Streeter performed a more systematic quantification of the fiber orientation (13-15). He measured fiber orientations on

parallel and rotated sections of the through-wall blocks, which were sampled from different latitudes and longitudes of the wall between the base and apex of the left ventricle. With the measured data, he reconstructed 3D orientations of the fiber pathways around the heart, and found that principal fiber pathways tend to follow a geodesic path on the planes parallel to ventricular wall surface. In addition, the fibers burrow into the wall in a continuous fashion such that they make a figure-eight return to the equator (Fig. 1.1). His results vindicated Krehl's Triebwerk model of the heart wall which held that the ventricular wall can be imagined as a nested set of toroidal shells centered on the midwall on which the fiber pathways run in a helical pattern from epicardium to endocardium.

In Streeter's work, at each location of the wall he decribed the 3D orientation of the fiber axis using three projected angles in orthogonal planes (tangential, longitudinal, and traverse), i.e., the helix angle, the declination angle, and the traverse angle, respectively (16, 17). Declination and traverse angles were combined to give the imbrication angle, which represents the rate of change in wall depth for a given fiber pathway. The imbrication angle determines how steeply a fiber path burrows into the wall. Using these angle descriptions, Streeter found that the fiber helix angle, namely the angle of fiber on the local epicardial surface with respect to local latitude, varies smoothly from approximately -90° at the epicardial surface, through 0° near the midwall, to approximately 90° towards the endocardium (Fig. 1.2). The imbrication angle varies from approximately +15° near the base, through 0° at the equator, to almost -15° near the apex.

Based on his study, Streeter regarded the myocardium as a well-ordered fiber-wound continuum of interconnecting muscle fibers, and refuted the concept of distinct bands of the heart muscle that had been claimed by many anatomists for decades. According to his model, elastic behavior of the myocardium can be approximated as transversely isotropic. The fiber is viewed as a rod structure in a lubricated near-parallel array in the vicinity (a slippery-skinned rod), carrying only axial tension and reacting to a pressure gradient laterally. Streeter's is a classic work in the history of understanding the myocardial fiber architecture. Although his approach did not produce a comprehensive documentation of the fiber pattern over the entire ventricle, it gave a clear picture of the three main characteristics of the myocardial fiber architecture: (1) fiber orientations are generally tangential to the endocardial and epicardial surfaces, (2) fiber paths are in a helical pattern, and the helices can be approximately described as geodesics lying on a family of nested toroidal surfaces, (3) fiber angle changes smoothly in a way that

corresponds to a transition from a left-handed helix on the epicardium to a right-handed one on the endocardium. The model described by Streeter lays the groundwork for the modern concept of the fiber architecture, and was widely implemented in numerous models of ventricular wall mechanics in the following several decades.

1.2.2 The era of sheets

However, in recent years the concept that myocardium is a 3D continuum with uniform branching myocytes has been challenged, as people began to realize that there may be a more complex structural organization of the myocardium, which in gross appearance is evidenced by those regularly arranged gaps observed in myocardium samples. In fact, the existence of such regularly arranged gaps in both the right ventricle (RV) and LV walls in longitudinal and transverse sections has been reported since the late 1800s. In transverse sections, these gaps can be recognized in the appearance of a feathering or pinnation pattern converging toward the midwall (Fig. 1.3). Hort described these gaps as systematically ordered anastomosis-poor sections in the myocardium, which may provide delicate regulation of the movement of muscle fibers with one another (18). Though thesegaps had been observed for a long time, they had never been recognized as an indispensable part of the myocardial architecture, and gained little study interest until Caulfield and Borg published their significant works on the microstructure of the myocardium.

In 1979, using a scanning electron microscope (SEM) at high magnification (1000x to 10,000x), Caulfield and Borg observed a hierarchy of the connective tissue in the myocardium (19). They noted that myocytes were connected to adjacent myocytes by numerous bundles of radial collagen fibers. These collagen cords were quite straight and have a relatively uniform circumferential distribution. They also observed that a connective tissue meshwork surrounded groups of three or more myocytes, and that the enclosed myocytes were connected to the encompassing network by numerous short and straight collagen fibers. However, the adjacent bundles of myocytes were only loosely coupled by sparse and relatively long collagen fibers.

In 1995, using a lower magnification (100x to 1000x) SEM, LeGrice described the relationship between the 3D arrangement of myocytes and the extracellular connective tissue matrix in dog hearts (20). He found that the myocardium consists of an ordered laminar organization, with myocytes arranged into branching sheets that are "stacked" upon one another

from apex to base, and twisted through the ventriclular wall from epicardium to endocardium. Individual sheets of myocytes are approximately four cells thick and are surrounded by an extensive meshwork of connective tissue. Within each sheet, myocytes are coupled tightly to each other by dense radial collagen fibers, but adjacent sheets are only loosely coupled by long perimysial collagen fibers (Fig. 1.4). The sheet thickness is found to be homogeneous transmurally and at different regions of the ventricle, but sheets appear to be more tightly coupled in the subendocardium as there are increased branching of myofibers between layers in this region. The organization of these microscopic sheets corresponds to the macroscopically visualized cleavage planes on the tissue sections. Based on these findings, LeGrice concluded that the ventricular myocardium is not a continuous structure composed of a 3D network of fibers, but rather a complex anisotropic material with a laminar hierarchy of myocardial fibers.

LeGrice's work constitutes the modern view of myocardial architecture, i.e., myocardial architecture is organized as a laminar hierarchy of myocardial fibers. At any point of the ventricular wall, local myocardial architecture is represented by a stack of sheets composed of parallel fibers, and the orientation of the fibers at each location conforms to Streeter's classic description. The sheet direction is determined by the direction of lateral extent of these parallel fibers. The material symmetry at each location can be defined by three orthogonal axes, paralleling fiber, sheet, and sheet normal vectors, and hence is orthotropic.

1.3 Functional Significance of the Myocardial Architecture

Understanding myocardial structure-function relations is important for interpreting and predicting changes in the diseased heart. Thus, the study of myocardial structure-function relations has long been of interest to researchers. Since Streeter's description of the unique helical fiber orientation, many investigators have proposed various hypotheses to relate myocardial fiber architecture to its functions such as contraction and relaxation. Following is a review about the study of the functional roles of myocardial architecture.

1.3.1 Fiber function – a well-studied kingdom

Fiber function has been studied extensively in the past several decades. Numerous results of animal experiments and computer simulation show evidence that the fiber architecture has two

important functional roles. First, the fiber helical pattern allows transmission of the fiber contraction from the outer wall to the inner wall through transmural coupling of the associated connective tissue. This kind of force transmission results in remarkable cross-fiber shortening in the inner wall, which in turn leads to significant thickening in the radial direction. Second, the fiber helical pattern is the result of a local feedback process to equalize fiber stress and fiber strain across the wall. Equalization of the fiber work load is believed to be the manifestation of physiologically uniform distribution of coronary perfusion and cell metabolism in the wall. The following paragraphs describe the evidence that supports these two hypotheses.

The first hypothesis was enunciated in 1988 by Waldman et al., who first determined 3D myocardial deformation and fiber orientation in the anterior free walls of the LV in seven dogs (21). They measured myocardial deformation by recording motions of implanted radiopaque markers with high-speed biplane cineradiography. The local myocardial 3D strain tensor with respect to end-diastole was then computed from relative displacements of tetrahedrons demarcated by the markers. Hearts were then fixed at end-diastole and sectioned parallel to the local epicardial tangent plane to determine the transmural distribution of fiber directions at the site of strain measurement. Their results showed that, unlike the wide range of fiber orientation ($\approx$180°), the transmural variation of the direction of maximal shortening is relatively small ($\approx$90°). In particular, the directions of fiber and maximal shortening are not substantially different in the outer wall, but are orthogonal to each other in the inner wall. This kind of deviation of maximal shortening direction from the fiber axis indicates that there may be some mechanism other than fiber contraction that participates in this off-line shortening. Waldman proposed two possible mechanisms responsible for this deviation: one is the rearrangement of myocytes, and the other is the shape change in the cross sections of myocytes or the interstitium. As a consequence, the maximal shortening orthogonal to the fiber axis in the inner wall leads to a larger radial thickening due to incompressibility of the myocardium. Waldman's finding indicates that the purpose of the helical pattern of the fiber orientation is to promote inner wall thickening during contraction. However, the accuracy of their data is compromised by the invasive procedures they used (opening the chest and traumatizing the myocardium) to record the wall motion, and also uncontrollable errors arising from *ex vivo* determination of the fiber orientation, such as incompatible physiological conditions and specimen distortion during tissue preparation.

To clarify the significance of the helical fiber pattern relative to the wall thickening in a less invasive way, in 1994 Rademarkers et al. measured 3D myocardial strain on ten closed-chest dogs using a noninvasive NMR tagging technique (22). After strain measurement, the dogs were sacrificed and the fiber orientation at the same site of strain measurement was determined using a dissecting microscope. By recording strain tensors at 20 time points during systole, he statistically compared the correlation between different strain components (fiber shortening, cross-fiber shortening, and in-plane shear) at different regions (endo- and epicardium). The results show that there is strong correlation between fiber shortening on one side of the wall and cross-fiber shortening on the other side. The finding suggests that there is strong coupling of the fiber shortening between the inner wall and the outer wall. Using regression analysis, he also found that epicardial and endocardial cross-fiber shortenings have strong correlation with total wall thickening. These results support the hypothesis that the contractile force of the fiber is carried through the wall via connective tissue coupling from layer to layer. Because fibers in the outer wall (presents a left-hand helix) and those in the inner wall (presents a right-hand helix) are crisscrossing, contraction of fibers in the outer wall exerts exceedingly large cross-fiber shortening (three times the fiber shortening) in the inner wall. As a consequence, spontaneous shortening in fiber and cross-fiber directions leads to a remarkable thickening in the radial direction. The structural basis of the cross-fiber shortening may be either a slippage motion between myocyte bundles (i.e., sheet slippage inducing cellular rearrangement) or anisotropic stretching of the individual myocyte and/or sheet cross sections.

The second hypothesis regarding the functional role of the fiber helical orientation was enunciated by Arts (23). He claims that helical fiber orientation is the result of an adaptive process to equalize fiber stress and sarcomere shortening across the wall. By modeling the left ventricular wall as a thick-walled cylinder composed of 8 concentric shells, he incorporated anisotropic material properties according to classic transmural transition of the fiber orientation. Based on this model, he simulated cardiac contraction and found that, in contrast to conventional models based on isotropy, transmural distribution of stress and strain in the fibers appears to be rather uniform. In computer simulation, he also shows that equalization of fiber stress and fiber strain is achieved by the combination of cardiac torsion and transmural gradation of fiber angle, which effectively levels off the existing transmural difference of segmental shortening. He further hypothesized that the fiber orientation is controlled by the feedback signals, which are

fiber stress, end-diastolic sarcomere length, and sarcomere shortening during ejection (24). With this feedback system set up, a stable final solution for the transmural course of fiber orientation can be achieved after self-correcting iterations. This final solution yields a homogeneous fiber load within ±2%, which is close to anatomical findings of fiber geometry reported in many species.

In fact, the uniformity of fiber work load and fiber strain is supported by many lines of experimental evidence. Transmural distribution of coronary perfusion was found to be uniform within ±10% at rest (25), and became even more uniform during exercise. The difference in cellular metabolism between endocardium and epicardium is also insignificant (26). Waldman, Rademarkers, and Bloomgarden (21, 22, 27) separately measured the fiber shortening in dog hearts using different methods. They found consistent results that fiber shortening is quite uniform across the wall.

The uniformity of fiber stress and fiber strain has potential significance in the evaluation of ventricular function. The contractile function of the heart wall can be indicated by a single active action, i.e., the fiber shortening. Furthermore, myocardial infarction results in imbalance of the fiber shortening and fiber loading. The adaptive process of the myocardium to resume uniformity of the fiber dynamics might closely relate to the process of ventricular remodeling.

1.3.2 Sheet function – mystery still to be revealed

The discovery of the functional significance of sheets starts from a paradox in ventricular inner wall thickening. In the cardiac cycle from end diastole to end systole, the ventricular inner wall undergoes as much as a 40% thickness change, while the length of fiber or sarcomere changes by about 15% (28). Given such an amount of fiber strain, simple calculation based on the conservation of individual myocyte volume yields about 8% thickness change in the cross-fiber direction, equivalent to only about one-fifth of the local thickening at the inner wall. Thus, there must be some other mechanisms that account for the large wall thickening strains at this site. The explanation for this paradox was first described by Hort (12, 18). He counted the number of fibers across the ventricular wall in various contracted and dilated hearts of guinea pigs and dogs, and found that there was a significant difference in transmural fiber number between dilated and contracted walls. Hort also measured the cross sections of the fibers in these walls, and found that fiber cross sections did not change significantly between different states.

Based on these observations, he speculated that the mechanism of this cell number change was due to the distinct gaps or planes found in the myocardium, which provided freedom for fibers to slide on one another laterally. It is then such rearrangement of the fibers that leads to the observed variation in fiber number across the wall.

Hort's hypothesis was further verified by Spotnitz et al. (29). In Spotnitz's experiment, longitudinal sections of the whole wall of rat hearts fixed in differently filled ventricular volumes were examined, and the numbers of fibers across the wall and the fiber density (the number of fibers per unit area) were correlated with wall thickness. The results were consistent with Hort's: the wall thickness associated closely with the number of fibers across the wall, and the decrease in wall thickness was 3 to 4 times greater than the decrease in fiber density. In his study, Spotnitz also illustrated how the gaps or cleavage planes in the myocardium change orientation to accommodate change in transmural fiber number. In thick ventricular walls, these planes generally approached a horizontal orientation, while in thin walls, the planes tilted vertically along the ventricular axis, forming acute angles with the epicardium and endocardium.

In 1995 LeGrice documented that the myocardium was indeed a complex laminar structure (20), and that the spaces between adjacent laminae (or sheets) formed distinct cleavage planes observed on the cut surface of the tissue on the macroscopic scale. He further hypothesized that the slippage motion between adjacent sheets provided an anatomic basis for myocyte (or cellular) rearrangement to occur during systole (30). To prove the hypothesis, he did experiments on canine hearts. He chose two regions where cleavage planes were opposite in orientation, i.e., the anterior free wall and the septum of the left ventricle, and correlated the 3D orientations of the cleavage planes with the myocardial strains measured at the same sites. The myocardial strain was first measured on anaesthetized open-chest dogs by recording the motion of implanted metallic beads using high-speed cineradiography. After strain measurement, hearts were sectioned and 3D cleavage plane (sheet) orientations at the site of strain measurement were determined in three orthogonal planes using a light microscope. Using this method, he found that sheet shears in these two regions were opposite in sign, but both consistently contributed to wall thickening. The amount of wall thickening calculated from the shear amount and the cleavage plane angles at these two regions showed reasonable correspondence to the measured thickening strain. In the inner third of the wall, there was a close match between the planes of maximum shear and the planes of the sheet structure. Based on these results, he concluded that, in the inner

wall of anterior free wall and septum, systolic wall thickening was mostly contributed by the slippage motion between the sheets.

In 1999, Costa et al. further explored the functional role of laminar myocardium (31). Using similar methods to LeGrice's, they measured myocardial end-systolic 3D strains at sites near the apex and base of the canine anterior LV free wall, and also fiber angles and cleavage-plane angles at the sites of strain measurement. Using obtained fiber and cleavage plane angles, they constructed local 3D structural axes of the myocardial laminae, and referred the measured 3D strain to these local "fiber-sheet coordinates." By doing so, they examined the contribution of fiber-sheet strain to wall thickening, and found that transverse shear associated with the reorientation of sheets around the local fiber axis contributes to LV wall thickening and cross-fiber shortening strains, which is consistent with LeGrice's hypothesis. In addition, they also found substantial laminar extension transverse to the fiber axis across the wall, which was another dominate source of radial thickening. Based on these findings, they hypothesized that, in addition to sheet shear, sheet extension is also an important mechanism for ventricular wall thickening. They also suggested that this dual wall thickening mechanism, i.e., sheet extension and sheet shear, may have distinct ultrastructural origins that depend on the hierarchical organization of the extracellular collagen matrix.

The role of sheet function is not completely understood yet, though some progress has been made in recent years. Difficulties in methodology have limited the scope of investigation. Previous studies have been invasive, and also have required complex procedures. Thus, only a few studies have been performed at limited regions of the heart on animals. Whether the above hypothesis works over the whole ventricular wall or over other species, and whether there are any unknown functions of the sheets, are still questions that need further investigation. In order to answer these questions, more efficient and applicable ways of examining myocardial structure-function relations are desired.

1.3.3 Difficulties in the study of myocardial structure-function relations

The study of myocardial structure-function relations is not an easy task. To perform such studies, at least two pieces of information are required, one concerning myocardial structure and the other myocardial deformation. By combining these two sets of data, and analyzing their relationships over different regions of the ventricular wall, some simplified principles about the

mechanical role of the fiber architecture can be revealed, as shown in the review part of the functional roles of the myocardium (Chapter 1.3). One principal requirement for such studies is that the structural information and functional information should be registered, i.e., one needs to obtain these two data sets simultaneously from the same location of the beating heart. Technically, this requirement is extremely difficult to fulfill, because although myocardial function can be measured *in vivo* using invasive or noninvasive methods, fiber architecture can be determined, in most cases, only by dissection and histology. How much the structural information obtained *ex vivo* deviates from *in vivo* situations is not clear, because the condition of the heart when it is in *ex vivo* state is completely different from that of *in vivo* conditions when strain is measurable. Thus, traditional methods of studying structure-function relations cannot provide a reliable way to determine myocardial architecture. Moreover, due to their invasive features, studies of humans are not possible, which greatly limits the scope of investigation.

To overcome the above obstacles, new noninvasive methods are desired that are able to obtain structural information and functional information from human hearts under the same physiological conditions. MRI offers a unique opportunity to perform such tasks. In this thesis, we propose to use diffusion tensor MRI to map myocardial architecture, and to use phase-contrast MRI to map myocardial deformation. By analyzing these data, we will produce quantitative maps of motion patterns of the fibers and the sheets, which will allow us to investigate many questions concerning structure-function relations of the myocardium. For this thesis, we will establish and apply state-of-the-art MRI techniques to explore the intriguing questions of the functional role of the myocardial sheets.

1.4 MRI Methods for Studying Myocardial Structure-Function Relations

Myocardial structure-function relations can be studied using noninvasive MRI techniques. MRI diffusion measurement offers the opportunity to define myocardial structure. MRI strain measurement gives functional information for the myocardium. A combination of these two techniques can help to define myocardial structure-function relations. The following parts review the basic principles of MRI techniques on myocardial diffusion and strain measurement.

1.4.1 Myocardial diffusion measurement

The process of self-diffusion refers to the random translational Brownian motion of molecules in a material (such as liquid). The macroscopic effects of translational Brownian motion are best described by an equation derived by Einstein (32):

$$Dx^2 = 2\,D\,t \qquad (1.1)$$

where Dx^2 represents the mean square displacement of a particle within a given time of observation t, and D represents the diffusion constant, characterizing the mobility of the substance.

Equation 1.1 shows that the mean diffusion path length depends on the length of the observation period t. If the particles experience no barriers during this observation time, the determination of the diffusion coefficient will remain independent of this time t. In this case, the diffusion process is called free diffusion. However, if the particles bounce into barriers during the observation period, i.e. the diffusion path length is limited by the environment, then the apparent path length will be shorter than the one based on the medium viscosity alone. In consequence, the apparent diffusion coefficient will also become smaller; or to put it differently, the value of the apparent diffusion coefficient will depend on the experimental observation time. In this latter case, the diffusion process is called restricted diffusion.

In *in vivo* situations it is often times difficult to determine under which conditions free diffusion or restricted diffusion will be obtained, as the measurement of the diffusion coefficient is affected by other factors such as bulk motion, intracellular streaming, temperature, and magnetic-susceptibility variations (33). Furthermore, the existing hardware will influence the possible experimental diffusion time. Therefore, in relation to *in vivo* experiments the term apparent diffusion coefficient (ADC) is used.

To measure the self-diffusion constant or ADC, normally a molecular label is required so that positional change of molecules can be traced through time. To employ such molecular labels, three major techniques have been developed so far. They are radioactive tracer measurement, neutron scattering spectroscopy, and pulsed gradient NMR. Each technique has different sensitivity to Einstein lengths of molecular diffusion. Tracer measurement is useful for lengths on the scale of millimeters. Neutron scattering is for those on the scale of Angstroms. Pulsed gradient NMR probes diffusion lengths ranging from a few microns to hundreds of microns, which are compatible with the size of cells in biological tissue. Therefore, one

important application of pulsed gradient NMR is to investigate the structural features of cellular organization based on the parallel correspondence between diffusion anisotropy and structure anisotropy.

1.4.1.1 NMR pulsed gradient diffusion measurement

The sensitivity of NMR on molecular motion arises from labeling the molecule using a smoothly varying magnetic field or magnetic gradient field over the sample. In this magnetic field, the individual nuclei of each molecule (hydrogen nuclei of water molecules in most cases) precess with characteristic Larmor frequencies according to their positions. Individual nuclei accumulate precessional phases as they move with molecules due to flow or diffusion motion and experience different magnetic fields during the measurement. In the case of flow, the motion of water molecules is coherent, so the phase memory of the precessing nuclei is conservative, which will result in a phase shift in the readout echo. In the case of diffusion, on the other hand the molecular translational motion is random in nature, so the phase memory of the precessing nuclei is dissipative, which will result in an attenuation of the amplitude of the readout echo. The constant representing the above attenuation process is known as the coefficient of self-diffusion.

The effect of diffusion on the attenuation of echo signals was noticed and discussed by Hahn in 1950 in his classic paper on spin echoes (34). In 1954, Carr and Purcell extended Hahn's idea and proposed a multi-echo method to minimize such a diffusion effect (35). A formal derivation of the diffusion effect on signal attenuation was carried out in 1956 by Torrey, who took the "magnetic flow" approach by adding diffusion terms to the original Bloch equations (1946) so that self-diffusion and flow are represented as a "transport of magnetization" (36, 37). To measure self-diffusion, one can use conventional spin-echo pulse sequence with a magnetic field gradient continuously applied. However, this sequence is found to have a higher noise due to the increased signal bandwidth. To overcome this problem, Stejkal and Tanner proposed a new sequence that uses a pair of pulsed magnetic field gradients, symmetrically positioned around the 180°-refocusing pulse of a Hahn spin echo (38). They also gave a detailed theoretical description of the signal attenuation that generalizes Torrey's equation of the constant-gradient case, and showed that the diffusion coefficient (D) in their sequence is related to the signal attenuation A(TE) / A(0) by:

$$\ln[A(TE) / A(0)] = - \gamma^2 g^2 \delta^2 D (\Delta - 1/3\ \delta) \qquad (1.2)$$

where g is the magnitude of the pulsed gradient, δ is its duration, and Δ is the interval between the pulse pair, i.e., diffusion time.

It is instructive to derive Eq. 1.2 using narrow-pulse approximation, i.e., in the limit of $\delta << \Delta$, for it clearly demonstrates the mechanism for diffusion-induced signal attenuation (39). Assuming pulsed gradients are the only gradients that impose phase shifts on the spins, a spin at position $\mathbf{r}$ will gain a phase shift of $\gamma\delta\mathbf{g}\cdot\mathbf{r}$ after the 90° r.f. pulse and first gradient pulse. This phase shift is subsequently inverted by the 180°y r.f. pulse. After diffusion time Δ, the second gradient pulse is applied. Suppose the spin has moved to position $\mathbf{r}'$ due to molecular translation at the time of second gradient pulse. The net phase shift following this process will be $\gamma\delta\mathbf{g}\cdot(\mathbf{r}' - \mathbf{r})$. The probability for a spin to begin at $\mathbf{r}$ and move to $\mathbf{r}'$ at the time Δ can be described by conditional probability $P_S(\mathbf{r}|\mathbf{r}', \Delta)$ multiplied by function of spin density $\rho(\mathbf{r})$. The echo signal $E(\mathbf{g})$ is then the ensemble average of transverse magnetizations with phase terms $\exp[i\gamma\delta\mathbf{g}\cdot(\mathbf{r}' - \mathbf{r})]$ weighted by $\rho(\mathbf{r})\ P_S(\mathbf{r}|\mathbf{r}', \Delta)$:

$$E(\mathbf{g}) = \int\int \rho(\mathbf{r})\ P_S(\mathbf{r}|\mathbf{r}', \Delta) \exp[i\ \gamma\delta\mathbf{g}\cdot(\mathbf{r}' - \mathbf{r})]\ d\mathbf{r}'\ d\mathbf{r} \qquad (1.3)$$

In the case where the diffusion time Δ is sufficiently long, $P_S(\mathbf{r}|\mathbf{r}', \Delta)$ is independent of starting position $\mathbf{r}$ and depends only on the dynamic displacement $\mathbf{R} = \mathbf{r}' - \mathbf{r}$. The conditional probability P_S for water molecular diffusion in an anisotropic medium can be represented by a normalized Gaussian as a function of $\mathbf{R}$, Δ, and the diffusion tensor $\mathbf{D}$:

$$P_S(\mathbf{R}, \Delta) = (4\pi\Delta||\mathbf{D}||)^{-3/2} \exp[-\mathbf{R}^T\cdot\mathbf{D}^{-1}\cdot\mathbf{R} / 4\Delta] \qquad (1.4)$$

where $||\mathbf{D}||$ is the norm of $\mathbf{D}$, i.e., $||\mathbf{D}|| = (\lambda_{max}\ \mathbf{D}^T\cdot\mathbf{D})^{1/2}$; λ_{max} = the largest eigenvalue of $\mathbf{D}^T\cdot\mathbf{D}$. Substituting Eq. 1.4 in Eq. 1.3, it is easy to see that $E(\mathbf{g})$ is actually the Fourier transformation of the Gaussian $P_S(\mathbf{R}, \Delta)$:

$$E(\mathbf{g}) = \exp[-\gamma^2 \delta^2\ \mathbf{g}^T\cdot\mathbf{D}\cdot\mathbf{g}\ \Delta] = \exp[-4\pi^2\ \mathbf{k}^T\cdot\mathbf{D}\cdot\mathbf{k}\ \Delta] \qquad (1.5)$$

where $\mathbf{k} \equiv (1/2\pi)\ \gamma\delta\mathbf{g}$, the spatial modulation of the magnetization. The echo signal $E(\mathbf{g})$ derived above has neglected the signal attenuation caused by T_2. In practical experiments, diffusion-

induced signal attenuation is measured by the ratio of the signal with diffusion-sensitizing gradients to the signal with null gradients.

It should be noted that Eq. 1.5 is derived under the condition that the pulsed gradient acts like an instantaneous spike, in which the duration of the spike is so short that molecular diffusion during δ can be neglected. In the case of finite δ, the phase term of transverse magnetization would be an integral form of field gradient, namely, $\exp[i\ \gamma\ (\int_0^t \mathbf{g}(t')dt')\cdot\mathbf{r}] = \exp[i\ 2\pi\mathbf{k}(t)\cdot\mathbf{r}]$, instead of $\exp[i\ \gamma\delta\mathbf{g}\cdot\mathbf{r}]$. Equation 1.5 can then be extended as the following form:

$$E(\mathbf{g}) = \exp\left[-\int_0^{\Delta} 4\pi^2\, \mathbf{k}(t)^{\top}\cdot\mathbf{D}\cdot\mathbf{k}(t)\, dt\right] = \exp[-\,4\pi^2\,\Delta\,\langle\mathbf{k}(t)^{\top}\cdot\mathbf{D}\cdot\mathbf{k}(t)\rangle_{\Delta}] \qquad (1.6)$$

where $\langle\ldots\rangle_{\Delta}$ denotes time average over the diffusion time Δ, i.e., $\langle\ldots\rangle_{\Delta} = 1/\Delta \int_0^{\Delta}(\ldots)dt$. In pulsed gradient spin-echo sequence, the time integral of $k(t)^2$ over TE yields $(1/4\pi^2)\ \gamma^2 g^2\delta^2\ (\Delta - 1/3\ \delta)$, which is the attenuation factor of Stejskal-Tanner's equation (Eq. 1.2). It should be emphasized that Eq. 1.6 can be generalized to the diffusion-attenuation effect caused by any time-varying spatial modulation of the magnetization during Δ. The implication of this important principle will be invoked in the next section when the effect of tissue stretch on the MR diffusion measurement is considered.

1.4.1.2 MRI of anisotropic diffusion

In the original description, diffusion is considered a scalar with no preference for direction. However, in a situation where the distance of the barriers differs for the various axes, such as where the diffusion along axis **a** is found to be free while along axis **b** the barriers are close enough to lead to restricted diffusion under the chosen experimental conditions, diffusion anisotropy results. The complete determination of the diffusion characteristics under such conditions requires the determination of the full diffusion tensor of the ADC.

The character of diffusion anisotropy inherent to materials exhibiting organizational anisotropy has been investigated in NMR diffusion experiments (40-43). In biological tissues, water molecules are the most abundant component that gives NMR signals. Thus, MRI measurement of diffusion in biological tissues in general refers to measurement of water diffusion. The ability of MRI methods to measure the self-diffusion coefficient of water molecules was first demonstrated *in vitro* by Wesbey in 1984 (44). By incorporating the paired-gradient Stejskal-Tanner sequence into conventional imaging sequences, MRI images with the

image contrast weighted by the local tissue diffusivity can be obtained. From these diffusion-weighted images, one can compute apparent diffusion coefficients (ADC) of water, and obtain information about tissue pathophysiology complementary to that contained in usual T_1- and T_2-weighted images.

MRI measurement of water diffusion is a unique tool to study structural information of biological samples. In tissues that have a regularly ordered microstructure, such as brain white matter, skeletal, cardiac, and uterine muscles, kidney, and lens, the measured ADC of water is found to vary with tissue orientation (45-51). Specifically, the ADC is found to be greatest when the diffusion-sensitizing gradient is applied along the fiber direction, and smallest when the gradient and fiber directions are perpendicular to each other. The most plausible explanation for this phenomenon is that cell membranes and/or other oriented molecular structures retard water diffusion perpendicular to the fiber tract axis more than water diffusion that is parallel to it. Following this discovery, Moseley et al. (1990) and Douek et al. (1991) carried out studies on nerve fibers and suggested that this diffusion anisotropy could be used to determine the orientation of nerve fiber tracts within brain white matter (52, 53). Their findings have attracted much attention, and since then, diffusion MR imaging has been widely used as a sensitive probe for investigations into structural and functional cellular and interstitial aspects.

To fully define a 3D orientation of the microstructure, a rank-2 diffusion tensor of the ADC in each voxel of the tissue needs to be determined. From the diffusion tensor, one can calculate its three eigenvectors, which can be used to define the three orthotropic axes of the microstucture in study. For this reason, Basser et al. (1994) proposed a new imaging method that uses a series of NMR pulsed gradient spin-echo experiments to compute the diffusion tensor at each voxel (54). This technique is called MR diffusion tensor imaging. The key procedure of diffusion tensor imaging is to acquire six diffusion-attenuated images using six noncollinear diffusion-encoding gradients. Given a set of six attenuated images and one unattenuated reference image, inverse algebra can be applied to solve for the six components of the diffusion tensor. This procedure can be illustrated mathematically by rewriting Eq. 1.5 as follows:

$$\ln[A(TE) / A(0)] = - 4\pi^2 \Delta \, \mathbf{k}^T \cdot \mathbf{D} \cdot \mathbf{k} = - \mathbf{b}^T \cdot \mathbf{d} \qquad (1.7)$$

where $\mathbf{d}$ is a column vector containing six components of the diffusion tensor D_{ij}, namely $\mathbf{d} = \{D_{11}, D_{22}, D_{33}, D_{12}, D_{13}, D_{23}\}$; and $\mathbf{b} = 4\pi^2 \Delta \{k_x^2, k_y^2, k_z^2, 2k_xk_y, 2k_xk_z, 2k_yk_z\}$ where $k_i =$

$(1/2\pi)\ \gamma\delta g_i$, g_i is the component of **g** in Cartesian coordinates, i = x, y, z. By changing the orientations of the diffusion-encoding gradient, one can obtain six different signal attenuations (represented by $\mathbf{a} = \{a_1, a_2, a_3, a_4, a_5, a_6\}$) corresponding to six different **b** vectors (represented by $\mathbf{b}_n$, n = 1,2,...,6). From the measured **a** and $\mathbf{b}_n$, **d** can be solved uniquely by

$$\mathbf{d} = \{\mathbf{b}^T_1, \mathbf{b}^T_2, \mathbf{b}^T_3, \mathbf{b}^T_4, \mathbf{b}^T_5, \mathbf{b}^T_6\}^{-1} \cdot \mathbf{a} \qquad (1.8)$$

The technique of diffusion tensor imaging soon gained much interest in structural study of the myocardium. Garrido et al. first demonstrated the ability of this technique to define 3D orientation of the myocardial fibers in perfused rat hearts (48). Scollan et al and Tseng et al demonstrated the capability of this technique to define myocardial sheet structure in tissue samples (55,56). People also began to explore the possibility of using this technique for *in vivo* studies on human subjects. *In vivo* MR diffusion tensor imaging of the heart is of particular interest because it provides a noninvasive way to assess the myocardial fiber organization, which previously could only be obtained by the invasive histology method. Thus, it is potentially useful in both basic and clinical investigations.

However, MR diffusion measurement in the beating heart is very difficult and complex. The first big problem comes from cardiac and respiratory motion. Because the diffusion is a slow process, the diffusion-sensitizing gradient needs to be switched on for a long time in order to gain enough diffusion-induced attenuation. However, due to cardiac and respiration motion, to image the same slice over the long period needed for diffusion imaging is almost impossible. Moreover, since bulk motion from pulsation or respiration is about a hundred-fold larger than molecular diffusion, the phase shift caused by bulk motion is much larger than that of diffusion. Thus, any imperfect refocusing of the transverse magnetizations due to bulk motion may cause unwanted signal attenuation or signal loss, which impairs the diffusion measurement. To overcome this problem, Edelman et al. proposed a stimulated-echo echo-planar MRI sequence for *in vivo* diffusion measurement (33). In his method, two diffusion-sensitizing gradients are placed at the same cardiac phase of successive heartbeats (double gating). The phase information induced by diffusion-encoding gradient is preserved over the period between preparation pulse and readout pulse (the diffusion time Δ, which is exactly one cardiac cycle). Thus, the diffusion time Δ is effectively prolonged to one cardiac cycle with a tolerable signal loss due to T_1 relaxation, rather than substantial signal loss due to T_2 relaxation. In regular heartbeats, little

bulk motion is phase-encoded by the diffusion-sensitizing gradients, and so signal attenuation of the echo is purely from the molecular diffusion.

Though Edelman's method effectively ameliorates the problem of bulk motion in diffusion measurement of the beating heart, it encountered a new problem, which is the interaction between diffusion encoding and myocardial strain, or the "strain effect". As pointed out by Reese et al., the problem arises from the physical deformation of spatial modulation of the magnetization, $\mathbf{k}(\mathbf{X}) = (1/2\pi)\ \gamma \mathbf{g}\delta = \mathbf{grad}(\phi)$, during the diffusion-encoding period (57). If myocardial tissue undergoes a deformation $\mathbf{F}(\mathbf{X}) \equiv \partial \mathbf{x}/\partial \mathbf{X} = \mathbf{grad}(\mathbf{x})$, $\mathbf{k}(\mathbf{X})$ is also "deformed" according to the linear mapping: $\mathbf{k}(\mathbf{X}) \rightarrow \mathbf{F}^{-T}(\mathbf{X})\cdot\mathbf{k}(\mathbf{X}) \equiv \mathbf{k}_{eff}(\mathbf{X})$. Thus, spins in the myocardium "see" a time-varying $\mathbf{k}_{eff}$ during diffusion time Δ instead of a constant $\mathbf{k}$. Therefore, according to the generalized form of Eq. 1.7, signal attenuation in this case is the result of the time integral of $\mathbf{k}_{eff}$:

$$\ln[A/A_0] = -4\pi^2 \Delta \langle \mathbf{k}^T_{eff}(t)\cdot\mathbf{D}(t)\cdot\mathbf{k}_{eff}(t)\rangle_\Delta \qquad (1.9)$$

Substituting $\mathbf{k}_{eff}(t)$ with $\mathbf{F}^{-T}(t)\ \mathbf{k}$, and using polar decomposition: $\mathbf{F}(t) = \mathbf{R}(t)\cdot\mathbf{U}(t)$, Eq. 1.9 can be written as:

$$\begin{aligned}\ln[A/A_0] &= -4\pi^2 \Delta\, \mathbf{k}^T\cdot\langle \mathbf{U}^{-1}\cdot(\mathbf{R}^T\cdot\mathbf{D}_0\cdot\mathbf{R})\cdot\mathbf{U}^{-1}\rangle_\Delta\cdot\mathbf{k} \\ &= -4\pi^2 \Delta\, \mathbf{k}^T\cdot\langle \mathbf{U}^{-1}\cdot\mathbf{D}_0\cdot\mathbf{U}^{-1}\rangle_\Delta\cdot\mathbf{k} \qquad (1.10)\end{aligned}$$

The last expression in Eq. 1.10 has used the fact that the diffusion tensor rotates with the myocardium, i.e., $\mathbf{D}(t) = \mathbf{R}(t)\cdot\mathbf{D}_0\cdot\mathbf{R}^T(t)$, and has assumed that true diffusivity $\mathbf{D}_0$ is independent of tissue stretch. Therefore, the observed diffusion tensor $\mathbf{D}_{obs}$ is related to the true diffusion tensor $\mathbf{D}_0$ by:

$$\mathbf{D}_{obs} = \langle \mathbf{U}(t)^{-1}\cdot\mathbf{D}_0\cdot\mathbf{U}(t)^{-1}\rangle_\Delta \qquad (1.11)$$

where U(t) is the stretch tensor at time t with respect to time t_0.

To correct the strain effect on the diffusion measurement in beating hearts, two different approaches have been proposed. One is based on Eq. 1.11, from which one can solve for $\mathbf{D}_0$ using stretch tensor history U(t) and the measured $\mathbf{D}_{obs}$. Reese proposed that the history of the stretch tensor over a cardiac cycle can be obtained by a motionless movie technique (58). The

motionless movie technique utilizes stimulated echoes to sample the temporal evolution of the 3D velocity of each pixel in a fixed image. After obtaining velocity data, the stretch tensor history in the material coordinates can be computed by numerical integration. The fixed image used in the motionless movie technique is taken at the identical cardiac phase as the time of MR diffusion imaging so that images of D_{obs} and U(t) are well-registered. In this way, $\mathbf{D}_0$ in each pixel can be solved for using Eq. 1.11.

Reese's scheme for stretch correction is theoretically feasible. However, it suffers from large noise and lengthy scanning time. The noise arises mostly from inherently noisy measurement of the stimulated-echo sequence, especially when the period between preparation and readout pulses is close to one cardiac cycle. Other noise comes from the complex computation for stretch correction that may lead to large propagated errors. The lengthy scanning time results from the need to recording myocardial strain history. The scanning time for 3D motionless movie at 50 ms temporal resolution may take up to one hour. These problems prohibit the practical use of diffusion tensor imaging in the beating heart.

To overcome this problem, Tseng proposed a unique way that is practical for clinical use (59). In his approach, the strain effect is not corrected but rather circumvented, so that diffusion measurement gives accurate results. He made use of the synchrony of normal cardiac motion, and found that there are time points in the cardiac cycle, "sweet spots", when the cardiac configuration approximates its temporal mean. If the diffusion is encoded at these points, the net effect of strain on the observed diffusion approximates to zero, and so the diffusion measurement gives accurate results. Tseng also performed systematic phantom study and *in vivo* study to validate his method. Tseng's method overcomes the shortcomings of Reese's method, and enables practical application of cardiac diffusion measurement in clinical situations, as the diffusion scanning can be finished in around 10 minutes. However, his method can only be applied on normal subjects because a synchrony of normal cardiac motion is required in his solution.

Reese's and Tseng's methods both use unipolar gradient pulses that encode diffusion over one cardiac cycle. Though unipolar method has become practical through years of development and also showed effectiveness in imaging myocardial diffusion, challenges remain as researchers question whether any unknown motion effect other than the strain effect has been overlooked by this method. Thus, to fully address the validity of this method, further study needs to be carried

out. This thesis will develop a new diffusion imaging scheme to completely address this troubling question on motion effects, and demonstrate the validity of current techniques of cardiac diffusion MRI.

1.4.2 Myocardial strain measurement by MRI

The sensitivities of MRI to spin motions can be applied to measure the intramural motion of the heart wall noninvasively. Myocardial deformation can be mechanically described by the myocardial strain, a tensor property of the relative motion between neighboring material points. By tracking myocardial motion using MRI, the myocardial strain tensor can be computed. Currently, there are two different MRI approaches to access the myocardial motion: 1) magnetization tagging and 2) velocity encoding. The following paragraphs review these two strain measurement techniques.

1.4.2.1 Magnetization tagging

Magnetization tagging normally uses a grid of magnetic saturation produced by applying a sequence of radio frequency (RF) pulses. This grid provides landmarks that can be used to track the myocardial motion, and so myocardial strain can be computed.

The basic physical principle of magnetization tagging was first discovered by Suryan in 1951. After the demonstration of NMR by Bloch et al. (37) and Purcell et al. (60), Suryan carried out some experiments with flowing liquid (61). He applied a strong B_1 field to magnetized stationary liquid in a fixed volume, and found that the measured nuclear absorption signal was greatly attenuated due to substantial saturation by the B_1 field. However, when he repeated the same experiment on the flowing liquid, the NMR signal increased proportionately with liquid velocity. This velocity-dependent signal arises from the fact that the liquid flowing into the volume of detection carries unsaturated protons. Depending on the flow rate, "fresh" protons replace different amounts of the saturated protons originally in the volume, and can be nutated by the B_1 field and emit signals proportional to the liquid velocity.

The discovery of this kind of velocity-sensitive NMR soon gained attention, and people began to apply it in biological studies such as imaging blood flow. Application of velocity-sensitive NMR to the measurement of blood flow rates *in vivo* was first illustrated in the works

of Singer et al. In 1959, Singer suggested that the velocity of blood flow could be determined in terms of three measurements: longitudinal relaxation time T_1, and two signal amplitudes, one with flow and one without flow (62). He performed the first *in vivo* NMR measurement of blood flow in mouse tails to demonstrate his method. He also proposed an MR "time-of-flight" method to measure the blood velocity. This method uses one set of transmitter coils located upstream to demagnetize the proton spins, and the second set of coils downstream to monitor the signal. By estimating the time for the bolus of demagnetized nuclei to reach the monitoring point, the flow velocity can be determined. The first NMR measurement of blood flow in humans was carried out by Morse and Singer in 1970 (63). They used the time-of-flight tagging method to measure blood flow in the median veins of human arms. In their experiment, the "tagged" bolus of proton spins was used as the tracer to determine the velocity from the transit time of flow. This method is more straightforward than Singer's three-measurement method, and forms the groundwork for the subsequent development of the MR tagging technique used to obtain quantitative images of the blood flow.

Tagging with cardiac MRI for the assessment of myocardial motion was first demonstrated by Zerhouni et al. (64). The basic idea of this method is to use certain RF pulses to produce regular dark bands of selective saturation, followed by conventional imaging sequence. Specifically, after slice selection, spatially designed RF pulses are applied immediately to demagnetize spins in certain regions within the imaging plane. When the image is acquired, these demagnetized regions will appear to be dark in the image plane because the spins in these regions do not give out signal. The spatial patterns of these dark regions are normally chosen to be strips or grids, forming effective tagged markers in the imaging plane. Since the demagnetized nuclei move with the tissue, any motion between the time of demagnetization and subsequent imaging will be seen as a corresponding displacement of these tagged markers. Because T_1 of myocardium in general is about several hundred milliseconds, it is possible to observe the deformation pattern of the tag image over the ejection phase before tagged markers fade away.

To calculate a 3D strain tensor field of the ventricular myocardium using the MRI tagging method, multiple short-axis and long-axis images of tagged grids over the whole ventricle need to be taken. After the tagged images are obtained, the motion of a 3D grid system can be reconstructed (65, 66). This is usually done by tracking the intersections of the tagged lines, so that the corresponding displacement vectors are determined. A 3D displacement field can then

be obtained using the finite element method to interpolate a smooth displacement function between the adjacent grid points (67). After the displacement field is calculated, any tensor quantity relevant to myocardial kinematics, such as deformation gradient or strain tensor, can be derived.

MR tagging has been found to be an easy-to-use method of assessing myocardial function. Compared to the traditional invasive method based on radiopaque markers, it is noninvaisve, allows higher density of markers and also full functional imaging of intramural myocardium. Thus, various successful studies have been performed on myocardial mechanics, such as demonstrating the normal pattern of cardiac torsion during contraction and its change corresponding to various abnormal conditions (68-70). However, current MR tagging techniques cannot provide a satisfactory spatial resolution. The spacing of the tagged lines is approximately 7 mm, which limits its capability to show the transmural variation of the strain component. This limitation also makes study of thin walls such as dilated cardiomyopathy or post-infarct expansion a difficult task. MR tagging normally requires a large number of slices to obtain enough grids for strain calculation. However, in human study, the number of imaging slices must be decreased because of limited scanning time. This will further compromise the spatial resolution of the strain calculation. Moreover, the tagging method requires tracking of the same tagged markers from one scan to the next to provide the displacement data. However, in some locations of the ventricular wall, such as regions near the endocardium, the tagging marker is often confounded by the beat-to-beat variation of the endocardial contour, complex geometry of the trabeculae, and flow-related artifacts in the cavity. To overcome this, current methods of data analysis involve subjective guidance, and so are subject to inter-observer variation. Lastly, the tagging method requires tedious postprocessing to obtain the strain data, which limits its potential application in clinical studies. Thus, to establish it as a standard clinical tool, more development is required.

1.4.2.2 Velocity-sensitive phase shift

MR velocity encoding uses motion-induced phase shifts to measure myocardial motion. The phase of the signal is directly related to the velocity of the material within each voxel. The velocity fields can then be integrated to yield displacements to calculate strain tensor, or can be used directly without integration to calculate strain rate tensor.

The effect of velocity-induced phase shift on the NMR signal was first discussed by Carr and Purcell in 1954 (71). In their multi-echo experiment to measure transverse relaxation time (T_2) of liquids, they observed that, if there was convection flow in the sample, even echoes were larger than odd echoes. This effect is then found to arise from the phase memory of the nuclear-spin Larmor precession. The distances that individual proton spins travel through a magnetic field gradient are inscribed by their accumulated phases. Consequently, the ensemble evolution of the phases of the proton spins arrives at perfect refocusing at even echoes, producing larger amplitudes than those of odd echoes. In 1960 Hahn proposed the use of spin echoes to measure coherent motion of sea water (72). He derived an important equation that relates the velocity v with the phase shift $\Delta\phi$ of the spins by

$$\Delta\phi = \gamma g v t^2 \tag{1.12}$$

where γ is the gyromagnetic ratio of proton nuclei, g is the magnetic field gradient, and t is the time between RF pulses, which is one half of the echo time (t = TE/2). This relation formed the conceptual basis for the development of phase-contrast MRI in the following decades.

The more generalized formula of phase shift ϕ of motion spins in an NMR signal (72) is given by:

$$\phi = \gamma \int_0^{\tau} \mathbf{G}_r(t) \cdot \mathbf{r}(t)\, dt \tag{1.13}$$

Where γ is the gyromagnetic ratio characteristic of the nuclei, τ is the time duration of the gradient after excitation, $\mathbf{G}_r(t)$ is a temporal function of the magnetic gradient superimposed on the static magnetic field B_0, and $\mathbf{r}(t)$ describes the position of the nuclear spins as a function of time. In the case where $\mathbf{r}(t)$ represents simple linear motion and acceleration and higher-order terms are negligible, then $\mathbf{r}(t) = \mathbf{r}_0 + \mathbf{v}_0 t$, where r_0 and v_0 are the position and velocity at time t = 0. Equation 1.13 can then be expressed as:

$$\phi = \gamma \int_0^{\tau} \mathbf{G}_r(t) \cdot \mathbf{r}_0\, dt + \gamma \int_0^{\tau} \mathbf{G}(t) \cdot \mathbf{v}_0\, t\, dt \tag{1.14}$$

When the gradient function is selected such that $\int_0^{\tau} \mathbf{G}_r(t) \cdot \mathbf{r}_0\, dt = 0$, Eq. 1.14 is simplified to:

$$\phi = \gamma \int_0^{\tau} \mathbf{G}(t) \cdot \mathbf{v}_0\, t\, dt \tag{1.15}$$

In the one-dimensional case, Eq. 1.15 can be written as:

$$\phi = \left(\gamma \int_0^{\tau} G(t)\, t\, dt\right) v_0 = K_v v_0 \tag{1.16}$$

where $K_v = \gamma \int_0^\tau G(t)\, t\, dt$ is the velocity sensitivity, a constant frequently used in phase contrast MRI.

The classic velocity-encoding technique for MRI was developed by Moran in 1982, soon after MRI equipment was manufactured for clinical use. Moran proposed a theory of phase-gradient-modulation technique for phase-encoding velocity (73). In this technique, a bipolar velocity-sensitive gradient pair can be interlaced into an already existing MR imaging sequence without interference. Velocity components of the moving tissue are directly encoded as true subject variables of the magnetization to be imaged, while the spatial positions of the magnetization are phase-encoded in conventional imaging sequence. Using phantom studies, Moran demonstrated the ability of phase contrast MRI to accurately quantify the velocity of the flow (74). The application of phase contrast MRI to detect myocardial motion and blood flow was first implemented by van Dijk in 1984 (75). He found that the existing gradient pair for signal readout actually phase-encoded the velocity of the moving spins. After offsetting unwanted phases caused by the slice-select gradients, he obtained the phase image that was directly related to the velocity along the slice-select direction. He also color-coded velocity images at different points in the cardiac cycle, and showed that the patterns of spatial velocity distribution were compatible with physiological motion patterns of the myocardium and the aortic blood flow.

Though velocity is crucial to indicate the functional status of the physiological flow, to describe the mechanical function of the myocardium, it is desirable to be able to calculate the myocardial strain/strain rate tensor, a rank-2 tensor constructed from differential displacements/velocities between adjacent points. While complex methods have been developed to calculate the displacement from the velocity data and then compute the strain tensor from the trajectories (76-78), a more straightforward and robust way is to compute the strain rate tensor, which can be done directly from differential velocities between adjacent points. Wedeen (1992) first computed the 2D myocardial strain rate tensor by taking spatial derivatives of the in-plane velocity components obtained by phase-contrast MRI (79). Using the fact that linearization holds for small displacements detected within a short period of velocity sensitization, the strain rate tensor **S'** can be reasonably approximated by a linear combination of the spatial gradient of the velocity, **grad v**, and its transpose, $(\mathbf{grad\ v})^T$:

$$\mathbf{S'} = 1/2\ (\mathbf{grad\ v} + (\mathbf{grad\ v})^T) \qquad (1.17)$$

With single-shot echo-planar MRI (EPI), a series of strain rate tensor images at 30 ms increments through the cardiac cycle can be effectively obtained within 20 min. The results show that the temporal evolution of the radial strain rates corresponds to the pattern of thickening and thinning action of the ventricular wall in systole and diastole, respectively. Strain rate imaging technique offers a powerful insight into the mechanical function of the myocardium at the time of imaging. Moreover, since calculation of the strain rate tensor only requires that the phase difference between adjacent pixel does not exceed π, a high velocity-sensitizing gradient can be applied for high signal-to-noise ratio images, which ensures high quality data sets. Based on this phase-contrast EPI technique described by Wedeen, Tseng et al. extended the strain rate measurements from 2D to 3D, and established a practical way to compute 3D strain rate tensors to describe the mechanical function of the myocardium (80).

Velocity-encoding MRI has advantages in studying myocardial mechanics over the tagging method. First, it could have higher spatial resolution compared with the tagging method, which is limited by the thickness of the tagging lines; thus, it is able to perform more delicate study of the mechanical function of intramural myocardium. Second, the postprocessing of the images in the velocity-encoding method is faster and less tedious than in the tagging method; thus, it has the full potential to be automated and applied in clinical studies. In this thesis, we will explore and apply the velocity-encoding method to measure *in vivo* myocardial 3D strain. The image of 3D strain will then be registered with the image of myocardial structure (obtained by *in vivo* diffusion measurement) to study the functional role of myocardial sheets.

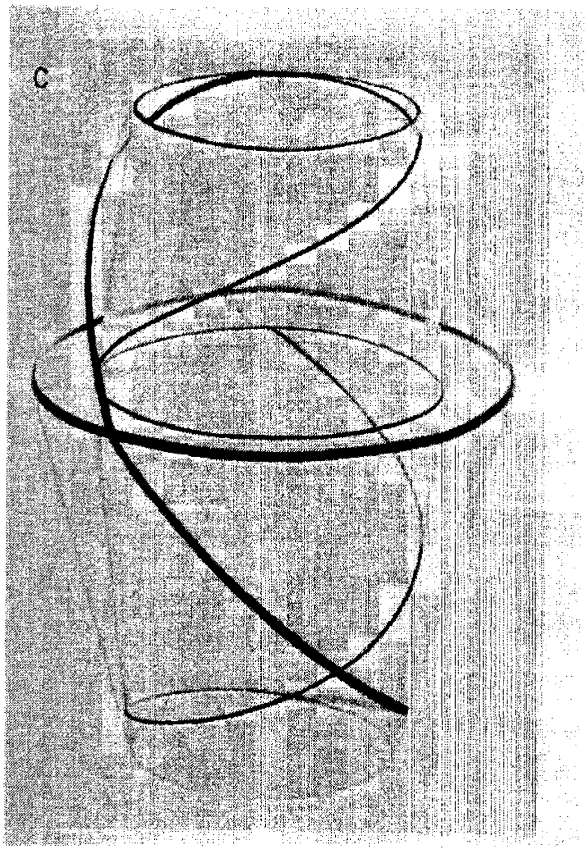

Figure 1.1 Reconstructed fiber pathways on one cusped toroidal shells. The paths preserve their geodesic property on the surface of the corresponding shells, and form figure-eight configurations. (From Streeter et al. (17))

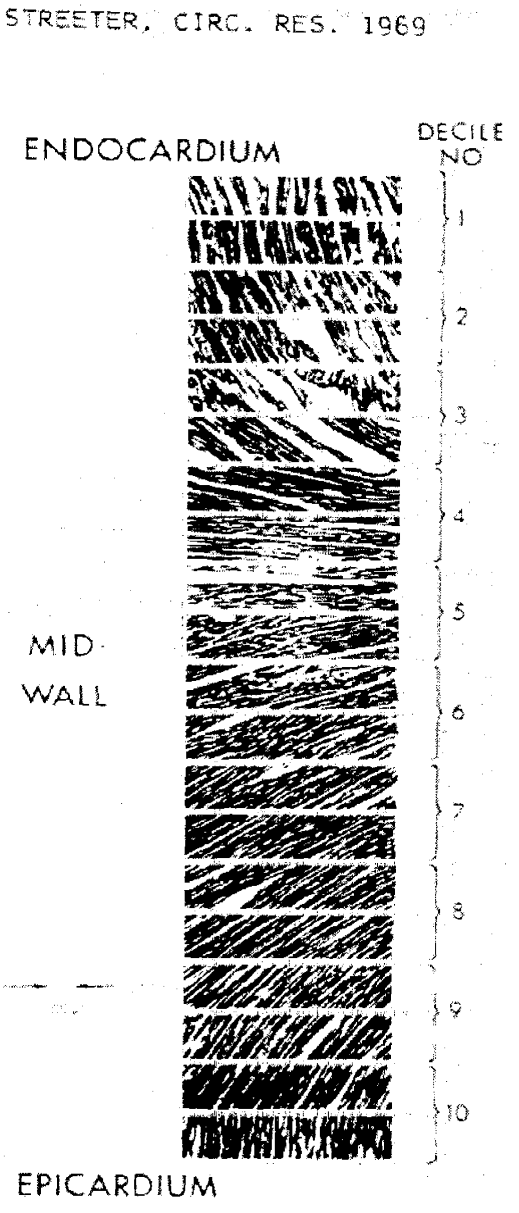

Figure 1.2 Sequence of photomicrographs in epicardial tangent plane, showing gradual change of helix angle through ventricular wall of a canine heart. The helix angle approaches 90° endocardially and -90° epicardially, running through 0° at the midwall, with a range approaching 180°. (From Streeter et al. (17))

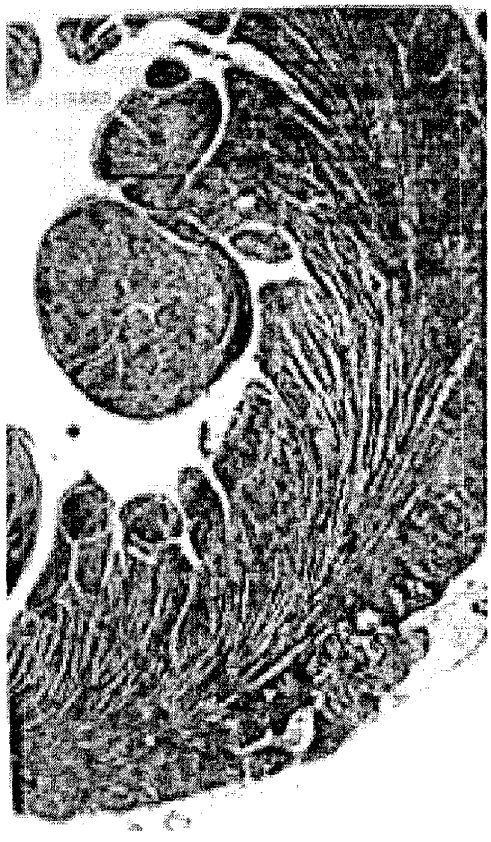

Figure 1.3 Transverse section through the human left ventricular free wall at mid-ventricular level (5 x magnification). A feathering pattern of cleavage planes is clearly shown. (From Lunkenheimer et al. (112))

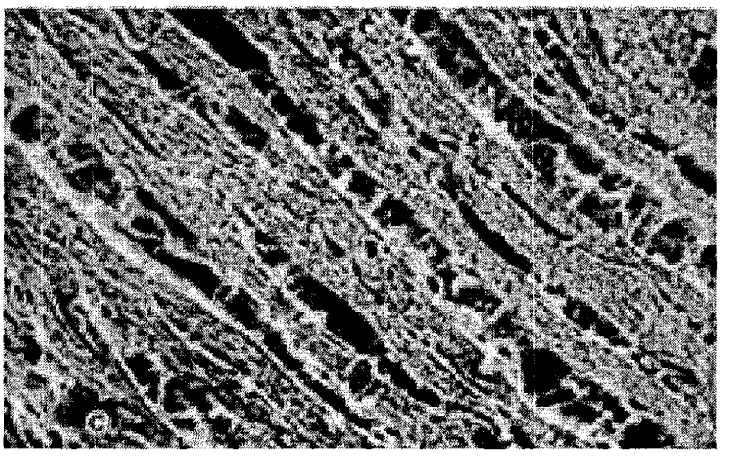

(a)

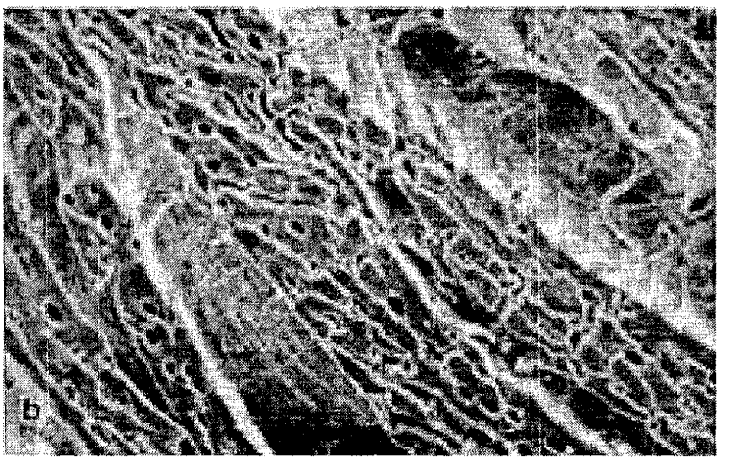

(b)

Figure 1.4 Electronmicrographs of laminar sheet architecture. (a) Transverse midwall section of x 145 magnification showing layers of myocyte groups with distinct gaps between them. (b) Groups of myocytes are surrounded by meshwork of connective tissue., x510. (From Smaill et al. (89))

Chapter 2

Cardiac Diffusion MRI without Motion Effects

2.1 Introduction

Diffusion MRI provides a noninvasive window into tissue architecture (33,48,55-59,80). In the heart, myocardial structure and function are intimately linked and can change dramatically in disease. Accordingly, diffusion MRI methods have been developed to map myocardial architecture *in vivo* (33,57-59,80). As described in chapter one, initially, methods were devised that, by encoding diffusion over an exact cardiac cycle, sought insensitivity to gross cardiac motion (1). It subsequently was found that such diffusion encodings interact with myocardial strain, and effective methods were described to overcome this effect by measuring the history of myocardial strains (57-59,80). A comprehensive measurement of cardiac strain can be challenging, but more germanely, it leaves the dependent diffusion measurements open to question, to the extent that they may be influenced by unrecognized cardiac motion or some other unanticipated mechanism. To fully address the validity of diffusion MRI in the beating heart, the problem of motion sensitivity needs to be further addressed.

This chapter presents a new method for diffusion MRI in the beating heart which encodes diffusion at a single cardiac phase. We will demonstrate that this method fully addresses the problem of motion sensitivity of diffusion MRI in the beating heart, and validate the theory of *in vivo* MRI of myocardial diffusion.

2.2 Methods

2.2.1 Experimental design

To encode diffusion in a single cardiac phase in the beating heart, we use a bipolar gradient pulse of less than 30 ms in duration. The two gradient lobes (encoding and de-encoding gradient pulses) in the bipolar pulse are identical but opposite in sign, which limits the diffusion sensitivity to the interval of the bipolar pulse. Thus, the applied bipolar pulse effectively encodes diffusion at a single cardiac phase. This bipolar pulse requires flow compensation (33). To accomplish this, we apply after phase reversal an identical bipolar gradient pulse at the identical phase of the next cardiac cycle, using a stimulated echo with two ECG triggers (Fig 2.1 A). This sequence is perfectly flow compensated for periodic motion, and the net diffusion sensitivity is the sum of the contributions of the two bipolar gradients.

Previously, a similar alternative method was proposed using unipolar pulses, Fig. 2.1 B (33). This 'unipolar method', while free of phase sensitivity to motion of cardiac periodicity, remains sensitive to material strains over the cardiac cycle. In this method, the diffusion encoding persists over the entire cardiac cycle that intervenes between the encoding and de-encoding gradient pulses. At any time during this period, material strain physically stretches the applied spatial modulation of spin phase and so the encoding yields diffusion contrast that indicates an observed diffusion tensor in general different than that would have been observed had the material remained stationary (57). Given this effect, methods were proposed to accurately determine the true underlying diffusion, first by calculation based on MRI of the full myocardial strain history (58) and then in the normal heart by locating special cardiac delays ('sweet spots') where strain effects cancel (59). The bipolar method described herein should be free of this effect, because it has no diffusion sensitivity during the intervening cardiac cycle when strain occurs.

This section validates the new method in two ways: first, we show in a phantom with cyclic motion that diffusion measurements with the bipolar encoding are in fact independent of motion, where those of the unipolar method are not; second, studies in human subjects show that myocardial diffusion eigenvalues measured with the present method have no statistically significant change between peak contractile velocity and at cardiac standstill (mid- vs. end-

systole), demonstrating that the observed diffusion is independent of myocardial motion. We will further show that the new method agrees with previous MRI methodology shown valid in the normal heart, providing cross-validation of both methods and confirming the validity of the theory of MRI diffusion measurement in the beating heart.

2.2.2 Validation *ex vivo*

To directly demonstrate the motion- and strain-independence of the bipolar method, we compared the unipolar and the bipolar methods in a phantom with cyclic strain. The phantom is a cylinder of aqueous gelatin 12 cm high by 12 cm in radius whose top face is cyclically indented along the cylinder axis to a depth of 2 cm by a motorized plunger at a constant rate of one indentation per 750 ms.

Experiments were performed on a 1.5-T GE Signa MR imager. Images of the gelatin phantom at different phases in the deformation cycle were acquired using the unipolar and bipolar encoding techniques. Diffusion-encoding used gradients $\boldsymbol{G}$ directed to non-opposed edge centers of a cube $\{\{1,\pm1,0\},\{0,1,\pm1\},\{\pm1,0,1\}\}$ of intensity $|\boldsymbol{G}_U| = 3.1$ mT m^{-1} for the unipolar method and $|\boldsymbol{G}_B| = 40$ mT m^{-1} for the bipolar method. Pulse offset $\Delta_U = 750$ ms and duration $\delta_U = 26.2$ ms in the unipolar case, and $\Delta_B = \delta_B = 13.2$ ms in the bipolar case (see Figure 1), furnishing equal diffusion sensitivities of $b \approx 350$ s mm^{-2} in both cases, the uni- and bipolar diffusion sensitivities being given by

$$b_U = |\boldsymbol{k}_U|^2(\Delta_U - \delta_U/3) \tag{2.1a}$$

$$b_B = 4/3|\boldsymbol{k}_B|^2\delta_B \tag{2.1b}$$

respectively, where $\boldsymbol{k}_i = 2\pi\gamma\delta_i\boldsymbol{G}_i$ is the spatial modulation vector in each case, where $i = \{U,B\}$ and γ the proton gyromagnetic ratio. Spatial encoding used single shot EPI with 3 mm isotropic resolution. Equal echo times TE = 82 ms were used in both cases. Diffusion tensor MRI movies were acquired with 50 ms progressive delays for a single slice that contains the phantom axis. Registered phase-contrast MRI movies of 2D strain rates were also acquired (58,79).

After data acquisition, the diffusion tensor images at each time frame were computed by linear inversion of the relations for the image attenuations in the uni- and bipolar experiments I_U/I_0 and I_B/I_0, respectively:

$$-\log(I_U/I_0) = (\Delta_U - \delta_U/3)\,\boldsymbol{k}_U^T\,\boldsymbol{D}_{obs}\,\boldsymbol{k}_U \tag{2.2a}$$

$$-\log(I_B/I_0) = 4/3\ \delta_B\ \boldsymbol{k}_B^T\ \boldsymbol{D}_{obs}\ \boldsymbol{k}_B \qquad (2.2b)$$

where I_U and I_B represent diffusion-attenuated images by the unipolar and bipolar methods, I_0 represents unattenuated image, and $\boldsymbol{D}_{obs}$ is the measured diffusion tensor (81). The corresponding strain rate images were also calculated. To quantify the changes in the observed diffusivity, we examined the radial component $D_{r,obs}$ of the observed diffusion tensor $\boldsymbol{D}_{obs}$, $D_{r,obs} = \boldsymbol{r}^T\ \boldsymbol{D}_{obs}\ \boldsymbol{r}$, where $\boldsymbol{r}$ is the radial unit vector, with polar origin at plunger contact (Figure 2, top center).

As previously shown (59), for the unipolar method, if we let $\boldsymbol{S}_t(\tau)$ be the strain at time τ relative to time t, and $\langle \ldots \rangle = \Delta^{-1} \int_\Delta \ldots\ d\tau$ denote the time-average over one cardiac cycle Δ, then the measured diffusivity $\boldsymbol{D}_{obs}$ is related to the true intrinsic diffusivity $\boldsymbol{D}_0$ by:

$$\boldsymbol{D}_{obs}(t) \approx \boldsymbol{D}_0 - \langle \boldsymbol{S}_t \rangle \boldsymbol{D}_0 - \boldsymbol{D}_0 \langle \boldsymbol{S}_t \rangle \qquad (2.3)$$

where strains are computed relative to the configuration at the time of measurement. For the radial component, Eq. 3 becomes

$$\begin{aligned} D_{r,obs}(t) &\approx (1 - 2\langle S_{r,t} \rangle)\ D_{r,0} \\ &\approx (1 - 2 f(t)\ S_{r,t}^{max})\ D_{r,0} \end{aligned} \qquad (2.4)$$

where $S_{r,t}^{max}$ is the map of peak radial strain and $f(t)$ is a scalar function describing the time dependence of S (82).

Because the diffusivity of the gel phantom is uniform and also unaffected by the strain (57), i.e., $D_{r,0}$ is constant, the above equation gives that the $D_{r,obs}$ measured by the unipolar method is dependent on $\langle S_{r,t} \rangle$. Since $\langle S_{r,t} \rangle$ varies with t and location, it is expected that $D_{r,obs}$ of the unipolar method will have both spatial and time variations through the deformation cycle. If the bipolar method is motion- and strain-independent, the observed diffusivity should be constant in space and time. To measure the variations of $D_{r,obs}$, we compute an image representing the standard deviation σ of the time-series $D_{r,obs}(x)$ at each location x

$$\sigma[D_{r,obs}(\boldsymbol{x}, t)] = \langle [D_{r,obs}(\boldsymbol{x}, t) - \langle D_{r,obs}(\boldsymbol{x}, t) \rangle]^2 \rangle^{1/2} \qquad (2.5)$$

We hypothesize that in the bipolar case $\sigma[D_{r,obs}(\boldsymbol{x}, t)] \approx 0$ but that in the unipolar case $\sigma[D_{r,obs}(\boldsymbol{x}, t)] \neq 0$, and in particular

$$\sigma[D_{r,obs}(\boldsymbol{x}, t)] \propto S_r^{max} \qquad (2.6)$$

2.2.3 Validation *in vivo*

2.2.3.1 Myocardial diffusion eigenvalues during systole

Using the bipolar method, we measured myocardial diffusion eigenvalues at different phases in systole on a normal human subject, and compared the observed values at moving phases (during systole) with that at the standstill phase (end-systole) to examine the cardiac motion effect.

After providing written informed consent, which was approved by the hospital human study committee, the subject was instructed to use synchronized breathing to suppress respiration motion in the diffusion studies. Electrocardiogram (ECG) R-wave triggering was used for data acquisition. After a mid-ventricular short-axis slice was located, the standstill phase at end-systole was found at around ECG trigger delay 325 ms by examining myocardial velocity phase maps at multiple points through the cardiac cycle. Diffusion images at 6 phases from early-systole (trigger delay 75 ms) to end-systole (trigger delay 325 ms) in 50 ms time steps were then acquired using single-shot EPI with spatial resolution of 4 x 4 x 12 mm. The diffusion-encoding gradient intensity used was $|\boldsymbol{G}_B| = 40$ mT m^{-1}, pulse duration $\delta_B = 13.2$ ms, furnishing a diffusion sensitivity $b \approx 350$ s mm^{-2}. $TE = 82$ ms and $TR = 4$ R-R intervals were used in all acquisitions. The heart rate of the subject was stable during the experiment. The total imaging time per study is under 10 minutes. After the quality of acquired images was assured by examining both the magnitude and phase images, myocardial diffusion eigenvalues were calculated at each image pixel. The mean diffusion eigenvalues of the left ventricle (with papillary muscle excluded) were then computed at each phase for comparison.

If the bipolar method is insensitive to the cardiac motion effect, i.e., there is little or no hidden motion effects on the measurements, we expect that the observed diffusion eigenvalues should show little or no differences between the moving phases (during systole) and the stand-still phase (end-systole).

2.2.3.2 Agreement between the bipolar method and the unipolar sweet spot method

As previously described (59), the unipolar method provides an accurate map of myocardial diffusion tensor field in the normal heart at times t (the sweet spots) where the strain effect is

canceled. To validate the overall accuracy of the unipolar sweet spot method and also demonstrate the accuracy of the bipolar method for *in vivo* studies, especially in structural measurements, we compared the bipolar method and the unipolar method at several points in the cardiac cycle, including the sweet spot.

The experiment was performed on a healthy human subject whose average heart rate was 64 beats/min during the experiment. Synchronized breathing and ECG R-wave triggering were used for data acquisition as in previous studies. After a mid-ventricular short-axis slice was located, the diffusion images were spatially encoded using single-shot EPI with spatial resolution of 4 x 4 x 12 mm. Registered diffusion images measured by the unipolar method and the bipolar method at four points in the cardiac cycle (trigger delay 80 ms, 160 ms (sweet spot), 240 ms and 320 ms) were then obtained. The diffusion-encoding gradient intensity used was $|\boldsymbol{G}_U| = 2.8$ mT m^{-1} for the unipolar method and $|\boldsymbol{G}_B| = 40$ mT m^{-1} for the bipolar method. Pulse durations $\delta_U = 26$ ms and $\delta_B = 13.2$ ms. With a heart rate at 64 beats/min, these parameters furnish an equal diffusion sensitivity $b \approx 350$ s mm^{-2} for both methods. $TE = 82$ ms and $TR = 4$ R-R intervals were used for both cases, and the total imaging time per study is under 10 minutes for both methods.

After registered unipolar and bipolar diffusion images were obtained, image quality was assured by examining both the magnitude and phase images. The diffusion tensors were then calculated at each image. Pixels of the left ventricle (with papillary muscle excluded) are used for comparison. To validate the overall accuracy of the sweet spot method, we compared the mean diffusion eigenvalues measured by the bipolar method and the sweet spot method to show that the sweet spot method is insensitive to the cardiac motion effect. To demonstrate the accuracy of the bipolar method in measuring *in vivo* myocardial structures, we compared observed diffusion tensors $\boldsymbol{D}$ and eigenvectors of $\boldsymbol{D}$ at each pair of unipolar-bipolar registered pixels at all four cardiac phases. The $\boldsymbol{D}$ were compared by representing the tensors as vectors $\boldsymbol{d} = \{D_{11}, D_{22}, D_{33}, D_{12}, D_{13}, D_{23}\}$, where D_{ij} are tensor components. The tensor difference T_d between the unipolar and bipolar methods were then calculated as $T_d = |\boldsymbol{d}_U - \boldsymbol{d}_B|^2$, where $\boldsymbol{d}_U$ and $\boldsymbol{d}_B$ are tensor data measured by the unipolar method and the bipolar method respectively. The eigenvectors of $\boldsymbol{D}$ are indicators of the myocardial fiber and sheet structure (33,48,55-59,80) and were compared by calculating the angle difference θ_i between each pair of eigenvectors, $\theta_i = \arccos(|\boldsymbol{u}_i \cdot \boldsymbol{b}_i|)$, where $\boldsymbol{u}_i$ and $\boldsymbol{b}_i$ are ith eigenvectors measured by the unipolar method and the

bipolar method respectively. After differences were calculated for each pair of registered pixels, statistical analysis of these values was performed on an ensemble of all-pixels. The final results are shown as Mean ± Confidence Interval (CI) of T_d and θ_i as indicators of agreement between the two methods. We also estimated T_d and θ_i that are caused by the noise. This is done by randomly dividing the same set of diffusion attenuation images into two half data sets and comparing differences between the tensors and eigenvectors calculated by these two half data sets; the differences by the noise for the full data sets were then estimated by using the noise reduction relation between the half and full data sets.

If both the bipolar method and the unipolar sweet spot method are accurate and insensitive to the cardiac motion effect, we expect that the bipolar method and the unipolar method should agree at the sweet spot, where the measurement differences should be close to the noise level. We also expect that the bipolar method and the unipolar method should disagree (differences > noise level) at other points where the bipolar method still holds accuracy while the unipolar method is disrupted by the strain effect.

2.3 Results

2.3.1 Validation *in vitro*

Figure 2.2 shows the diffusion MRI of the gel phantom acquired using the unipolar and bipolar pulse sequences; the magnitude image is at top and the images of observed standard deviations σ of radial diffusivities over the deformation cycle for uni- and bipolar sequences with equal diffusion sensitivities are shown at center and bottom, respectively.

In a wedge-shaped ROI beneath the plunger, a region of relatively high strain, it is found that principle strains S and strain-rates dS/dt have maxima $\max(S) = 0.3$ and $\max(dS/dt) = 2\pm1\ s^{-1}$, similar in size to normal human myocardial values. For individual diffusivity maps measured during the deformation cycle, we found that those of the unipolar experiments show significant spatial variations due to the strain effect, while in the bipolar experiments, the spatial variations of observed radial diffusivity ($D_{r,obs}$) can not be isolated from the background variability of $D_{r,obs}$ (around 5% in current experiments). In Fig. 2.2, we computed the standard deviations σ of $D_{r,obs}$ over the deformation cycle (Eq. 2.5). In the unipolar experiment, the standard deviations σ of $D_{r,obs}$ are large (Fig.2A), with $\sigma(D_{r,obs})$ as great as 50% of the mean diffusion near the plunger.

By contrast the bipolar experiment shows a $\sigma(D_{r,obs})$ of at most 5% of the mean diffusion (Fig.2B), representing a ten fold reduction of the strain effect.

2.3.2 Validation *in vivo*

2.3.2.1 Myocardial diffusion eigenvalues during systole

Figure 2.3 shows the mean diffusion eigenvalues during contraction at 50 ms time steps on a normal human subject. The eigenvalues are nearly constant during contraction, with no statistically significant differences ($p < 0.05$) from early- to mid-systole (75ms - 175 ms trigger delay), or from mid- to end-systole (175 ms - 325 ms trigger delay), confirming independence of the rate of myocardial contraction. We note that for the whole range from early- to end-systole, the first and second eigenvalues show statistically significant decrease by 5-10% ($p < 0.05$) while the third eigenvalue increases by 5-10% ($p < 0.05$).

2.3.2.2 Agreement *in vivo* between the bipolar method and the unipolar sweet spot method

Figure 2.4 shows the mean myocardial diffusion eigenvalues measured by the bipolar method and the sweet spot method during contraction on the subject in study, and also the mean diffusion eigenvalues of 6 normal subjects previously measured by the sweet spot method. The intra-subject results show that the bipolar method agrees with the sweet spot method. The inter-subject results show that, within the experimental uncertainties, the myocardial diffusion eigenvalues of different subjects are in a similar range.

Table 2.1 Mean ± Confidence Interval of tensor difference T_d and tensor-eigenvector difference θ_i between the unipolar and bipolar method at ECG trigger delay 80 ms, 160ms (sweet spot in bold), 240 ms and 320 ms.

Time	Tensor (T_d) (10^{-12} cm^4/s^2)	$\overline{T}_d/\overline{T}_d$(noise)	1st eigenvector (θ_1)	2nd eigenvector (θ_2)	3rd eigenvector (θ_3)
80 ms	7.5 ± 0.6	3.75	16.0° ± 1.8°	23.5° ± 2.7°	19.1° ± 1.7°
160 ms	**2.1 ± 0.3**	**1.05**	**9.0° ± 1.1°**	**13.8° ± 1.4°**	**10.3° ± 1.2°**
240 ms	10.3 ± 1.5	5.15	15.6° ± 1.9°	28.7° ± 3.3°	24.6° ± 3.5°
320 ms	13.0 ± 1.9	6.50	21.5° ± 2.7°	39.8° ± 3.8°	34.3° ± 4.1°
Noise estimate	2.0 ± 0.3	1.00	8.9° ± 1.1°	13.9° ± 1.3°	10.4° ± 1.2°

Table 2.1 compares the measurement results of the tensor field by the unipolar method and the bipolar method at ECG R-wave trigger delays 80 ms, 160 ms (sweet spot), 240 ms and 320

ms. We see that the two methods agree at the sweet spot, where the differences are at the noise level, and disagree at other points where the unipolar method is inaccurate.

2.4 Discussion

2.4.1 Experimental design

Cardiac motion is the central obstacle to *in vivo* MRI of myocardial diffusion. An effective MRI methodology should be able to imaging myocardial diffusion without motion effects, i.e., it should be able to measure myocardial diffusion as if the heart were arrested at the time of measurement. To realize this, the desired method should satisfy two conditions: first, it should encode diffusion in a very short time compared to the heart contraction time, so the myocardium is nearly immobilized at the time of imaging. Second, there should be no diffusion sensitivity outside the time of encoding, so the diffusion measurement will not be affected by motion effects from times outside the diffusion encoding period. The bipolar diffusion encoding gradient is designed for this purpose. The less than 30 ms pulse duration satisfies condition one, and the bipolar gradient pulse, which limits the diffusion encoding to within the duration of the diffusion encoding pulses, satisfies condition two. Thus, use of bipolar diffusion encoding pulses effectively encodes diffusion at a single cardiac phase and eliminates motion effects from outside the diffusion encoding period.

However, satisfying the above two conditions is not sufficient to solve the problem. The less than 30 ms pulse duration is short compared to the contraction time, but is long enough for the cardiac gross motion to create phase shifts inside each voxel that may cause loss of signal. So "flow compensation" is needed. Traditional flow compensation would use a second bipolar pulse immediately following the first with reversed sign (+-,-+) to reverse velocity phase shifts, but this solution is unsatisfactory in the heart because of non-constant velocity over the required time intervals. To address this, we have used a stimulated echo sequence with two ECG triggers to put the velocity compensation at identical phases on consecutive heartbeats, affording cancellation of phase shifts induced by periodic cardiac motion (33).

In addition to phase accumulation during the bipolar pulses due to cardiac gross motion, there may also be unrecognized intra-voxel incoherent motion (IVIM) effects within the duration of the bipolar pulses. Such IVIM effects may be caused by cardiac events like myocardial

fasciculation or perfusion etc., which could add additional diffusion signal to that of the myocardial intrinsic diffusion, and so will increase the apparent diffusion coefficient (ADC) of the myocardium. Examining this possible IVIM effects is crucial for evaluating the accuracy and motion-sensitivity of the bipolar method, so a comparison between ADC measurement at cardiac moving phases (with possible IVIM effects) vs. cardiac standstill (excluding possible motion effects) is necessary. Little or no differences in ADC measurements between the moving and standstill phases directly demonstrates the insignificance of possible residual IVIM effects on diffusion, and so validates the accuracy and motion-insensitivity of the current method.

The bipolar method described in this paper afford the opportunity to examine the accuracy of the previously developed unipolar method, which addressed the cardiac motion problem by eliminating effects from the cardiac gross motion and the myocardial strain at significant costs of increased experimental complexity and reduced generality. This unipolar approach was shown to be effective. However, due to its complexities and limitations, the method has difficulty fully validating itself by comparing diffusion measurement at moving phases vs. the standstill phase. Thus, the unipolar method is open to question in that it may be influenced by unrecognized forms or effects of cardiac motion. The bipolar method, which is shown to be free of motion effects, offers the opportunity to examine the accuracy of the unipolar method. By comparing the diffusion measurement results by the two methods, we seek to address the confounding question on the unipolar method.

Recent observation of random spontaneous contractile movement in cardiocytes raises the question of whether some fraction of present diffusion contract may in fact have been produced by physiologic movements (Balaban R., personal communication). Such effects may be difficult to exclude. As such motion may occur throughout the cardiac cycle, they are not excluded by present findings of constant diffusion over the cardiac cycle. Neither are they excluded by the finding that diffusion tensor fields match the known fiber architecture, as they too may correlate with this architecture. However, evidence that spontaneous cellular fasciculation make minimal contribution to present measurements is strongly supported by the equality of myocardial diffusion measured with the unipolar and bipolar pulse sequences. While the uni- and bipolar experiments were constructed to have equal sensitivity to random diffusion, cellular fasciculation contains coherent components over the relevant timescales, these two experiments have markedly different sensitivities to such motion. According to a classic theory of generalized

motion sensitivity, NMR signal attenuation may be predicted from the spectral overlap between the power spectrum of the autocorrelations of spin velocities with the power spectrum of the motion-encoding gradient waveform (83-86). If we assume that most of the power of the fasciculatory motion is with the frequency band from 5 to 500 Hz, then the spectral amplitude of the bipolar experiment within this range is 5 to 60 times higher than that of the unipolar experiment, because the bipolar gradient pulses are more intense and more numerous. It follows that such fasciculation should produce greater attenuation in bipolar than unipolar experiments. As we find these data to agree in absolute terms, we conclude that such effects are negligible in present measurements, both unipolar and bipolar. Experiments to map the spectral content of myocyte fasciculation can be contemplated, perhaps with sinusoidal gradients for high spectral sensitivity and specificity (87).

2.4.2 Validation

Present studies in phantoms show that diffusion MRI with the bipolar method is independent of periodic motion and strain. Present *in vivo* studies show that the bipolar method measures no significant change in absolute diffusion from myocardial peak motion to myocardial standstill. This directly demonstrates that bipolar diffusion MRI is independent of myocardial motion *per se*.

The present measurements do show evidence of small but statistically significant differences in myocardial diffusion eigenvalues over the entire interval of contraction from end-diastole to end-systole. These differences may reflect changes in tissue architecture during contraction. The time-samples in Fig. 2.3 are cardiac phases that include the full range of contraction rates from zero up to the peak systolic motion. Accordingly, these data indicate that, in the bipolar method, the effect on diffusion contrast of any form of motion that varies with cardiac phase, is unlikely to exceed the observed dynamic range of diffusion eigenvalues of 5-10%. To the extent that the curves of Fig. 2.3 do not have the forms expected for these effects, it seems more likely that the observed changes in diffusion are reflections of changes in myocardial architecture during contraction. Detailed temporal analysis cannot be undertaken with the present data, as diffusion changes on a 50-100 ms time scale do not achieve statistical significance. Elucidation of the cause of change in observed myocardial diffusion will require further experimental study with improved sensitivity.

We also compared the bipolar method with the unipolar sweet spot method and found that they agree with each other in measuring myocardial diffusion. The agreement between the two methods provides cross-validation of both methods. First, it demonstrates that the sweet spot method is also accurate and insensitive to cardiac motion effects. Second, it validates the accuracy of the bipolar method for *in vivo* studies, since the sweet spot method is a validated method for measuring *in vivo* myocardial architectures. Third, it demonstrates that the confounding cellular fasciculation effect is not the primary component of current diffusion measurements, i.e., current methods are primarily and accurately measuring the myocardial water diffusion.

The above results demonstrate that cardiac motion effects in cardiac diffusion MRI arise mostly from the recognized effects of myocardial gross motion and myocardial strain; other unknown motion effects, if they exist, play little or no part. It also shows that the *in vivo* cardiac diffusion MRI approaches developed so far, either the unipolar sweet spot method or the bipolar method, are both accurate methods for measuring myocardial diffusion in beating hearts. However, compared with the unipolar method, the bipolar method offers clear advantages. Diffusion encoding in a single phase and the strain-independent feature of the bipolar method eliminate the complexity and potential ambiguity in the unipolar method, and enable convenient and accurate imaging of myocardial diffusion in both normal and diseased hearts at any point in the cardiac cycle, as if the heart were arrested at that point. Thus, the bipolar method is a good standard for MRI diffusion measurements in beating hearts. It has the capacity for multiple studies which previously were hard to by the unipolar method, such as fast and reliable imaging of the myocardial structure and its dynamics without contamination by cardiac motion and strain.

2.4.3 Strain effect within the bipolar pulses

The bipolar method is shown to be accurate and insensitive to the cardiac motion. However, to successfully apply this method, there is one additional experimental point that needs to be noted: the strain effect within the bipolar pulses. As previously described, the bipolar pulse limits the diffusion encoding to within the pulse duration. The two gradient lobes in the bipolar pulse are identical but opposite in sign, which in the ideal case results in a zero spatial modulation after the pulse, and so produces no diffusion sensitivity in the intervening period between the two diffusion encoding pulses. In practice, however, due to myocardial strain (which

stretches the spatial modulation within the pulse duration), the spatial modulation will not be exactly zero after the bipolar pulse. There will be some residual spatial modulation which will have diffusion sensitivity over the cardiac cycle. However, with less than 30 ms duration of the bipolar pulse, this residual spatial modulation is negligibly small. Specifically, the residual spatial modulation $\boldsymbol{k}_{residue}$ produced by the bipolar pulse approximately equals the spatial modulation $\boldsymbol{k}_B$ produced by the encoding gradient times the strain occurring in the duration δ_B of the de-encoding gradient, i.e., $\boldsymbol{k}_{residue} \approx \boldsymbol{k}_B \delta_B \dot{S}$, where $\dot{S}$ is the strain rate of the myocardium at the time of diffusion encoding. The b value $b_{residue}$ produced by $\boldsymbol{k}_{residue}$ over one cardiac cycle Δ is approximately $b_{residue} \approx |\boldsymbol{k}_{residue}|^2 \Delta = (|\boldsymbol{k}_B| \delta_B \dot{S})^2 \Delta$. It follows that over one cardiac cycle, the ratio of $b_{residue}$ to the b value produced by the bipolar pulses b_B is:

$$b_{residue}/b_B \approx (|\boldsymbol{k}_B| \delta_B \dot{S})^2 \Delta / (4/3 |\boldsymbol{k}_B|^2 \delta_B) = 3/4 \, \dot{S}^2 \delta_B \Delta \qquad (2.7)$$

In present cases, $\delta_B \approx 13$ ms, $\Delta \approx 1$ s and peak strain rate $\dot{S}_{peak} \approx 1$ s^{-1}, which indicates that $b_{residue}/b_B \approx 1\%$, which falls below present sensitivity. Thus, the bipolar pulses effectively encode the diffusion at a single cardiac phase as if the heart were frozen at that point. It is noted that this strain effect becomes significant at very much increased strain rates $\dot{S}$ or measurement times Δ, but could be ameliorated by reducing δ_B.

It is also noted that in practical experiments, other factors such as noise, imperfect pulse triggering, nonlinear effect of the strain etc. may also affect the diffusion measurement. Thus, the application of the bipolar method may not be as perfect as that in theory. Nonetheless, current experiments show that the bipolar method is capable of reducing the strain effect by at least ten folds. With improved experimental management, it is possible to increase the efficacy of the bipolar method in future studies.

2.4.4 Limitations of the bipolar method

The bipolar method is currently limited by the routinely available maximum gradient intensity for clinical MRI machines. The 40 mT m^{-1} gradient we used is the maximum available at this time, which determines the utility threshold for application to human subjects. At this gradient intensity, the required diffusion encoding time for the desired b value is long, which lengthens the TE and reduces the signal-to-noise ratio (SNR). As a result, the current bipolar method has limitations on spatial resolution and also on imaging time. On the other hand, the

motion- and strain-independent feature of this method enables acquisition of cardiac diffusion MRI with interleaved multislice across the cardiac cycle, which could be a compensation to the currently low SNR. With increased gradient intensity, the bipolar method will be able to perform higher resolution and higher efficiency studies in human subjects.

2.5 Conclusion

We presented a new cardiac diffusion MRI method which encodes diffusion in a single cardiac phase, and demonstrated that the new method is accurate and insensitive to cardiac motion and strain. We also compared the new method with previous diffusion MRI methodology valid in the normal heart, and demonstrated that both methods are accurate for *in vivo* studies. These results demonstrate that the present method has the capacity to measure myocardial diffusion accurately at any point in the cardiac cycle, as if the heart were immobilized at this point, and so offers the capacity to map myocardial fiber structure and its dynamics with little or no contamination by cardiac motion.

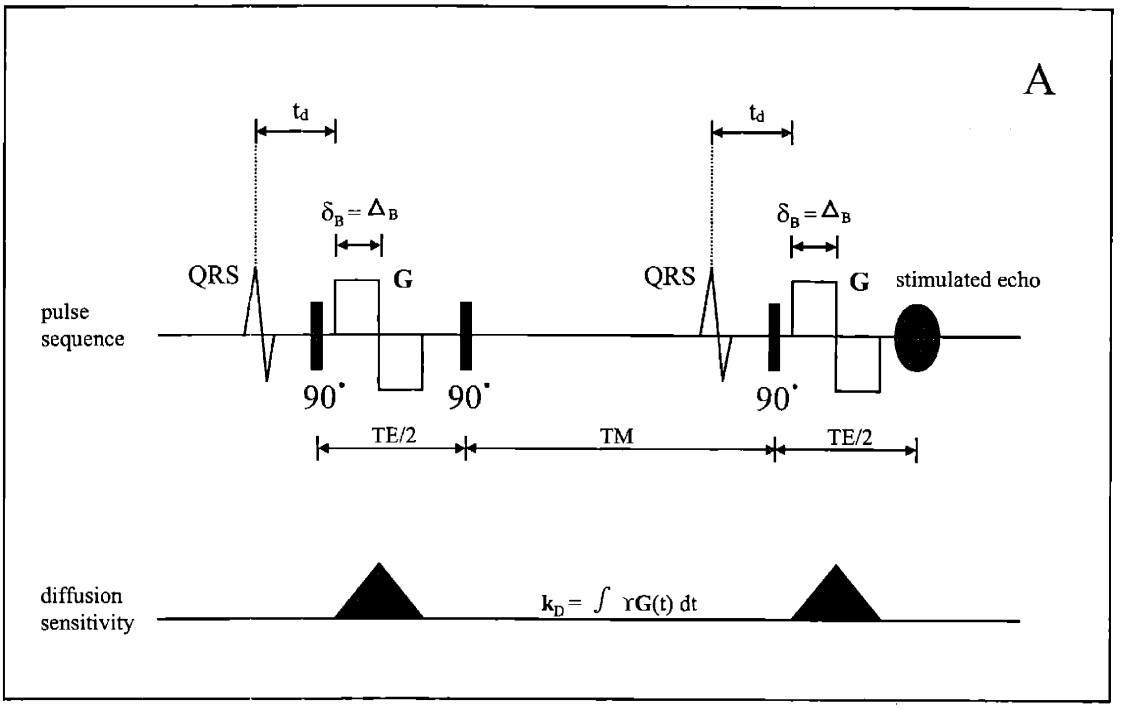

Figure 2.1. A. Strain-insensitive bipolar sequence, which uses a stimulated echo pulse sequence that incorporates two bipolar gradient pulses *G* separated by one cardiac cycle for the diffusion-encoding. Three 90° rf pulses are separated by the echo time *TE* and the mixing time *TM*. Bipolar diffusion-encoding gradients *G* follow the 1st and 3rd rf pulses. ECG triggers locate the diffusion-encoding gradient pulses *G* at identical phase delay t_d in consecutive cardiac cycles. Diffusion sensitization k_D is limited to the durations of the bipolar pulses, short compared to the contraction time, so this sequence effectively encode diffusion at single cardiac phase and is insensitive to tissue deformation (myocardial strain) during the cardiac cycle.

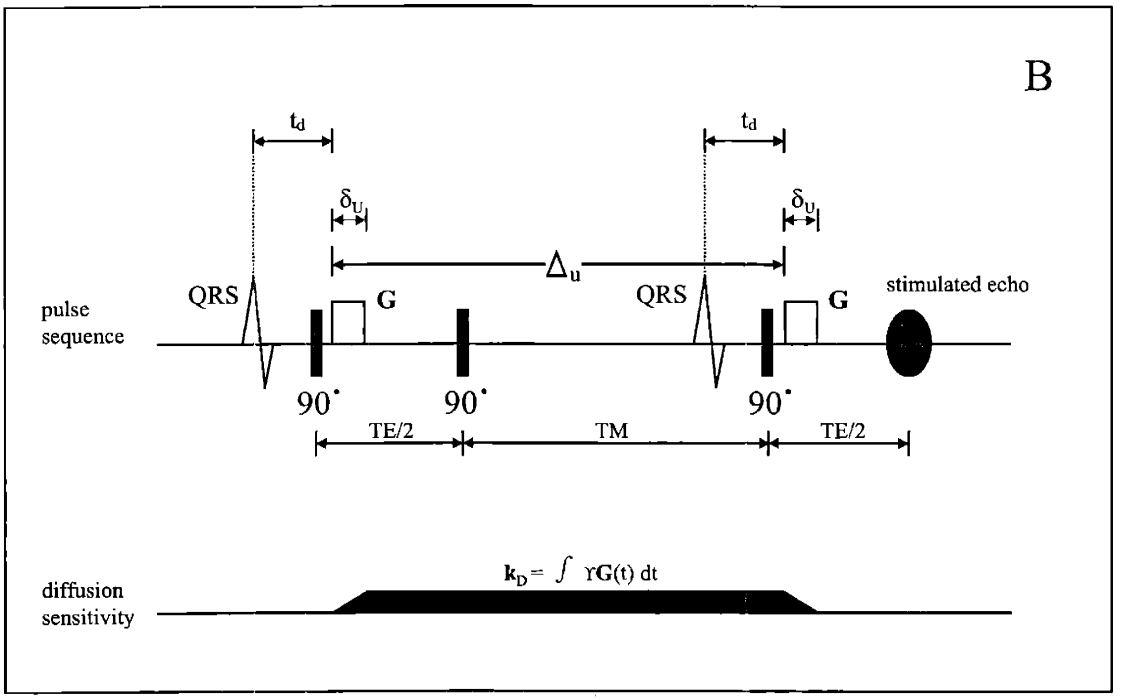

Figure 2.1 B. Strain-sensitive unipolar sequence, with same ECG-triggering and stimulated echo strategy as in Fig.1A, but each bipolar diffusion-encoding gradient pulse in Fig.1A is replaced by a unipolar diffusion-encoding gradient. Diffusion sensitization $k_D \neq 0$ during the period between diffusion encoding gradients, so this sequence is affected by myocardial strain during the cardiac cycle and is strain-sensitive.

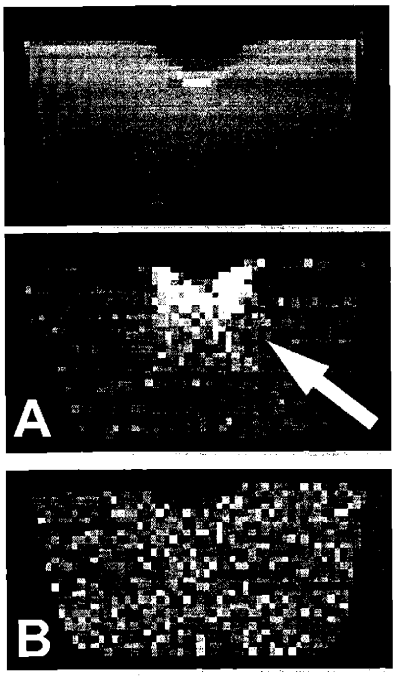

Figure 2.2 Diffusion MRI of a cyclically deformed gel phantom acquired using the unipolar and bipolar pulse sequences. The top image is the magnitude image. The center image (A) and the bottom image (B) show observed standard deviations σ of the time-series of radial component of diffusion (with polar origin at plunger contact, top center) at each pixel over the deformation cycle acquired with equal diffusion sensitivities using the unipolar sequence and the bipolar sequence respectively. The magnitudes of the σ are shown in gray scale. The arrow in A indicates the region that has apparent strain effect which is revealed by large σ; while in B, such strain effect approaches to the noise level.

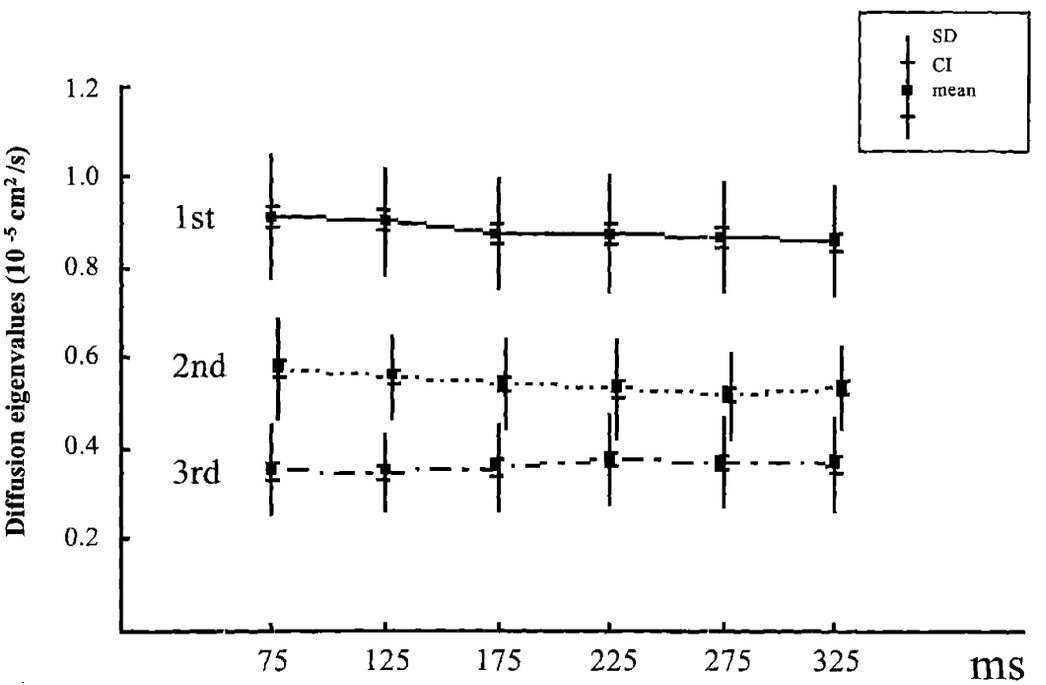

Figure 2.3 Myocardial diffusion eigenvalues (mean ± SD with bars indicating the confidence interval (CI) of the mean) measured by the bipolar method during contraction at 50 ms time steps on a normal human heart. From top to bottom: 1st, 2nd and 3rd eigenvalues respectively. The eigenvalues are nearly constant during contraction, with no statistically significant differences ($p < 0.05$) from early- to mid-systole (75ms - 175 ms delay after R-wave), or from mid- to end-systole (175 ms - 325 ms delay). For the whole range from early- to end-systole, the diffusion eigenvalues shows statistically significant change by 5-10% ($p < 0.05$).

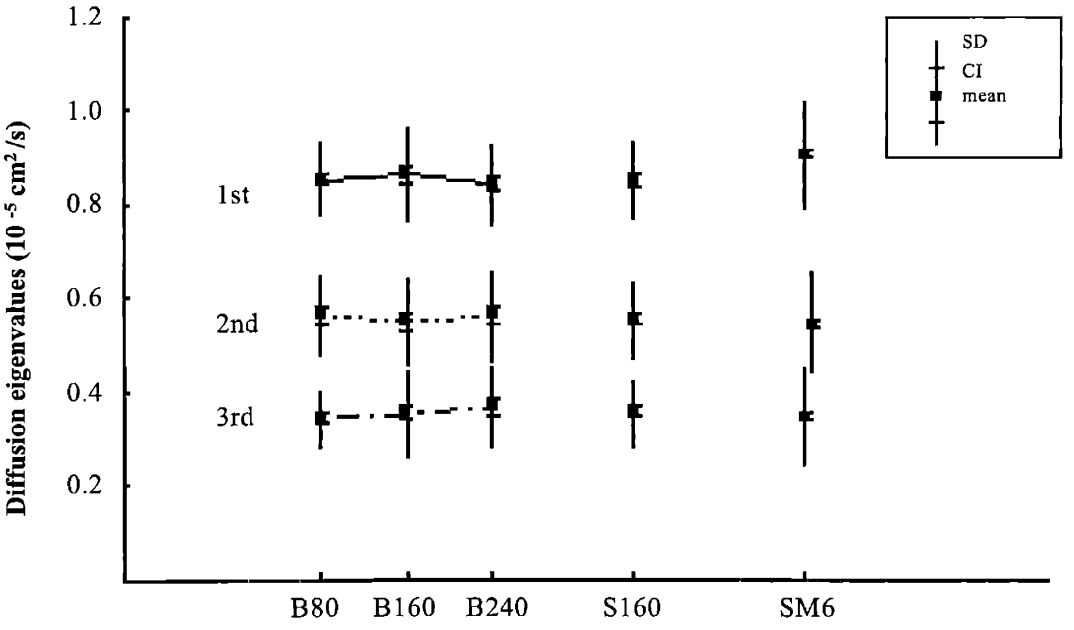

Figure 2.4 Diffusion eigenvalues measured by the bipolar method and the sweet spot method on normal subjects. From top to bottom: 1st, 2nd and 3rd eigenvalues respectively. B80, B160 and B240: bipolar results of subject S at ECG R-wave trigger delay 80ms, 160ms and 240ms respectively. S160: mid- systolic sweet spot (see text) result on subject S at trigger delay 160 ms. SM6: mean value of the sweet spot results on 6 normal subjects. It can be seen that the diffusion eigenvalues measured with the biopolar method agree with the sweet spot method. It can also be seen that the myocardial diffusion eigenvalues of different subjects are in a similar range.

Chapter 3

Myocardial Sheet and Fiber Architecture during Systole by Diffusion Imaging

3.1 Introduction

Myocardial structural motion during cardiac contraction is closely related to myocardial function. By observing the myocardial structure during systole at different phases, it is possible to obtain a picture of how the myocardial sheets function. The bipolar method developed in Chapter two provides such an opportunity. As previously shown (33,48,55-59,80), the eigenvectors of the myocardial diffusion tensor are indicators of the myocardial structure; the first eigenvector corresponds to the fiber vector; the second eigenvector corresponds to the sheet vector; the third eigenvector corresponds to the sheet normal vector. Consequently, by measuring myocardial diffusion tensors at different cardiac phases, one can mapping myocardial sheet and fiber structure at each phase. As myocardium constantly moves and deforms during contraction, the corresponding myocardial structure (sheets and fibers) will also move and change. Thus, by mapping myocardial structure at different phases during the cardiac cycle, it is possible to find certain motion patterns of myocardial sheets and fibers, and so obtain insightful information about the functional role of myocardial sheets and fibers.

In this chapter, we will apply the bipolar method to examine the myocardial sheet and fiber dynamics during contraction in normal human hearts. By observing histogram of certain geometry angles of the sheets and fibers (illustrated in Fig. 3.1), we try to obtain functional

information about the myocardial sheets and fibers. The results will be compared with previous invasive studies on canines.

3.2 Methods

Experiments were performed on a 1.5-T GE Signa MR imager. After providing written informed consent, which was approved by the hospital human study committee, the subject was instructed to use synchronized breathing to suppress respiration motion in the diffusion studies. Electrocardiogram (ECG) R-wave triggering was used for data acquisition. After a mid-ventricular short-axis slice was located, diffusion images at three points (trigger delay 80 ms (early- systole), 200 ms (mid-systole) and 320 ms (end-systole)) in the cardiac cycle were then acquired using the bipolar method with spatial resolution of 4 x 4 x 12 mm. The diffusion-encoding gradient intensity used was $|\boldsymbol{G}_B| = 40$ mT m^{-1}, pulse duration $\delta_B = 13.2$ ms, furnishing a diffusion sensitivity $b \approx 350$ s mm^{-2}. $TE = 82$ ms and $TR = 4$ R-R intervals were used in all acquisitions. The heart rate of the subject was stable during the experiment. The total imaging time per study is under 10 minutes.

After the quality of acquired images was assured by examining both the magnitude and phase images, myocardial diffusion tensors were calculated at each image pixel. The eigenvectors of the myocardial diffusion tensor were then calculated to define the sheet structure (with first eigenvector corresponds to the fiber vector, second eigenvector corresponds to the sheet vector, and the third eigenvector corresponds to the sheet normal vector). Sheet and fiber dynamics during systole were then studied by examining the histograms of sheet angle θ_S and helix angle θ_H at these points. At each pixel, let $\boldsymbol{d}_1$, $\boldsymbol{d}_2$ be the first and second eigenvectors of the diffusion tensor, $\boldsymbol{c}$ be the circumferential unit vector, defined as the normalized gradient of the polar angle about the left ventricular centroid, and $\mathbf{r}$ be the radial unit vector with origin at the left ventricular centroid. The fiber vector $\boldsymbol{f}$, sheet vector $\boldsymbol{s}$, and sheet normal vector $\boldsymbol{n}$ are defined as:

$$\begin{aligned} \boldsymbol{f} &= \text{sign}(\boldsymbol{d}_1 \cdot \boldsymbol{c})\, \boldsymbol{d}_1 \\ \boldsymbol{s} &= \text{sign}(\boldsymbol{d}_2 \cdot \boldsymbol{r})\, \boldsymbol{d}_2 \\ \boldsymbol{n} &= \boldsymbol{f} \times \boldsymbol{s} \end{aligned} \qquad (3.1)$$

Let $f_\perp$ be the unit projection of f onto the epicardium tangent plane, i.e., the circumferential-longitudinal (c-l) plane, where $l = r \times c$, and $r_\perp$ be the unit projection of r onto the plane formed by s and n. The sheet angle θ_S is then defined as the angle between the sheet normal vector n and the radial projection vector $r_\perp$:

$$\theta_S = \text{sign}(r_\perp \cdot n) \arccos(|r_\perp \cdot n|) \tag{3.2}$$

The helix angle θ_H is defined as the angle between the circumferential vector c and the fiber projection vector $f_\perp$:

$$\theta_H = \text{sign}(f_\perp \cdot l) \arccos(|f_\perp \cdot c|) \tag{3.3}$$

The slice examined is at left mid-ventricle (with papillary muscle excluded). We expect that the histogram of these two angles will change during contraction because of the motion of myocardium, from which we will derive how sheets and fibers move in this process, and so obtain functional information about the sheets and fibers.

3.3 Results

Figure 3.2 shows the myocardial structure measured by the bipolar method at ECG R-wave trigger delays 80 ms, 200 ms and 320 ms. The images show classic distribution of fiber orientations from epicardium to endocardium. Examining through the time course shows that the sheets become more radially oriented during contraction, and the sheets in the septum and the freewall tilt in parallel in this period. Fiber helix angle changes during contraction can not be observed directly from the images, but are revealed in the histogram analysis in Figure 3.3.

Figure 3.3A shows the histograms of the sheet angle θ_S at ECG R-wave trigger delays 80 ms (early-systole), 200 ms (mid-systole) and 320 ms (end-systole). From this histogram "movie," we see that the histogram becomes broader from 80 ms (sheet angle SD 24°±3°(CI)) to 320 ms (sheet angle SD 41°±4°), indicating the sheets become more radially oriented during contraction. This result is in qualitative agreement with the result on canine hearts by LeGrice et al. (30), who found that the myocardial sheet's flipping to the radial direction (sheet shear) contributes to systolic wall thickening. Figure 3.3b illustrates the functional meaning of this result.

Figure 3.4a shows the histograms of the helix angle θ_H during contraction. We see that the histogram becomes broader from 80 ms (helix angle SD 36°±4°) to 320 ms (helix angle SD 44°±5°), indicating the fibers become more longitudinally oriented during this period. This result is in qualitative agreement with the result on canine hearts by Streeter et al (88), who found that the myocardial fibers of left ventricle become more longitudinally oriented during systole. Figure 3.4b illustrates the meaning of this result.

3.4 Discussion

Using the bipolar method, we examined the myocardial sheet and fiber dynamics during systole in a normal human heart. The results showed that the myocardial sheets became more radially oriented, and the fibers became more longitudinally oriented, in agreement with previous results on canine hearts.

The motion- and strain-independent feature of the bipolar method makes it possible to study the myocardial sheet dynamics noninvasively in the cardiac cycle. The myocardial sheet is a recently observed laminar organization of the myocardium (20,89,90), whose function is still a matter of active study. Study of the myocardial sheet in the past was mostly based on histology (30,31). Cardiac diffusion MRI offers the possibility to study the sheet structure noninvasively (55,56). In beating hearts, the unipolar method has difficulties in studying the sheet dynamics due to the complexities of the strain effect which disrupts diffusion tensor measurements at points other than the sweet spot. The bipolar method, however, is strain-independent and able to measure the sheet structure accurately at any point in the cardiac cycle. Our results on sheet dynamics in a normal subject using the bipolar method show that the sheets become more radially oriented during systole. The changes of the sheet angle during systole indicate that the sheet shear contributes to radial thickening, which is in agreement with the results on the canine hearts by LeGrice et al. (30), who found that the myocardial sheet shear can account for a substantial proportion of systolic wall thickening. Since sheet shear is considered to be cellular rearrangement of the myocardium, our results on sheet dynamics show the existence of cellular rearrangement in the living human heart. The observation in our results, that the sheets in the septum and freewall tilt in parallel, is also in agreement with the results on canine hearts by

LeGrice et al., who found that the longitudinal-radial shear of the sheets in the septum and anterior freewall are opposite in sign.

The studies of the fiber dynamics in the past were typically based on histology (88) or used radio-opaque markers (91) within limited regions of the heart. The bipolar method offers the possibility to study the fiber dynamics directly and noninvasively with the capability to examine any region of the heart. Our results on normal human subjects using the bipolar method show that the myocardial fibers of the left mid-ventricle become more longitudinally oriented from early systole to end systole, which may indicate the torsion motion of the heart during contraction. This result is in agreement with the result using canine hearts by Streeter et al (88), who found that the myofibers of left ventricle become more longitudinally oriented from end-diastole to end-systole. In Streeter's method, different canine hearts arrested at end-diastole and end-systole were used to observe the fiber dynamics, which is invasive and also requires careful and labor-intensive sample preparations. The bipolar method described here is able to study the same heart at multiple points in the cardiac cycle both noninvasively and efficiently, which offers clear advantages in examining the fiber dynamics.

It is noted that current experiment used large spatial resolution 4x4x12 mm to achieve enough signal-to-noise ratio (SNR). Although the results show that current spatial resolution is effective in imaging the myocardial fiber and sheet architecture, further study will be required to assess the suitability of this resolution for clinical application.

3.5 Conclusion

Using cardiac diffusion MRI, we mapped myocardial sheet and fiber architecture during systole in normal humans, and found evidence that myocardial sheet structure undergoes remarkable changes during systole. Specifically, myocardial sheets tilt toward radial and fibers tilt toward longitudinal during contraction, which is in agreement with previous results on canine hearts. These results suggest that sheet shear is an important mechanism for ventricular wall thickening.

Sheet angle:

$\theta_S = \text{sign}(\boldsymbol{r}_\perp \cdot \boldsymbol{n}) \arccos(|\boldsymbol{r}_\perp \cdot \boldsymbol{n}|)$

for sheet dynamics

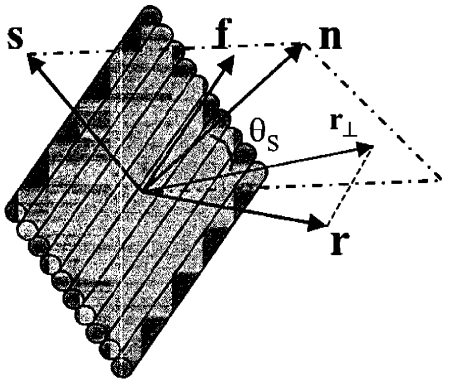

Helix angle:

$\theta_H = \text{sign}(\boldsymbol{f}_\perp \cdot \boldsymbol{l}) \arccos(|\boldsymbol{f}_\perp \cdot \boldsymbol{c}|)$

for fiber dynamics

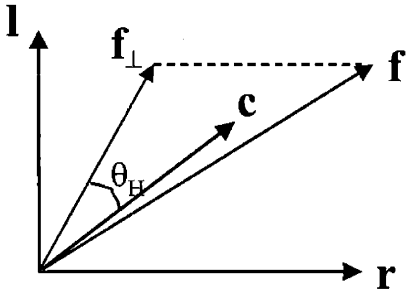

Figure 3.1 Definition of sheet angle and fiber angle. **f**: fiber vector; **s**: sheet vector; **n**: sheet normal vector; **l**: longitudinal vector; **c**: circumferential vector; **r**: radial vector; $\mathbf{f}_\perp$: the unit projection of **f** onto the epicardium tangent plane, i.e., the circumferential-longitudinal (**c-l**) plane; $\mathbf{r}_\perp$:the unit projection of **r** onto the plane formed by **s** and **n**.

.

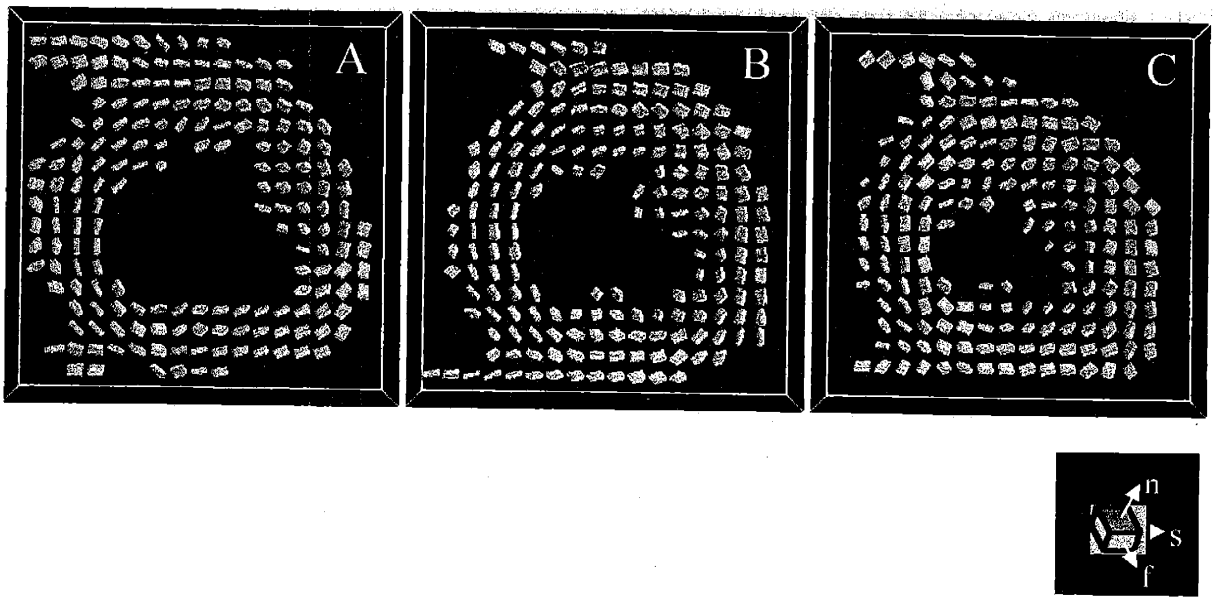

Figure 3.2. Fiber architecture of a left mid-ventricle short axis slice during contraction measured by the bipolar method at ECG R-wave trigger delay 80 ms (A), 200 ms (B) and 320 ms (C). The fiber architectures are represented by colored boxes, with fiber ***f***, sheet ***s***, sheet normal ***n*** vectors perpendicular respectively to red, green and blue-colored surfaces viewed from above the slice. The anterior wall is at the top and the septum is at the left in each image. The images show classic distribution of fiber orientations from epicardium to endocardium. The first column of images clearly show that the sheets become more radially oriented during contraction (sheet axis becomes more perpendicular to the viewing axis from image A to C). Note also the sheets in the septum and the freewall tilt in parallel during contraction.

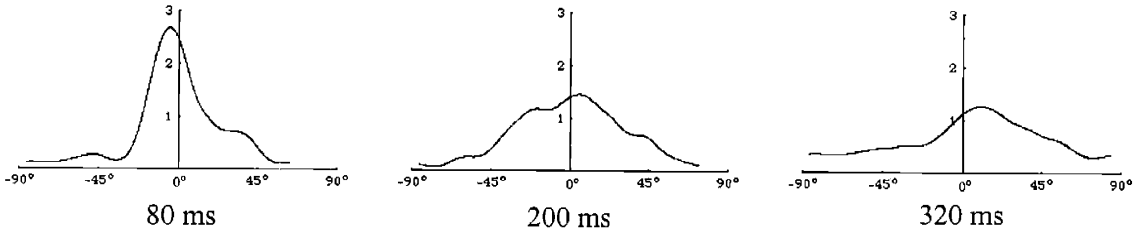

(a)

(b)

Figure 3.3. (a) Histograms of sheet angle θ_S of a left mid-ventricle short axis slice during contraction measured by the bipolar method at ECG R-wave trigger delays 80 ms (early-systole), 200 ms (mid-systole), and 320 ms (end-systole). 0° represents sheets that have radially oriented sheet normal, angles away from 0° represents sheets that have more longitudinally oriented sheet normal. The histogram becomes broader from 80 ms to 320 ms, indicating the sheets become more radially oriented during contraction. (b) Illustration of the functional meaning of the result in (a). The flipping of sheets (sheet shear) contributesto ventricular wall thickening.

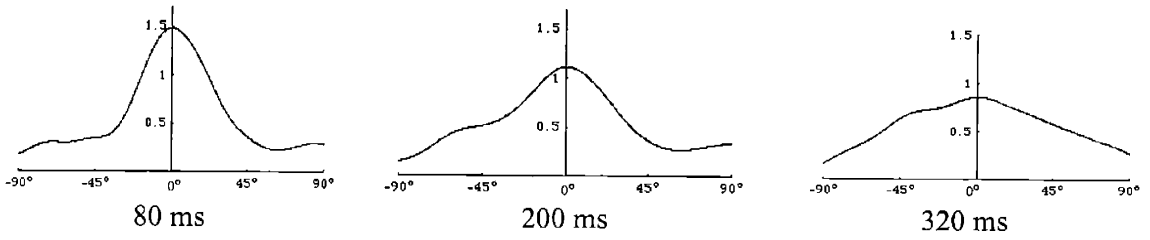

(a)

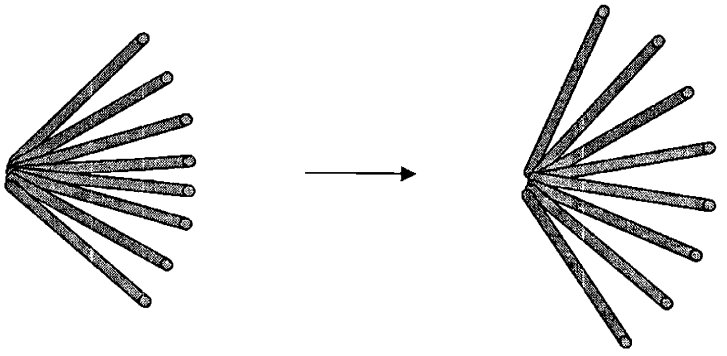

(b)

Figure 3.4. (a) Histograms of fiber helix angle θ_H of a left mid-ventricle short axis slice during contraction measured by the bipolar method at ECG R-wave trigger delays 80 ms (early-systole), 200 ms (mid-systole), and 320 ms (end-systole). 0° represents circumferentially oriented fibers, and angles away from 0° represents more longitudinally oriented fibers. The histogram becomes broader from 80 ms to 320 ms, indicating the fibers become more longitudinally oriented during contraction. (b) Illustration of the meaning of the result in (a). The cylinders represent myofibers, which become more longitudinally oriented during contraction.

Chapter 4

MRI of Myocardial 3D Strain/Strain rate

4.1 Introduction

To understand the role of myocardial sheets, in previous chapter, we applied diffusion MRI to observe the motion of the sheets using histograms of sheet angles, from which we found that sheet shear is an important mechanism that contributes to ventricular wall thickening. However, for a more complete understanding of how sheet functions, the observation of sheet angles is not sufficient. The change of sheet angles only reveals one pattern of sheet motion – the sheet shear. It is possible that the motion of sheets may have other patterns that can not be revealed using the analysis of sheet angles. In order to reveal other possible motion patterns, mechanical information of myocardial deformation (strain/strain rate) must be measured. The myocardial strain/strain rate can be registered with the underlying sheet structure to derive the motion pattern of the later, and so give us a detailed insight into the functional role of myocardial sheets. To measure mechanical information of the myocardium, MRI techniques that could quantify myocardial 3D strain/strain rate must be developed.

As previously described, myocardial 3D strain can be measured using MR tagging or MR velocity encoding techniques (Chapter 1). MR tagging is limited by spatial resolution and also tedious task of postprocessing of images. Since study of myocardial structure-function relations requires fine spatial registration between structural and functional data and also desires ease of data processing, the tagging method is not an ideal technique for this task. The velocity encoding method, however, can have higher spatial resolution and also can be more easily automated.

Thus, we choose velocity encoding method to quantify myocardial strain/strain rate in our investigation of myocardial structure-function relations.

To imaging the myocardial 3D strain/strain rate, the image data must cover a 3D volume of at least two contiguous 2D slices, so that both in-plane and through-plane strain/strain rate can be calculated. A previous method accomplished this by collecting adjacent slices at different heart beats using a single-shot spin-echo echo-planar imaging (EPI) sequence augmented by velocity encoding bipolar gradient pulses (80). This method, though effective, has a through-plane noise issue which comes from its strategy of splitting measurement of the two adjacent slices on different heart beats. The position shift of slices along the through-plane axis due to beat to beat variations can cause large noise in the calculation of the spatial derivative along the through-plane direction. To overcome such noise, lots of averages and postprocessing supervision are required, which reduce the efficiency and automaticity of the method. In order to solve the problem of through-plane noise in previous method. New ways that are able to acquire two adjacent slices simultaneously within the same heartbeat are desired.

In this chapter, we will present a new MRI method of myocardial 3D strain/strain rate imaging that is capable of collecting the two adjacent slices simultaneously within the same heart beat. This new method is developed in our lab by Reese et al.

4.2 Methods

4.2.1 Data acquisition and reconstruction

In this method, special techniques are applied to collect sufficient information for reconstruction of two adjacent slices simultaneously using a single-shot EPI. The acquisition consists of a pair of closely spaced 90 rf excitations, with slice selective and frequency selective gradient encoding designed to generate separate echoes, one for each slice, in a conventional EPI readout.

Figure 4.1a and b shows two versions of the pulse sequences of the new single-shot 3D strain MRI. One uses a gradient-recalled echo (GRE) with bipolar velocity encoding gradient (1a), which measures the strain rate. The other uses a stimulated echo (STE) where the unipolar strain-encoding gradients are separated by the mixing time (TM) (1b). The STE sequence measures the total strain S over the evolution time between strain-encoding gradients. To encode

two slices with effective simultaneity, two slice selective rf pluses are placed as close in time to each other as possible given the constraint of time needed for the read out pre-encode and slice refocusing – typically about 2.5ms. The two slice selective pulses are separated by a slice refocusing gradient and a read gradient dephasing pulse with half the area (amplitude times duration) of a trapezoidal readout gradient lobe. The readout pre-encoding separates the slices in spatial-frequency (k-space). This results in two gradient echoes being refocused concurrently with each read gradient switching, one echo for each slice, separated by half the total readout excursion in K_x (cm-1). The pre-encoding are selected such that the two echoes are separated sufficiently to allow for minimum-phase-gradient complex reconstruction without using conjugate synthesis (part-K) methods. An additional readout dephasing gradient is applied prior to the EPI readout to center the echo pairs in each EPI readout gradient lobe. Time separation between the echo pairs in the readout equals about 350 μs.

The read out acquisition consists complex raw data of two echoes. In postprocessing, the complex raw data are divided in half along the middle of the read axis and reconstructed each half (corresponding to one slice) separately. To accomplish this, the read out axis contains twice as many time points as the image of each slice, i.e. two 64x64 images would require 128x64 raw data points in each acquisition, the same of doubling the spatial resolution in the readout axis with the same field-of-view (FOV). Figure 4.1c and d demonstrates the procedure of this technique using strain phantom.

4.2.2 Strain calculation and display

To imaging strain-rate of each slice, velocity encoding gradient pulses are applied in tetrahedral orientations corresponding to nonopposed corners of a cube (92). After signals of the four velocity encoding directions are obtained, the velocity field V in each Cartesian coordinate direction can be calculated. The strain rate (or, similarly, strain) tensor fields can then be computed form the velocity field data by using:

$$S_{ij} = (1/2)\,(\delta V_i/\delta x_j + \delta V_j/\delta x_i) \qquad (4.1)$$

where V_i and S_{ij} are artesian components of the velocity field V and strain rate tensor field $\boldsymbol{S}$, i and j are coordinates indices, and δx_i is the differential between pixels adjacent in the x_i direction.

The calculated strain tensor has an abundance of information of myocardial deformation, including eigenvectors and eigenvalues. To display the rich information contained in the strain rate tensor, we developed two graphic methods to encode the critical mechanical information.

The first method is to present the strain eigensystem as rectangular box icons three dimensionally rendered in space. Each eigenvector $\mathbf{s}_i$ is normal to one surface of the box, with the expression for the central axes $\mathbf{A}_i$ of the box:

$$\mathbf{A}_i = \pm (1+\alpha\lambda_i)\, \mathbf{s}_i,\ i = \{1,2,3\} \tag{4.2}$$

Giving the length of the side corresponding to the associated eigenvalue λ_i times a scaling constant α. The expression gives positive and negative eigenvalues a positive length. Thus, a cube represents zero strain or strain rate, with positive or negative then lengthening and shortening respectively. Each face of the box is color coded red, green or blue, indicating the largest to smallest eigenvalues respectively.

The second method is to use color-encoded graphics that are constructed from train rate tensor eigenvalues. Using hue, saturation, and brightness (HSB) color model, we display strain rate tensor "shape" is displayed with color hue, strain rate amplitude is displayed with color saturation, and anatomic background is displayed with brightness. Color hue is assigned using the skewness of the eigenvalues $\xi(\lambda)$, with $\xi(\lambda)>0$ coded red, $\xi(\lambda)\approx 0$ coded green, and $\xi(\lambda)<0$ coded blue. Color saturation is determined using the net strain rate amplitude $\|S\|$. Brightness is calculated according to the mean magnitude z of the constituent MR images. The math expressions of the calculation of the above three color codes are as follows:

$$\text{Strain Rate Tensor Shape (hue): } \xi(\lambda) = \sigma_\lambda^{-3} \sum_i \lambda_i^3$$

$$\text{Strain Amplitude (saturation): } \|S\| = \sqrt{tr(\mathbf{S} \bullet \mathbf{S}^T)} \tag{4.3}$$

$$\text{Anatomy (brightness): } \bar{z} = \frac{1}{N} \sum_n \|z_n\|$$

Where σ_λ is the standard deviation of the eigenvalues and tr( ) is the trace operator.

4.2.3 Validation

To validate the new method, we first tested its performance using a gel phantom (as described in Chapter 2), then we applied it on healthy *in vivo* human heart and brain to demonstrate its effectiveness for clinical applications.

Both phantom and *in vivo* data was collected using a GE 1.5T Signa Lightning MR scanner (General Electric Medical Systems, Milwaukee WI), LX 8.2.5 equipped with the CRM gradient set (40 mT/m, 150 mT/m-ms). GRE scans had an echo time (TE) of 47 ms (heart) or 80 ms (brain) with a bipolar strain encoding gradient with velocity sensitization (VENC) of 4.5 cm/s (heart) or 0.23 cm/s (brain). Slice thickness for each excitation was 5 mm with no gap between, and a 12-mm separation between acquisitions. Cardiac scans used a 20 cm x 12 cm flexible linear surface coil designed and built in our laboratory. Brain images were acquired with the GE head coil. With STE, the mixing time TM = 100ms, TE = 61 ms, and VENC = 6.3 cm/s (heart). The field of view was 24x24 cm, with in-plane resolution of 3.75 mm. The EPI readout time is 50.2 ms. Using the above GRE and STE prescription, each 3D strain and strain rate image was collected in 8 EPI shots, one shot per heartbeat, with a strain contrast-to-noise ratio of 15:1 or better. To test the efficiency of this method, we collected 7 slices in 7 cardiac phases over 8 strain encoding direction for 56 heartbeat in total. These acquisitions were collected in 8 seven heartbeats breath holds interspersed with 7 five second breathing pauses for a total measurement of about 90 seconds. All human studies were carried out with informed consent using an IRB-approved research protocol.

4.3 Results

Figure 4.2 shows the strain measurement performance of this sequence using a synchronized plunger phantom method described in Chapter 2. The strain field was represented using color coded boxes described in method 1. It can be seen that both the GRE (Fig. 4.1a) and STE (Fig. 4.1b) forms of the pulse sequence performed as expected; the intensity and direction of the measured strain field matched the predicted deformation of the gelatin phantom. Figure 4.2a shows the gel deformation resulting from the acquisition-synchronized plunger. Due to tissue incompressibility, the trace of the strain tensor must always be zero. The trace of the strain tensor at each pixel within the phantom was calculated and found to be uniformly zero within the

range of background noise. Figure 4.2b shows velocity components of each slice during the plunger stroke, and Fig. 4.2c shows calculated material deformation gradient tensor components. Using the STE sequence, the eigensystem at each voxel in the gel was measured during plunger tension (up stroke) and compression (down stroke) and was displayed as iconic fields (Fig. 4.2d). Using the GRE sequence, strain rate in the gel was also measured and displayed in the HSB color code described above (Fig. 4.3).

In vivo testing in normal human subjects demonstrated the effectiveness of the twin echo acquisition in measuring strain, and was in good agreement with previous 3D phase contrast methods (80). Strain-rate data of the human heart are displayed as iconic fields in Fig. 4.4a and b. It can be seen that the transmural thickening with contraction is evident, along with the pitch of the blocks due to myocardial twist. Figure 4.5 shows normal net systolic strain, measured from 100-350 ms post R-wave using the STE sequence (Fig. 4.1b). The pitch of the box icons results from myocardial twist. Note that there are 4-6 pixels across the wall thickness, and that the transmural strain resolution is the same as the image resolution.

Fig. 4.4c use color maps of eigenvalue skewness and amplitude to display the multislice multiphase data. The color skewness maps present the contraction speed and contraction state (contraction vs. relaxation). The relative amplitude of the eigenvalues, indicating rate of contraction or relaxation, is shown by the color of the pixels. Easily seen is the uniform contraction in systole, and the transition from systole to diastole in each level of the heart. At 180 ms and 270 ms delay following ECG trigger, the color is bright and uniformly red, indicating the myocardium is moving fast and lengthening radial to the cardiac long axis. Systolic contraction lingers longest at the cardiac apex, and dysynergic transition to diastole is clearly seen. It can also be seen that all regions of the heart do not relax uniformly, which is characteristic of the normal heart as reported in the echocardiography literature (93). Previously observed in bead-labeled radiography studies (94), the mechanical stages of normal diastole – isovolumic untwisting, followed by radial thinning, then untwisting – can also be seen in figure 4.4c as change in color – green to blue to green – based entirely on the local pattern of deformation at each pixel.

4.4 Discussion

Our results show that the new method is valid in both phantom study and *in vivo* study on normal human hearts. In phantom study, it produced strain field that matched the predicted deformation field. In *in vivo* study, it successfully detected with 3D quantitation physiologic features previously reported only qualitatively in the 2D echocardiography literature (93) or detected invasively by radiographic tags (94). It also showed fast imaging ability (on the order of tens of seconds) with efficient multislice and multiphase acquisitions, which makes it possible for clinical applications such as cardiac stress tests.

Previous method realized the 3D strain imaging by using 2D EPI to collect adjacent slices in different heartbeats to calculate 3D strain. However, the strategy of splitting measurement of the two adjacent slices on different heartbeats could induce large through-plane noise. Because there is beat to beat variations, the two adjacent slices may not be exactly registered as adjacent slices. Defining in plane axis as x,y, and through plane as axis z, this kind of misregistration does not have much influence on calculating in-plane spatial derivatives of velocity $\delta V_i/\delta x$ or $\delta V_i/\delta y$, in which δx or δy is fixed (one pixel length) and the only influence comes from the variations of δV_i (velocity difference between pixels). Since the variation of δV_i from beat to beat is relatively small (such as 10%), and also because in-plane spatial derivatives are calculated from two slices and then averaged, the noise induced by beat to beat variations on in plane spatial derivatives is thus small and well confined. However, situations are different when considering the through plane spatial derivative $\delta V_i/\delta z$, which are influenced not only by δV_i but also by through-plane spatial derivative δz. While the beat to beat variations of δV_i are relatively small, the beat to beat variations of δz is not. In practical cases, it is possible for a through-plane displacement to be as large as 1 mm from beat to beat. Considering common cases of measured velocity with a 3 mm slice thickness, this 1mm deviation from assumed δz (3 mm) will cause the spatial derivatives $\delta V_i/\delta z$ to have a large 30% error, which is not acceptable for quantification studies. To reduce this kind of through-plane noise, lots of averages are required which lengthens the scanning time. Moreover, to ensure maximum calculation accuracy, subjective postprocessing supervision is required to exclude those bad images which have obvious through-plane artifacts. The supervision during data processing inevitably reduces the automaticity of data analysis. Thus, to

obtain high quality strain data using previous method, one needs to sacrifice scanning time and automaticity of data analysis, which are not favorite characteristics for clinical applications.

Compared with previous method, the new method successfully addressed the through-plane noise problem. By encoding the two adjacent slices simultaneously within one heartbeat, the through-plane displacement between the two slices caused by beat to beat variations is reduced to minimum. Thus, the large error of through-plane spatial derivatives $\delta V_i/\delta z$ that arise from the beat to beat variations of δz in method 1 is effectively avoided. Acquiring enough data to measure the strain tensor using method 2 still requires multiple EPI shots, and shot to shot variability persists as the normal variation of strain between heart beats. However, since method 2 effectively eliminates the beat to beat variations of δz, the only influence on $\delta V_i/\delta z$ comes from δV_i, which makes the through-plane derivative data has quality as good as that of in-plane spatial derivatives. Thus the noise in 3D strain calculations are significantly smaller than that in method one. The reduce in noise makes the scanning time shorter as less averages are required to achieve desired accuracy. Moreover, the reduction of through-plane noise also save the task of postprocessing supervision which is required in previous method; this means that the 3D strain encoded images measured by current method can be processed in an entirely unsupervised or 'turnkey' manner, and strain images can be presented as rapidly as acquisition proceeds, providing near real-time strain imaging rather than calculation of strain from images following the MRI scan.

The new method also has very high phase sensitivity. In practice, phase sensitivity using the current 3D strain MRI to measure 3D strain approaches the fundamental imaging limit: spatial derivatives approaching $\pm\pi$ radians per pixel (79,95). This represents a phase dynamic range that is greater by at least an order of magnitude than the usual phase contrast limit which requires dynamic range less than $\pm\pi$ over the entire image. Combined with the near-perfect velocity selectivity of phase contrast methods, measurements of strain over very short intervals and at very small relative displacements become possible.

Strain rate due to brain parenchymal motion (96) provides a useful demonstration of the strain sensitivity achievable using the current method. Fig. 4.6 shows strain rate of the normal human brain due to vascular pulsatility and resulting brain parenchymal motion (97-99). This image uses a VENC of 0.23 cm/s compared to a VENC of 4.5 cm/s used in collecting the cardiac strain-rate images in Fig. 4.4. Equivalently, Fig. 4.6 corresponds to a strain rate of 0.1 s^{-1},

compared to the 1-2 s^{-1} that is typical of the myocardial during the systole. In the human brain the total tissue excursion in general does not exceed 0.5 mm (98), and the relative or intravoxel displacements are much smaller. The strain measurement of Fig. 4.6 shows displacements with a dynamic range of $|l \Delta dS_{max}/dt| < 6 \mu$ per voxel, where $l = 3.5$ mm is the voxel dimension and $\Delta = 0.016$ s the measurement interval (limited by the image noise to an experimental precision of ±200 nm). At these very small relative displacements, signal loss due to diffusion attenuation (here with a 32 ms bipolar gradient at 40 mT/m, the diffusion sensitivity b value is about 300 s/mm^2, corresponding to an attenuation of ~60%) becomes the relevant physical barrier. In addition to potential application to the study of CSF circulation, brain strain rate images could also be useful for predicting diffusion-encoding artifacts due to pulsatile motion.

While the new method successfully resolves the noise problem in previous method and saves scanning time significantly, it is not at no cost. Most obvious is the increased readout time required by doubling the number of pixels per EPI shot. In practice, rather than doubling the readout time, the slew rate and maximum amplitude of the read out gradient impose a more-or-less fixed ramping time for trapezoidal readouts with useful FOVs, requiring about a 50% increase in readout gradient time for a doubling of gradient area. Increasing the gradient readout time with the same phase encode gradient bandwidth produces additional susceptibility artifact, which can be especially problematic in the cardiac posterior wall. Thus, effective localized shimming is required in order to reduce the posterior wall susceptibility artifact and acquire image data of diagnostic quality. In addition to minimizing susceptibility gradients, as with the shimming method, sensitivity to susceptibility gradients can also be reduced with shorter readout times using faster, stronger field gradient hardware, selecting reduced phase-encode FOVs with selective inner volumes, or multicoil-multichannel methods such as simultaneous acquisition of spatial harmonics (SMASH) and sensitivity encoding (SENSE) (100,101). These and other methods of addressing cardiac susceptibility artifacts in single shot EPI are topics of further research.

In overall capability, the current 3D strain method provides a combination of features that were previously unavailable with a single technique – high temporal resolution, easy and quantitative 3D analysis, as well as excellent motion sensitivity. The spatial resolution of spin-warp MRI can exceed that of single shot methods such as EPI, but motion artifact severely limits the sensitivity of spin-warp acquisition. Some notable enhancements to myocardial tagging is

able to match the spatial resolution of single-shot phase contrast methods (102,103), although quantitation of tagged images requires a heavy processing burden. While the temporal resolution of 3D phase contrast strain MRI can not match that of real-time cardiac echo, it substantively exceeds that of any other 3D strain MRI technique.

4.5 Conclusion

We described 3D phase contrast strain and strain rate imaging using single-shot 3D MRI. Following validation using a strain phantom, we demonstrated the effectiveness of our 3D single-shot strain method in healthy *in vivo* human heart and brain. Compared to previous phase contrast methods, the new method realizes potential sensitivity of phase contrast EPI, significantly improves image quality regarding noise and artifact, requires much shorter acquisition time with only routine patient supervision, and can be quickly and automatically processed without operator supervision. The new 3D strain MRI is a powerful tool for quantifying myocardial 3D strain.

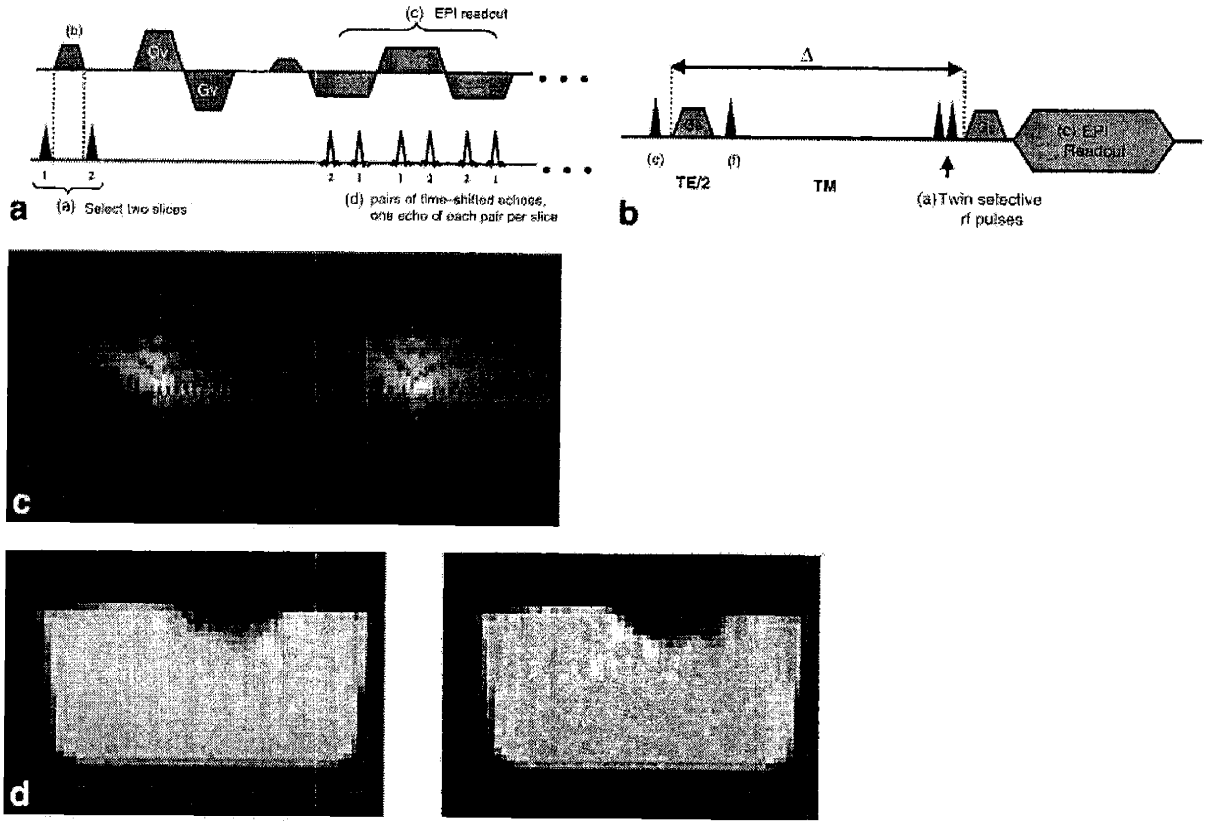

Figure 4.1 Pulse sequence diagram and k-space data. **a**: the GRE version of the EPI pulse sequence uses two slice selective 90 RF pulses to excite two adjacent slices with effective simultaneousness. The RF pulses are separated by a slice refocusing gradient pulse and a read gradient dephasing pulse (b) with half the area of a trapezoidal readout gradient lobe. This results in two gradient echoes being refocused concurrently with each read gradient switching, one echo for each slice, separated by half the total readout excursion in K_x (cm^{-1}) An additional readout dephasing gradient (c) prior to the EPI read out (d) centers the echo pairs (e) in each EPI readout gradient lobe. Bipolar encoding gradients Gv encodes the strain rate. **b**: STE version of the pulse sequence to encode strain over an time interval uses the previous slice selection strategy preceded by two nonselective excitation pulse (e) and (f) separated by TE/2. Two constant gradients Gs encodes the net strain over the evolution time between the encoding gradients. **c**: k-space data of the two echoes from the two adjacent slices. **d**: Reconstructed images of the two slices from the two echoes. (Illustrations are provided by Reese)

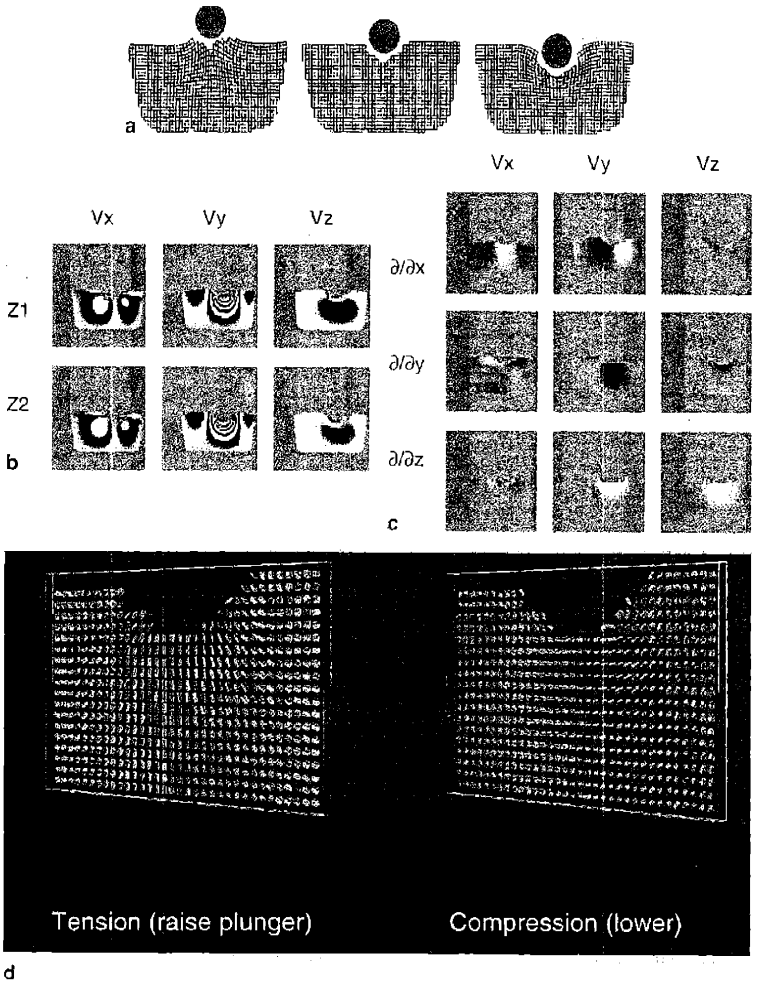

Figure 4.2 Strain phantom validation. **a**: Gel phantom strain results from deformation due to an acquisition-synchronous impact by a plunger. The gel takes the shape of the container. The hemispherical plunger (gray disk) located over the center of the container rests on the surface of the gel (center, no strain) or is lifted (left, causing tension in the gel) or lowered (right, causing compression). **b**: 3D velocity maps derived from the two slices for each shot acquisition show aliased phase (phase difference between adjacent pixel $< \pm\pi$) due to material strain resulting from the plunger impact. **c**: Components of the material deformation gradient $E_{ij} = \delta V_i/\delta x_j$, generated by taking the spatial derivative of the velocity maps, are automatically dealiased. **d**: STE 3D strain MRI of the gel phantom. The eigensystem at each voxel in the gel was measured during plunger tension (up stroke) and compression (down stroke) and was displayed as iconic fields. It can be seen that the intensity and direction of the measured strain field matched the predicted deformation of the gelatin phantom. (Illustrations are provided by Reese)

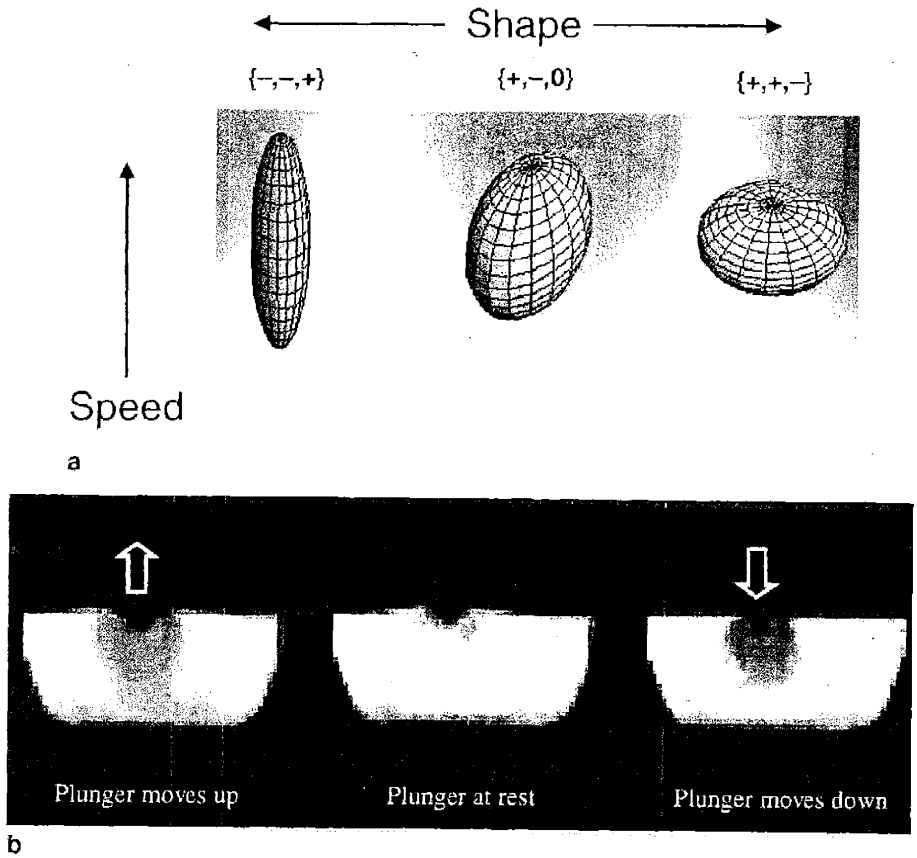

Figure 4.3 HSB color maps of strain rate in gel phantom. **a:** 3D strain color code with a hue-saturation-brightness system. Brightness: mean magnitude of the phase contrast images. Saturation: net strain rate. Hue: geometry of the strain rate, defined by skewness of its set of eigenvalues. Eigenvalues {+,-,-} has skewness > 0 and is coded red. This geometry is typical of myocardial systolic strains. Eigenvalues {+,-,-} has skewness < 0 and is coded blue. This is typical of myocardial strains during filling. Strains with eigenvalue skewness ≈ 0, corresponds to eigenvalues {+,0,-}, is coded green. This is plane strain and is characteristic of normal isovolumic twist. **b:** GRE 3D strain rate MRI of the gel phantom displayed in HSB color. Relaxation mimic systolic ejection (red) while compression mimics diastolic filling (blue). Plane strain (green) are generally absent in nontwisting phantom. (Illustrations are provided by Reese)

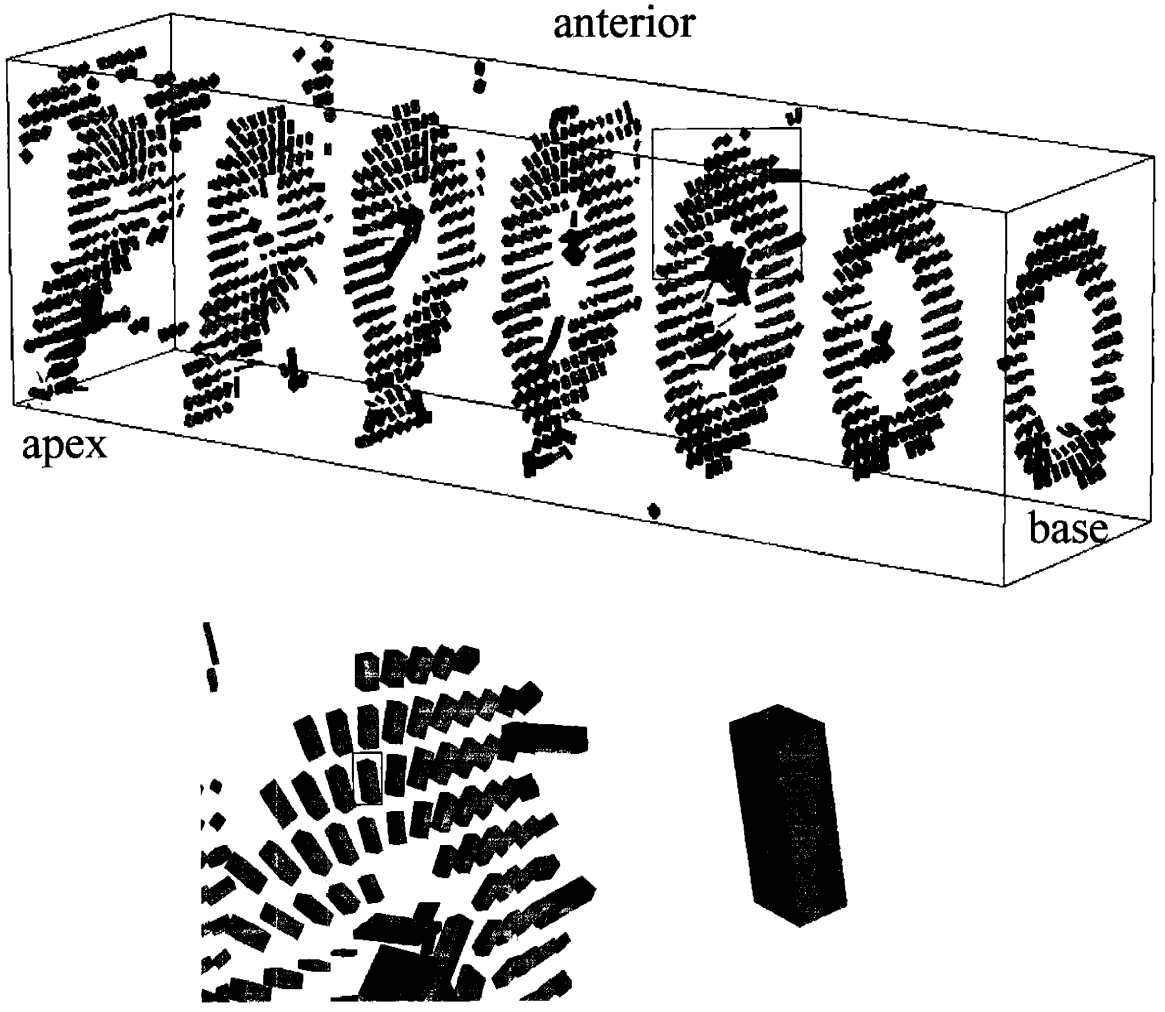

Figure 4.4 Multisclice, multiphase, phase contrast strain rate acquisition shown as icon fields and color maps. **a** and **b**: A perspective view of icons (boxes) allows the multislice data to be shown in relative anatomic location while displaying the strain and strain rate characteristics doe each pixel. The seven slices were acquired at systole, 270 ms after the ECG R-wave. The icon's largest axis is uniformly pointing toward the center of the ventricle, demonstrating the well known radial thickening with circumferential and longitudinal shortening of normal systolic contraction. An enlargement of the red outlined area shows the radial thickening more clearly. (Illustrations are provided by Reese)

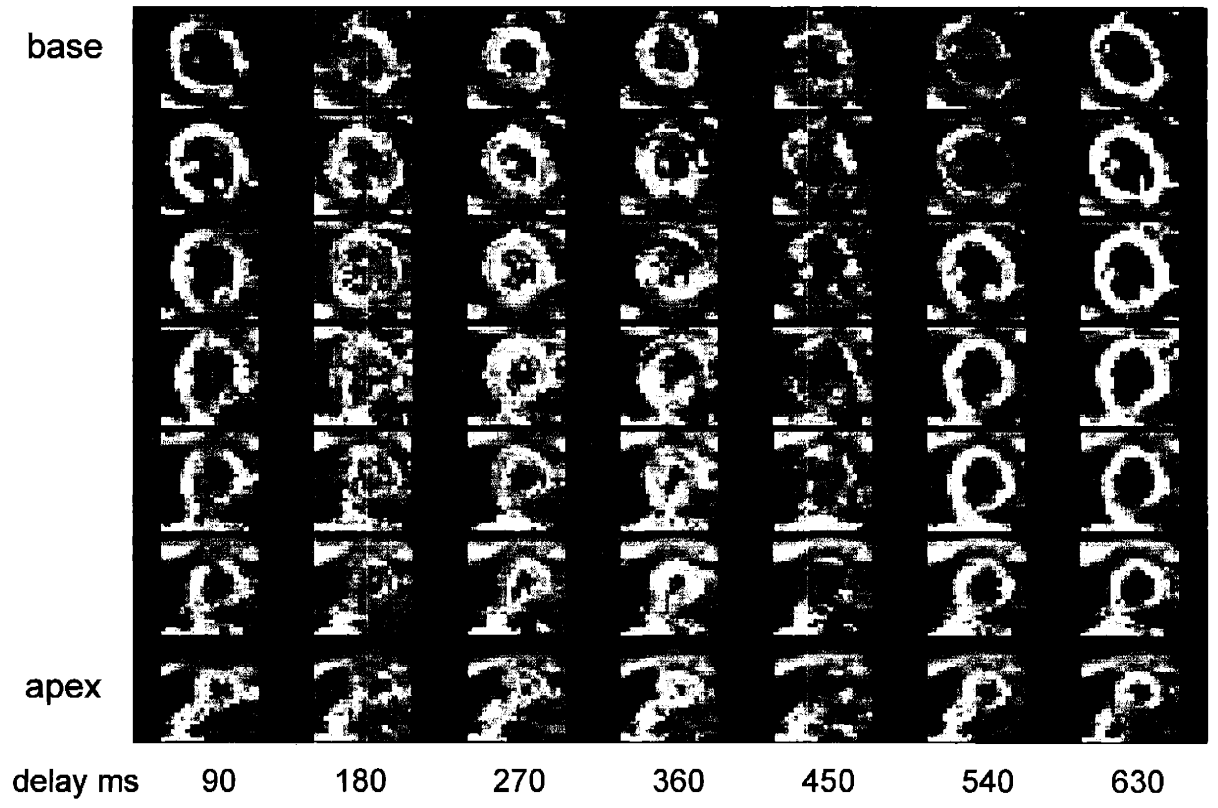

Figure 4.4 c: Strain rate images in HSB color model of seven slices separated by 1 cm, and seven cardiac phases at intervals of 90 ms starting 90 ms after ECG R-wave detection. Indicated by red, systole lingers longest at the cardiac apex. Proceeding to diastole, local deformation reverses (blue and green) and proceeds dysynergically. The regions of the heart do not relax uniformly; this is characteristics of a normal heart and is noted in the echocardiography literature. (Illustrations provided by Reese)

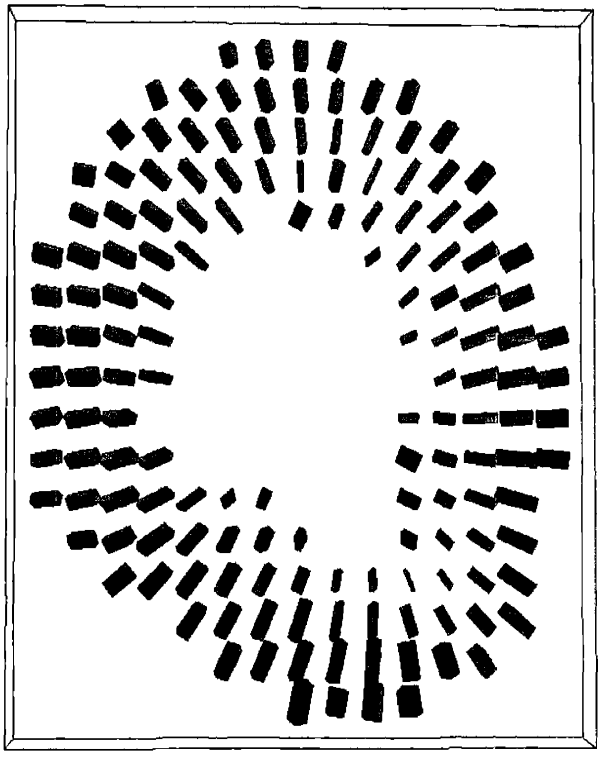

Figure 4.5 STE phase-contrast strain imaging shows net systolic 3D strain in the normal heart. The image is from mid-ventricle in the cardiac short axis. Net systolic strain, measured from 100 to 300 ms post-ECG R-wave (Δ = 250 ms) shows rotation (twist) of myocardium from apex to base. Note the pitch (rotation along the radial axis) of the boxes demonstrating longitudinal-circumferential shear, the local counterpart of myocardial twist. (Illustrations are provided by Reese)

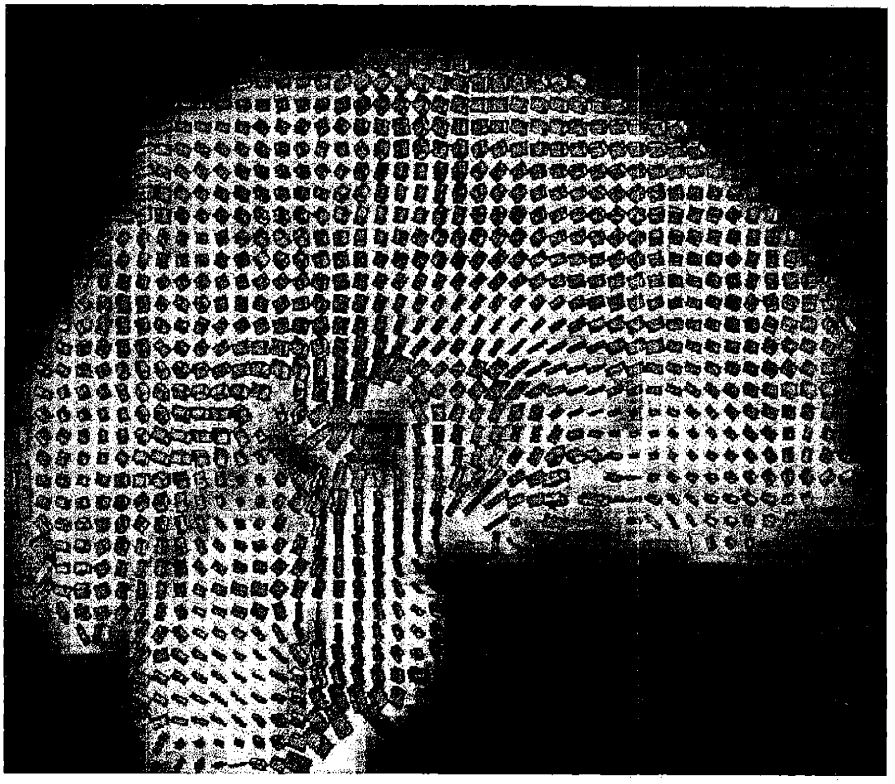

Figure 4.6 3D strain tensor field in normal human brain due to vascular pulsatility, with sensitivity at the diffusion limit. The sagittal section at the midline exhibits normal 3D strain rates of the brain parenchyma due to vascular pulsation. The strain rate tensors are displayed in iconic fields, superimposed on the corresponding magnitude image of the brain. The image was taken with motion sensitivity VENC of 0.23 cm/s, 350 ms after the ECG R-wave, within the normal time interval of the middle cerebral artery (MCA) pulse. Diffusion sensitivity $b \approx 300$ s/mm^2. The 3D strain rate map shows a cranio-caudal elongation of the midbrain and brainstem, which is consistent with the expected extrusion of cranial contents into the posterior fossa and toward the foramen magnum concomitant with the supratentoral volume bolus of the MCA pulse wave. The observed parenchymal strain rates have a dynamic range of ~ 0.1 s^{-1}, corresponding to strains of 0.002 mm per mm of tissue during the experimetntal time baseline Δ, or displacements of 6μ per voxel, with a standard error of $\pm$200 nm. (Illustrations are provided by Reese)

Chapter 5

Complex Structure-Function Relations of Myocardial Laminar Sheets Found in Normal Humans with Diffusion and Strain MRI

5.1 Introduction

Ventricular wall thickening is essential to systolic ejection. Relating myocardial structure to ventricular wall thickening is important to understand myocardial structure-function relations. While cellular rearrangement is thought to play an important role in ventricular wall thickening (29,104), the precise mechanism is not completely understood. Recent studies on myocardium reveal that the myocytes are organized into branching laminar sheets, which are about four cells thick and stacked upon one another from apex to base (20,89,90). Extracellular collagen fibers provide tight coupling within the sheets, but loose coupling between adjacent sheets (19, 20). This kind of sheet structure is thought to provide the basis for cellular rearrangement during ventricular thickening. Invasive studies on canines have suggested that the myocardial sheets contribute to ventricular wall thickening predominantly via cross-fiber deformation terms, sheet shear and sheet extension (30,31). However, previous invasive studies were performed on canine hearts and were limited to particular parts of the ventricular wall (studies were performed on selected sites at anterior free wall, septum, apex and base). Whether this hypothesis applies on humans and also on other ventricular areas needs further investigation.

To test whether this hypothesis works on humans and also on other ventricular areas, we applied noninvasive *in vivo* MRI techniques to normal human hearts. Using cardiac diffusion MRI, we acquired diffusion tensor images of the myocardium, from which we defined the sheet structure. Using phase contrast MRI, we acquired strain rate images of the myocardium. By registering diffusion and strain rate MRI images at mid-left ventricle in mid-systole, we analyzed the contribution of myocardial sheets to ventricular radial thickening, and addressed the function of myocardial sheets on normal humans.

5.2 Methods

The experiments were performed on normal human subjects. Each subject provided written informed consent, which was approved by the hospital human study committee. Registered diffusion tensor images and 3D strain rate images at a mid-left ventricular short-axis slice (slice thickness 6 mm, in-plane resolution 3x3 mm) were taken using a 1.5-T GE Signa MR imager (General Electric Medical Systems, Milwaukee, WI) retrofitted with instascan echo planar imaging. Electrocardiogram (ECG) R-wave triggering was used for data acquisition.

In diffusion studies, the subjects were instructed to use synchronized breathing to suppress respiration motion. Diffusion tensor images were then acquired using a double gated stimulated-echo sequence (57-59,80), in which two unipolar diffusion encoding gradients were applied at identical phases of two consecutive heart beats (Fig. 5.1). TE = 50 ms and TR = 4 R-R interval. The time of imaging was at the optimum point at mid-systole where the diffusion measurement yielded accurate results using this sequence (59, 80, 105). Diffusion-encoding used gradients $\boldsymbol{G}$ directed to non-opposed edge centers of a cube $\{\{1,\pm1,0\}, \{0,1,\pm1\}, \{\pm1,0,1\}\}$ of intensity $|\boldsymbol{G}|$ = 10 mT m^{-1} and duration δ (6-8 ms) adjusted to yield a diffusion sensitivity $b \approx 400$ s mm^{-2}. By acquiring six attenuated diffusion images I_i (i = 1…6) using the six oriented diffusion encoding gradient $\boldsymbol{G}_i$ (i =1…6), and an unattenuated image I_0 using a null gradient, the diffusion tensor $\boldsymbol{D}$ at the time of encoding is then determined by solving the linear equation (59, 106):

$$-\log(I_i/I_0) = (\Delta - \delta/3)\, \boldsymbol{k}_i^T \boldsymbol{D}\, \boldsymbol{k}_i \qquad (5.1)$$

where Δ is the diffusion encoding time, $\boldsymbol{k}_i = 2\pi\gamma\delta_i\boldsymbol{G}_i$ is the spatial modulation vector and γ the proton gyromagnetic ratio. Sixteen averages were taken to ensure high quality data (SNR ~30:1), and the total acquisition time is about 8 minutes for the diffusion study.

The corresponding time and spatial registered strain rate images were acquired using a single-shot spin-echo echo-planar imaging sequence augmented by velocity encoding bipolar gradient pulses, as shown in Fig.1. Velocity-encoding gradient pulses were applied with amplitude $|g|$ = 10 mT m^{-1} and pulse duration δ = 6 ms for a velocity sensitivity |k| = 130 radian m^{-1}, with tetrahedral orientations corresponding to the nonopposed corners of a cube (80,92). TE = 50 ms and TR = 4 R-R interval. Synchronized breathing was used in acquisition as in diffusion studies. Two contiguous 3 mm sections with opposite 1.5 mm offsets from the section center were imaged for the calculation of 3D strain rate tensor $\boldsymbol{S}$:

$$S_{ij} = (1/2)\,(\delta V_i/\delta x_j + \delta V_j/\delta x_i) \qquad (5.2)$$

where V_i and S_{ij} were cartesian components of the velocity field V and strain rate tensor field $\boldsymbol{S}$, i and j were coordinates indices, and δx_i was the differential between pixels adjacent in the x_i direction (79,80). Four averages were used for high quality data (SNR ~ 40:1), and the total imaging time was about 2 minutes for strain rate study.

After registered diffusion images and 3D strain rate images were acquired, image quality was assured by examining both the magnitude and phase images. The diffusion tensors and strain rate tensors were then calculated at each pixel. Myocardial sheet structure was then specified by the three eigenvectors of the diffusion tensor (55,56), with 1st eigenvector corresponds to the fiber vector **f**, 2nd eigenvector corresponds to the sheet vector **s**, and 3rd eigenvector corresponds to the sheet normal vector **n**. The strain rate tensor was then expressed in the local myocardial sheet coordinates {**f**,**s**,**n**} as a symmetric matrix:

$$\mathbf{S} = \begin{bmatrix} S_{ff} & S_{fs} & S_{fn} \\ S_{sf} & S_{ss} & S_{sn} \\ S_{nf} & S_{ns} & S_{nn} \end{bmatrix}$$

where the lower-right 2x2 matrix are cross-fiber strain terms: S_{ss}, sheet extension; S_{sn}, sheet shear; and S_{nn}, sheet-normal thickening. The rest of the components in the matrix are fiber strain terms: S_{ff}, fiber shortening; S_{fs}, fiber-sheet shear; and S_{fn}, fiber-normal shear. To relate sheet structure to ventricular radial thickening, we define **r** as the radial unit vector with origin at the left ventricular centroid, $\mathbf{r} = \{r_f, r_s, r_n\}$, which is expressed in the local sheet coordinates. The myocardial radial thickening R_t at each pixel was then calculated as:

$$R_t = \mathbf{r}^T \mathbf{S}\ \mathbf{r} = (r_f r_f) S_{ff} + (2 r_f r_s) S_{fs} + (2 r_f r_n) S_{fn} + (r_s r_s) S_{ss} + (2 r_s r_n) S_{sn} + (r_n r_n) S_{nn} \quad (5.3)$$

The fractional contribution of each **S** strain component to radial thickening was then calculated as the ratio of each strain item at right hand side to R_t at left hand side. After the ratios were calculated, statistical analysis was performed on an all-pixels basis (left ventricle pixels with papillary muscle excluded). The final results were shown as mean ± confidence interval (CI) of the ratio of each strain component to examine the significance of each component to radial thickening. Regional mean contributions of each major strain component to radial thickening were also examined by summing the results of all subjects on a regional basis.

Figure 5.2 illustrates the registered diffusion tensor field and strain rate tensor field, from which sheet function can be derived using the method described above.

5.3 Results

Figure 5.3 shows the mean contribution (in percentage with 95% confidence interval (CI) indicated) to radial thickening of the six sheet strain components of 7 normal subjects. It can be seen that fiber shortening S_{ff}, fiber-sheet shear S_{fs} and fiber-normal shear S_{fn} contribute little to radial thickening. The major contribution comes from three components: sheet extension S_{ss}, sheet shear S_{sn} and sheet normal thickening S_{nn}. Each of the three components can contribute significantly (as much as 40-60%) to radial thickening. While the mean contribution of sheet extension S_{ss} and sheet normal thickening S_{nn} have much individual variance (indicated by scattered plots), the mean contribution of sheet shear S_{sn} is close (indicated by clustered plots) over all subjects. Figure 5.4 illustrate the meaning of the three major strain components that contribute to ventricular wall thickening.

Figure 5.4 shows the mean contribution of the three major components to radial thickening by region. The results are produced based on regional sum of all subjects in study. Each angle in the horizontal axis represents a specific region of the mid-left ventricle wall, as indicated in the diagram to the left of the plot. It can be seen that contributions of the three components to radial thickening are not uniform over the ventricular wall, they are region-dependent. In particular, sheet shear S_{sn} and sheet extension S_{ss} are most dominant at the anterior free wall, where sheet normal thickening S_{nn} has little contribution. But at other locations, such as near the junction of right ventricle and left ventricle, sheet normal thickening S_{nn} is the most dominant one. It can

also be seen that the curve of sheet shear S_{sn} is the smoothest in the three curves, indicating that it is a preferred component by most myocardium for thickening.

Figure 5.5 shows gray scale images of the fractional contribution of the three major components to radial thickening of the 7 subjects in study. It can be seen that, though all hearts examined are healthy hearts with normal functions, the spatial patterns of wall thickening mechanism are not uniform over all hearts. Subjects 1-3 (group 1) are similar in spatial patterns of all three components, such as large sheet shear at anterior free wall, and large sheet normal thickening near ten o'clock and four o'clock. Subject 4 (group 2) has similar regional pattern in sheet shear and sheet normal thickening as that of group 1, however, it prefers to use sheet extension much more than other hearts. Subjects 5-6 (group 3) show patterns that prefer to use sheet normal thickening more than others, as sheet normal thickening are more broadly distributed in these two hearts. Subject 7 shows patterns that looks like an outlier, it uses sheet extension more than sheet shear at the anterior free wall, and it also does not use sheet normal thickening much as others do.

5.4 Discussion

5.4.1 Comparison with previous studies

Our studies show that the myocardial sheets contribute to radial thickening via three major components: sheet shear, sheet extension and sheet normal thickening. The finding of significant contribution of sheet normal thickening to ventricular thickening has not previously been documented. We also mapped spatial heterogeneity of sheet function over the entire mid-left ventricle and also over subjects, which also has not previously been documented.

In previous hypothesis based on invasive canine studies, sheet shear and sheet extension were found to be the primary determinants of wall thickening strain, and sheet normal thickening is found to contribute little. Fiber strain terms were also found to have little contribution. Previous studies did not find significant sheet normal thickening likely because of the limited areas they examined. In studies of LeGrice and Costa etc, selected sites at anterior free wall, septum, apex and base were examined. At anterior free wall, they found that the contribution to radial thickening came mostly from sheet extension (64%) and sheet shear (31%), with little contribution from sheet normal thickening (1%). At septum, they found that sheet shear (45%)

and sheet extension (39%) were dominant components, but sheet normal thickening also had some contribution (13%). At apex & base, they found that sheet extension (60%) and sheet shear (40%) dominated the contribution, and sheet normal thickening had small but negative contribution (-5%). At these ventricular sites, their results did not show significant contribution from sheet normal thickening.

Unlike LeGrice and Costa's studies, our study is performed on humans at a slice at mid-left ventricle. Though of different species, we found several points in common between both studies. First, the fiber strain terms are found to be small and have little contribution to wall thickening in both studies. Second, there is similarity in results at the anterior free wall. Same as in studies on canines, we also find that sheet shear (~50%) and sheet extension (~30%) dominate the contribution, and sheet normal thickening contributes little (~10%). But in our results, contribution from sheet shear is more significant than that of sheet extension. The third similarity is at septum. We found large contribution from sheet shear (~30%) and sheet extension (~20%), and we also observed significant contribution from sheet normal thickening (~40%, much larger than the 13% observed on canines). For rest of the mid-left ventricle, which has not been examined in previous studies, we found that sheet normal thickening is the most significant component to ventricular thickening, especially near the junction of right ventricle and left ventricle. The second contributor in these locations is sheet shear, and the third is sheet extension. This result is somewhat unexpected, as previous thoughts were focused on sheet shear and sheet extension. The findings here suggest that sheet normal thickening is an equally important mechanism for systolic wall thickening.

Another interesting result in our studies is the behavior of sheet shear. We found that the mean fractional contribution of sheet shear to wall thickening is large and have little fluctuation over the entire mid-left ventricle, as can be seen in Fig. 5.4. This kind of phenomena strongly suggests that sheet shear is a preferred thickening mechanism used by the human myocardium, at least those at mid-left ventricle. More interestingly, while we found that there are apparent intersubject variances on the mean contribution from sheet extension and sheet normal thickening to radial thickening, the intersubject variance of mean contribution from sheet shear is quite small, as can be seen in Fig 5.3 by the clustered plots. This again suggests that sheet shear is a preferred mechanism for ventricular wall thickening in humans.

Our results also show clear evidence that ventricular wall-thickening mechanism has regional heterogeneity. Previous studies on myocardial sheets show that there are regional variations in myocardial sheet orientations, which could suggest that the wall-thickening mechanism may also have regional differences. However, there is no clear experimental evidence. Although LeGrice and Costa's results on canines have suggested that there may be regional difference in wall-thickening mechanism as the fractional contributions of sheet strains to wall thickening between the anterior free wall and the septum seems have some differences, further experimental evidences are required. Our studies on the entire mid-left ventricle wall clearly map the regional heterogeneity of the wall thickening mechanism, as shown in Fig 5.4, where we found that the wall-thickening mechanism at anterior free wall is quite different from that of other regions. This heterogeneity on sheet function is in contrast to the results on fiber function and wall thickening, which appear to be uniform or symmetric. The existence of such heterogeneity suggests that myocardial sheet function is complex, and future studies on myocardial structure-function relations should incorporate such heterogeneous properties of the myocardium.

We also observed interesting variations in spatial patterns of wall thickening mechanism among normal subjects, as can be seen in Figure 5.5. All subjects are healthy with normal heart functions, confirmed in our experimental data by normal ECG, uniform fiber shortening pattern and large symmetric radial strains (80). In addition, we performed repeated scan on subject 2 and 4, with reproducible results. Thus, the variations observed in our studies are unlikely to be caused by experiment artifacts. More reasonably, it does show that there may be more than one spatial pattern of sheet function in normal humans. If this holds true, then interesting questions arise: what kind of spatial pattern of sheet function in human hearts can be defined normal or abnormal? Are there any clear distinguish-criteria for sheet function between normal and diseased hearts? To answer these questions, further investigations on large numbers of healthy and diseased subjects are needed.

5.4.2 The structural basis for the observed wall-thickening mechanism

Our results show that there are three mechanism for myocardial wall thickening: sheet shear, sheet extension and sheet normal thickening, all of which are sheet strain terms; fiber strains are found to be small and has little contribution to wall thickening. This kind of wall

thickening mechanism can possibly be explained by the structural characteristics of the myocardial sheets.

As previously described, myocardial sheets are about four cells thick, with extracellular collagen fibers provide tight coupling within the sheets, but loose coupling between adjacent sheets. The tight coupling of collagen fibers within the sheets provide mechanical restriction to the myocytes, which helps to explain why the fiber shear term S_{fs} (shear within the sheet plane) is small and has little contribution to ventricular thickening. The loose coupling of collagen fibers between sheets helps to explain why sheet shear and sheet normal thickening can be so significant. Loose coupling leads to less mechanical restriction to the sheets, and so provides the possibility for sheets to slide relative to one another (accounts for sheet shear) or increase the gap between adjacent sheets (accounts for sheet normal thickening).

One interesting point of sheet shear is that, in both canine and human studies, sheets were observed to prefer sliding relative to one another along the sheet direction rather than along the fiber direction. This was reflected by the large sheet-normal shear (S_{sn}) and small fiber-normal shear (S_{fn}) observed in both studies. The exact mechanism of such behavior is not clear. One possible explanation could be the three-dimensional packing effect of sheets which favor sheets sliding in the sheet direction but prevent sheets from sliding along the fiber direction. To find the exact mechanism, further studies are required.

In contrast to sheet shear, which is well studied and recognized, the substantial sheet normal thickening observed in our experiment at mid-left ventricle in regions other than the anterior free wall has not previously been documented. Sheet normal thickening provides another important mechanism of wall-thickening. The large sheet normal thickening is most likely caused by the increase of gaps between sheets during wall-thickening. Increase of gaps between cell layers within the sheets is less likely as these layers are more tightly coupled by the endomysial collagen networks. The exact mechanism of sheet normal thickening during ventricular wall thickening needs further investigation. Nonetheless, our observation of large sheet normal thickening strongly suggests the above hypothesis. It is also notable that sheet normal thickening appears to be largest near the junctions of left ventricle and right ventricle; this suggests that the sheet structures at these two regions may be somewhat different than that at other regions. Calculation of sheet orientations on our data show that at regions near the junctions of right and left ventricle, the sheets are more longitudinally oriented, while at other

regions (free wall and septum), sheets are more radially oriented. These may help to explain why sheet normal thickening is the most dominant component for wall-thickening near the junctions, but not at other regions such as free wall and septum, where sheet shear and sheet extension dominate the contribution.

One seeming puzzle in the structure-mechanism relations is the substantial sheet extension observed in both canine and human hearts. Sheet extension may result from the sum of increased diameter of the myocytes due to fiber shortening and possible mechanical "stretch-apart" of the myocytes along the sheet direction. Since the myocytes within the sheets are relatively tightly-coupled by the collagen fibers, it is not clear that such "stretch-apart" between myocytes is allowed. However, the substantial sheet extension observed on both canine and human hearts strongly suggest that such movement of myocytes within the sheets is likely to happen (same as what Costa speculated). Increase of cell diameter due to fiber shortening is found to contribute maximally about 20% to local wall-thickening (30), which can not account for the large fractional contribution (up to 40-60%) of sheet extension observed on canine and human hearts. In fact, the observed sheet extension is qualitatively consistent with published increases in transmural cell number and center-to-center distance with increasing ventricular wall thickness (29, 104). To completely understand the exact mechanism of sheet extension, further studies at cellular level may be required.

5.4.3 Advantages of MRI technique

The study in this paper shows that MRI has great advantages in studying myocardial sheet function. Previous invasive studies on sheet function are radiopaque marker based, which requires implanting metallic beads in the myocardium and recording radiographic movies during heart beat to determine the 3-D deformation of the myocardium, then followed by careful histology and optical imaging method to define the corresponding sheet structures. It is obvious that such experiments are invasive, labor-intensive and also difficult to perform. Thus, only limited areas of the ventricle can be examined once at a time using this method. For studies that require large number of samples, such as investigating spatial and inter-subject heterogeneity of the myocardial sheet function, extraordinary difficulties will be encountered if this method is used. Compared with previous invasive method, MRI has clear advantages. First, it is noninvasive, which makes it capable of performing *in vivo* studies on humans that is not possible

for previously invasive methods. Second, it is powerful and convenient, as it is capable of examining any regions of the heart, with easy ways (diffusion and strain rate MRI techniques) to define sheet structure and myocardial 3-D deformation. Third, the following up data analysis after image acquisition are much easier and straightforward compared with previous invasive methods. Thus, MRI is a promising and unique tool to study myocardial structure-function relations. With the improvement of experimental protocols such as increase of imaging resolution, imaging speed etc., it is possible to perform more delicate and detailed studies on sheet functions in the future.

5.4 Conclusions

We studied myocardial sheet function using cardiac diffusion and strain rate MRI, and found that myocardial sheets contribute to ventricular wall thickening via three major components: sheet shear, sheet extension and sheet normal thickening. Fiber shortening and fiber shears contribute little. We also found spatial heterogeneity of each major component. In particular, the myocardial cellular rearrangement at the anterior free wall is quite different than that at other regions. On average, sheet shear and sheet extension dominate the contribution at anterior free wall, where sheet normal thickening contributes little; while at other locations, such as near the junctions of right and left ventricle, sheet normal thickening is the most significant one. We also found subject variability in spatial patterns of wall thickening mechanism, which indicates that there may be more than one spatial pattern of sheet function in normal humans. The heterogeneity observed on sheet function is in contrast to results on fiber function and wall thickening, which appear to be uniform or symmetric. These results indicate that the function of myocardial sheets is complex, and future studies on myocardial structure-function relations should incorporate such heterogeneous properties of the myocardium. It also shows that MRI is a promising tool for noninvasive cardiac study on humans, and also a unique tool for studies that require large samples.

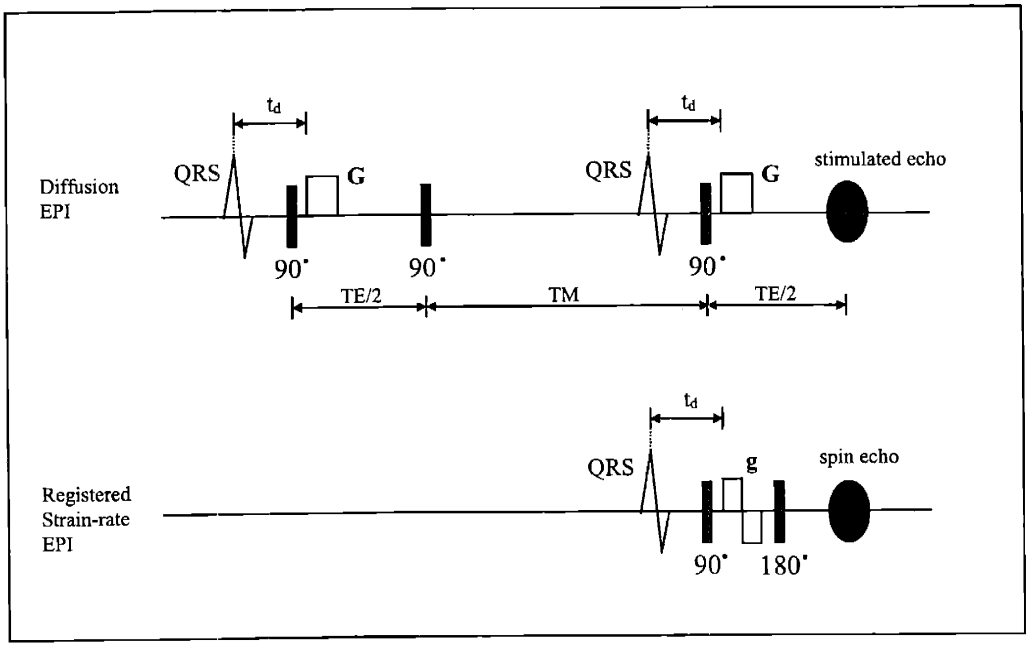

Figure 5.1 Pulse sequence for acquisition of registered diffusion MR images (top) and strain-rate MR images. The diffusion images are acquired using a stimulated echo pulse sequence that incorporates two bipolar gradient pulses *G* separated by one cardiac cycle for the diffusion-encoding. Three 90° rf pulses are separated by the echo time *TE* and the mixing time *TM*. Unipolar diffusion-encoding gradients *G* follow the 1st and 3rd rf pulses. ECG R-wave triggers locate the diffusion-encoding gradient pulses *G* at identical phase delay t_d in consecutive cardiac cycles. The registered strain rate images are obtained using a velocity-sensitive phase-contrast spin echo. The velocity-encoding bipolar gradients *g* are applied at equal delay t_d from R-wave as in the diffusion study for spatial and temporal registration with diffusion images. The readout echo centers are also equal in both sequences. EPI = echo-planar imaging.

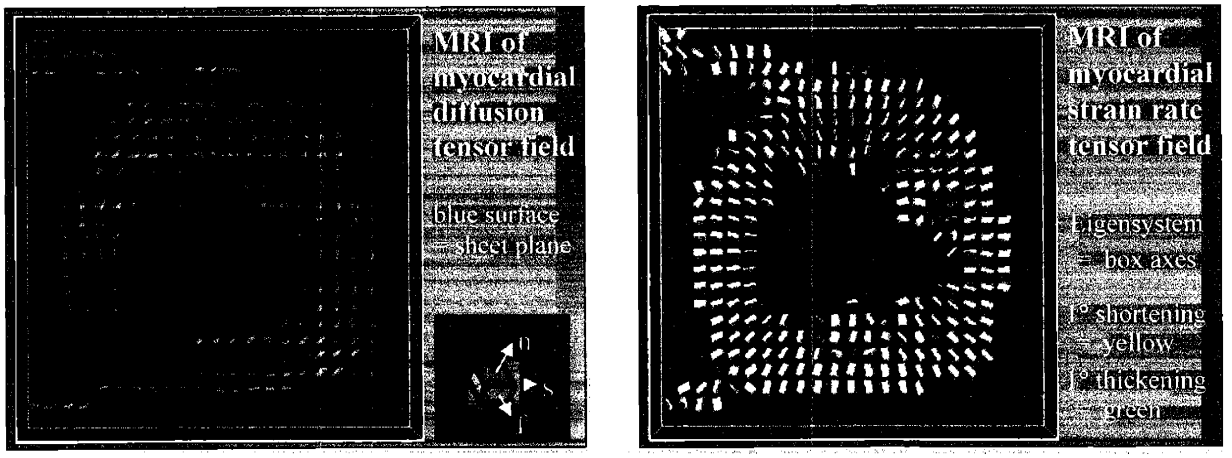

Figure 5.2 Registered diffusion tensor field and strain rate tensor field yield sheet function. Left: myocardial diffusion tensor fields (corresponds to myocardial sheet structure) represented by colored boxes, with fiber vector ***f*** (1st eigenvector), sheet vector ***s*** (2nd eigenvector), sheet normal vector ***n*** (3rd eigenvector) perpendicular respectively to red, green and blue-colored surfaces. Right: myocardial strain rate tensor field represented by colored boxes. The box has lengths proportional to the stretch in each direction and axes parallel to the directions of principle strains. Axes perpendicular to green, yellow and pink surfaces correspond to directions of maximum thickening, maximum shortening and minimum shortening, respectively.

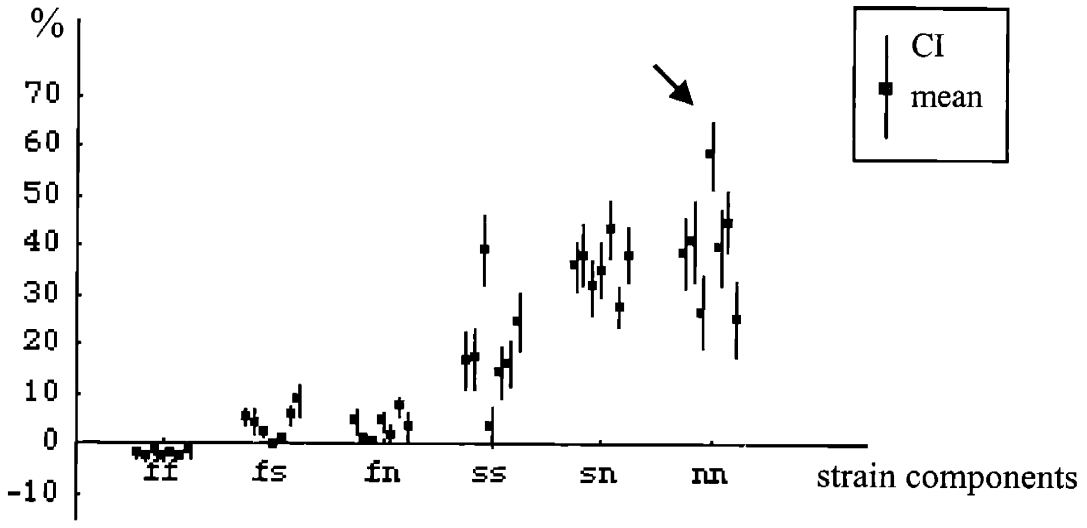

Figure 5.3 Mean fractional contribution (with 95% Confidence Interval (CI) indicated) of sheet strain to radial thickening at mid-left ventricle of 7 normal human subjects. ff: fiber shortening; fs: fiber-sheet shear; fn: fiber-normal shear; ss: sheet extension; sn: sheet shear; nn: sheet normal thickening. The arrow indicates large sheet normal thickening that has not previously been documented. It can be seen that fiber shortening, fiber shear and fiber normal shear contribute little to radial thickening. The major contribution comes from three components: sheet extension, sheet shear, and also the sheet normal thickening. It is also noted that contribution of sheet extension and sheet normal thickening have much individual variance (indicated by scattered plots), but the contribution of sheet shear is similar (indicated by clustered plots) over all subjects.

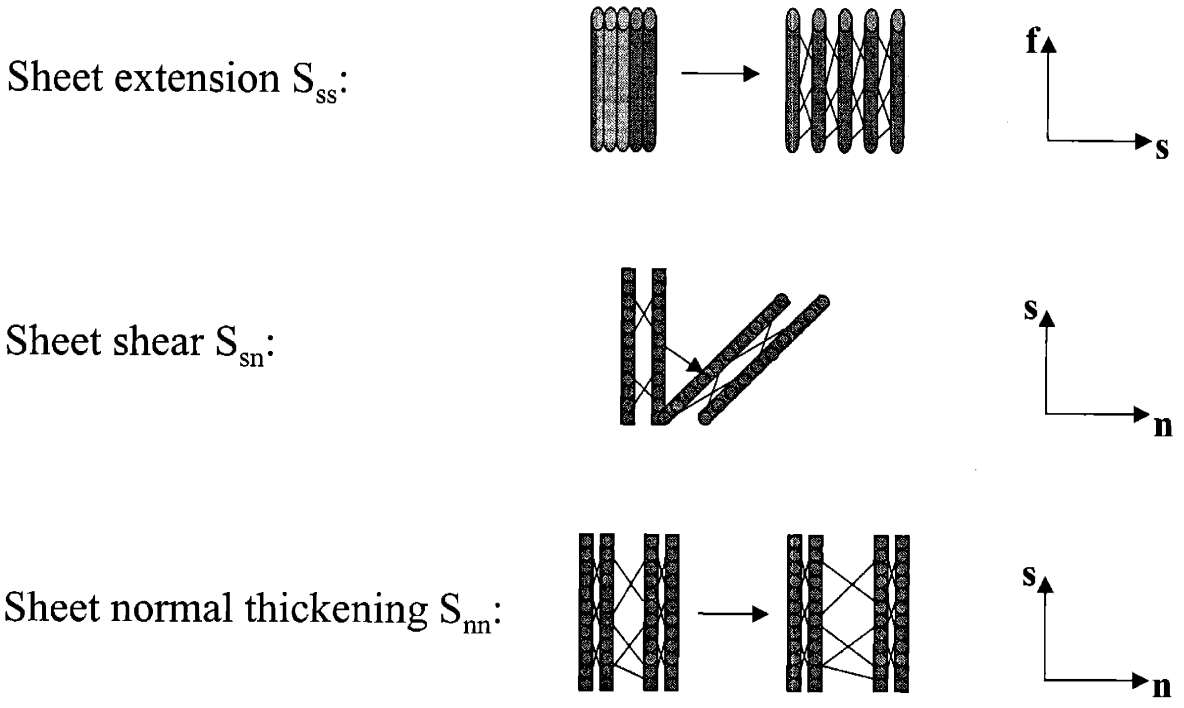

Figure 5.4 Diagram of the three major sheet strain components that contribute to ventricular wall thickening. Cylinder represents myocyte within the sheet. Lines between myocytes or sheets represent collagen fibers. $\mathbf{f}$: fiber vector; $\mathbf{s}$: sheet vector; $\mathbf{n}$: sheet normal vector.

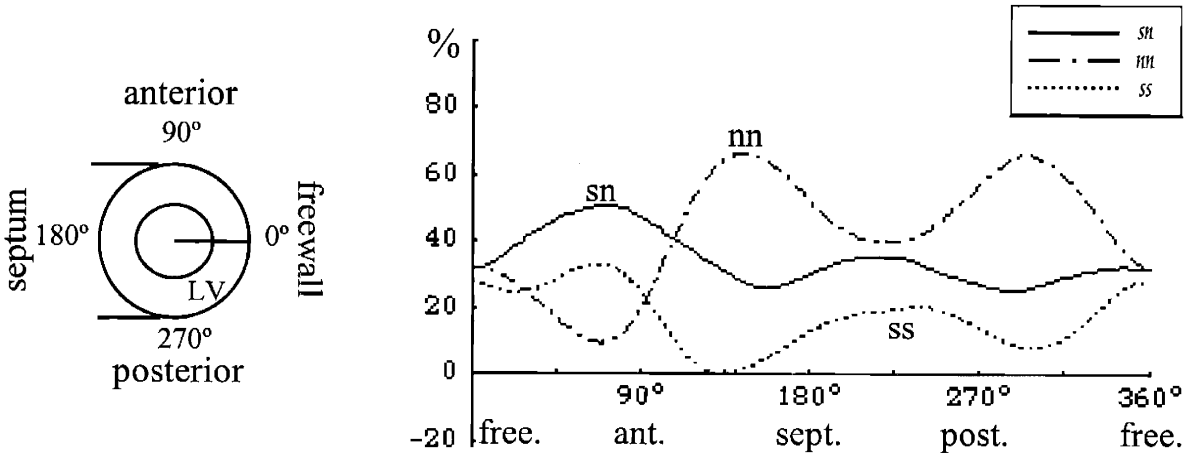

Figure 5.5 Mean contribution of the three major components to radial thickening by region. The results are produced based on regional sum of all subjects in study. Each angle in the horizontal axis represents a specific region of the mid-left ventricle wall, as indicated in the diagram to the left of the plot. ss: sheet extension. sn: sheet shear. nn: sheet normal thickening. It can be seen that contributions of the three components to radial thickening are not uniform over the ventricular wall, they are region-dependent. In particular, sheet shear and sheet extension are most dominant at the anterior free wall, where sheet normal thickening has little contribution. But at other locations, sheet normal thickening is the most dominant one. It can also be seen that the curve of sheet shear is the smoothest in the three curves, indicating that it is a preferred component by most myocardium for thickening.

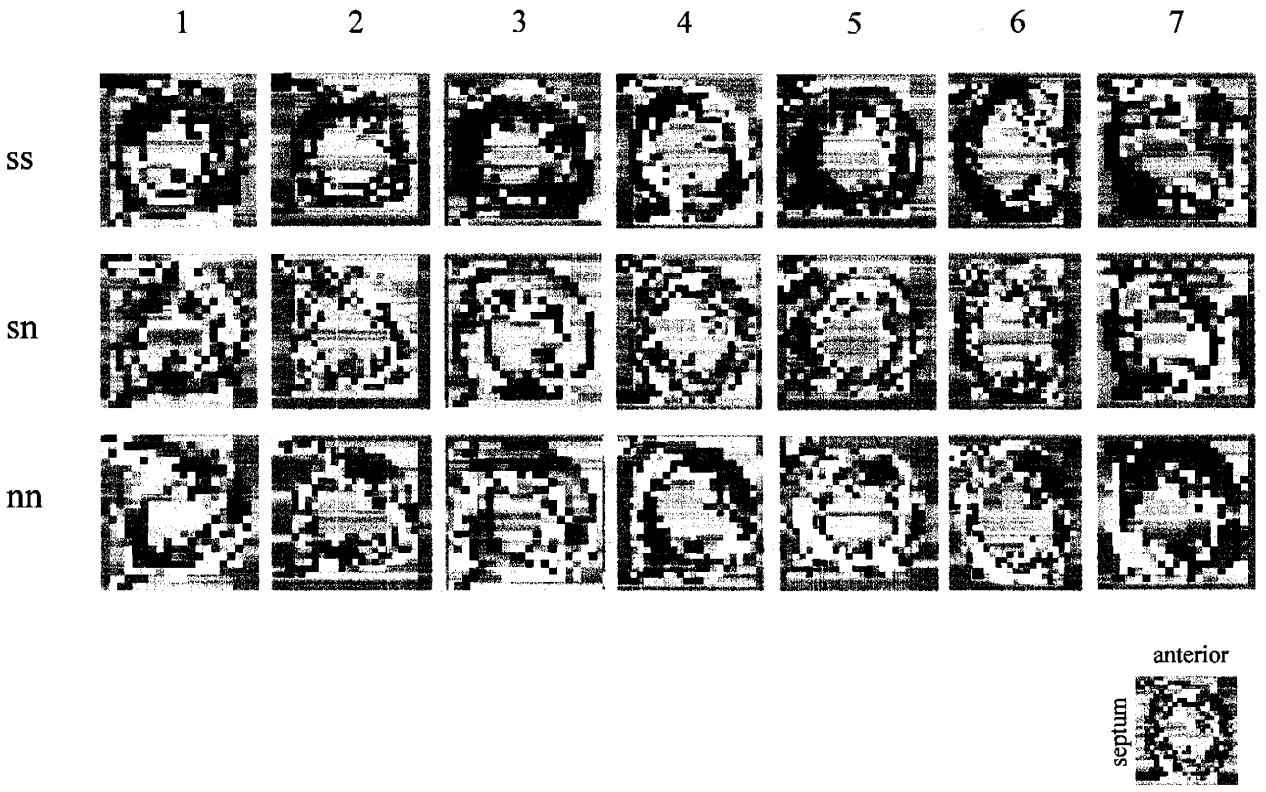

Figure 5.6 Gray scale maps of the contribution of the three major sheet strain components to radial thickening of the 7 normal subjects. **ss**: sheet extension; **sn**: sheet shear; **nn**: sheet normal thickening. Gray color = small percentage, white color = large percentage. It can be seen that the regional patterns of wall thickening mechanism are not uniform over all hearts. Subjects 1-3 (group 1) are similar in regional patterns of all three components, such as large sheet shear at anterior free wall, and large sheet normal thickening near ten o'clock and 4 o'clock. Subject 4 (group 2) has similar regional pattern in sheet shear and sheet normal thickening as in group 1, however, it prefers to use sheet extension much more than other hearts. Subjects 5-6 (group 3) show patterns that prefer to use sheet normal thickening more than other hearts, as sheet normal thickening are more broadly distributed in these two hearts. Subject 7 (group 4) show quite different patterns, it prefers to use sheet extension more than sheet shear at the anterior free wall, and also does not use sheet normal thickening much.

Chapter 6

Conclusions

6.1 Summary

The myocardial structure-function relation is the key to understand the functional design of the ventricular myocardium. While the function of myocardial fibers has been extensively studied, the recently observed laminar organization (sheets) of myocardial fibers is not well understood. To understand the functional role of myocardial sheets, methods that can register myocardial architecture and myocardial strain under identical *in vivo* conditions must be developed. Existing methods measure myocardial structure and strain under different physiological conditions. In these methods, myocardial strain is measured *in vivo* using invasive plantation of radio-opaque markers, while sheet structure is defined using postmortem dissection, which is suffered from tissue distortion and is also lab-intensive. Thus, existing methods have much limitations. This thesis establishes noninvasive MRI methods, registered cardiac diffusion and strain MRI, to acquire information about myocardial sheet structure and myocardial strain under identical *in vivo* conditions, and thus defines the functional role of myocardial sheets. This methodology solves limitations of existing methods that require postmortem dissection, and can be applied to living humans at multiple time horizons in the cardiac cycle.

Chapter 2 establishes *in vivo* myocardial diffusion MRI techniques. We addressed the critical problem of motion sensitivity on *in vivo* cardiac diffusion measurement, and validated the reliability of current techniques on myocardial diffusion imaging. A new motion-insensitive diffusion imaging pulse sequence (the bipolar method) is introduced to address this problem. Experiments are designed both *ex vivo* and *in vivo* to prove the validity of the new method and

also previously established method (the unipolar sweet spot method). In *ex vivo* validation, We compared the unipolar and the bipolar methods in a phantom with cyclic strain, and demonstrated the motion- and strain-independence of the bipolar method. In *in vivo* validation, we measured myocardial diffusion eigenvalues at different phases in systole on a normal human subject using the bipolar method, and proved that the bipolar method is insensitive to myocardial motion effect. We also compared the bipolar method and the unipolar method at the sweet spot, provided cross validation for both methods. In conclusion, the new bipolar method is accurate and insensitive to cardiac motion and strain. Previous unipolar sweet spot method is also accurate. Both methods are valid for *in vivo* studies.

With established *in vivo* diffusion MRI methods. In chapter 3, we applied diffusion MRI to observe myocardial sheet and fiber structure during systole, tried to obtain a picture of how the myocardial sheets function. We used motion insensitive bipolar method to imaging myocardial diffusion tensor at multiple cardiac phases to observe certain motion patterns of sheets and fibers. Sheet angle and fiber helix angle were calculated as parameters for observation. The histogram movie of sheet angle and fiber angle show that sheets become more radially oriented during contraction and fibers become more longitudinally oriented, which are in agreement with previous invasive studies on canine hearts. These results show evidence that sheet architecture undergoes remarkable changes during contraction, and suggest that sheet shear is an important mechanism for ventricular wall thickening.

To understand the role of myocardial sheets, diffusion MRI alone is not sufficient, mechanical information of the myocardium deformation (myocardial strain/strain rate) must be measured and registered with diffusion images to obtain a detailed insight into the functional role of myocardial sheets. Thus, in Chapter 4, we introduced a new myocardial 3D strain/strain rate imaging techniques using velocity encoding phase contrast methods.

The previous method quantifies myocardial 3D strain rate by collecting adjacent slices at different heart beats. This method, though effective, has problem of through-plane noise. To resolve this problem, we developed a new method that is capable of imaging myocardial 3D strain rate by collecting the two adjacent slices simultaneously within the same heart beat. Compared to previous phase contrast methods, the new method fully realizes potential sensitivity of phase contrast EPI, significantly improves image quality regarding noise and artifact, requires much shorter acquisition time with only routine patient supervision, and can be quickly and

automatically processed without operator supervision. Following validation using a strain phantom, we demonstrated our 3D single-shot strain method in healthy *in vivo* human heart and brain.

Using established diffusion and strain MRI techniques, in chapter 5, we explored the functional role of myocardial sheets by registering MRI diffusion image with MRI 3D strain rate image. We tested the hypothesis that myocardial laminar sheets contribute to ventricular thickening predominantly via sheet shear and sheet extension, as previously found invasively in canine studies at particular ventricular sites. In normal human subjects, registered images of myocardial sheet architecture and strain at mid-systole were acquired with diffusion and strain MRI. Sheet function was analyzed by computing myocardial strain in the local fiber-sheet coordinates. It is found that, in general, myocardial sheets contribute to ventricular thickening through all three cross-fiber strain components: sheet shear, sheet extension, and by previously undocumented sheet-normal thickening. Each of these components demonstrated substantial spatial heterogeneity, with sheet shear and sheet extension usually predominant in the anterior free wall and sheet-normal thickening predominant near the right ventricular insertions; however, considerable inter-subject variability was also found. In all cases, the contributions to thickening of fiber strains were small. Sheet function in normal humans is found to be heterogeneous and variable, contrasting with the previously demonstrated uniformity of fiber shortening. These results indicate that the function of myocardial sheets is complex, and future studies on myocardial structure-function relations should investigate the causes and extent of such heterogeneous properties of the myocardium. It also shows that MRI is a valid and effective tool for noninvasive study of myocardial mechanical function in humans

6.2 Conclusion

In this thesis, we established noninvasive MRI methods to quantify *in vivo* myocardial diffusion and myocardial 3D strain. We presented a new method for diffusion MRI in the beating heart that is insensitive to cardiac motion and strain. The new method addresses the problem of motion sensitivity of diffusion MRI in the beating heart that was not well addressed by a previous methodology valid in normal human hearts. We also presented new 3D phase contrast strain imaging using single-shot 3D EPI. Compared to previous phase contrast 3D strain

methods, the new method realizes potential sensitivity of phase contrast EPI, significantly improves image quality regarding noise and artifact, requires much shorter acquisition time, and can be quickly and automatically processed without operator supervision. Using these noninvasive methods, we acquired registered diffusion and strain MRI to provide quantitative maps of myocardial structure-function relations in living humans. From these quantitative maps, we are able to define for the first time accurate images of the functional role of myocardial sheets. We found that myocardial sheets contribute to ventricular thickening through all three cross-fiber strain components: sheet shear, sheet extension, and by previously undocumented sheet-normal thickening. Each of these mechanisms demonstrated remarkable spatial non-uniformity as well as inter-subject variability, this is in marked contrast to the previously demonstrated uniformity of fiber shortening. Owing to this unanticipated complexity, we find that future studies on myocardial structure-function relations must investigate the causes and extent of such heterogeneous properties of the myocardium, which could be well addressed with noninvasive imaging. This thesis shows that MRI is a valid and effective tool for noninvasive study of myocardial mechanical function in humans.

6.3 Future work

The study in this thesis found that myocardial sheet strains are major contributors to ventricular wall thickening, and also suggested that myocardial extracellular matrix (ECM) is an important factor that affects sheet function. Recent studies show that the myocardial ECM can have dynamic changes under pathological conditions (107-111). Thus, one important future work is to study the role of sheet function in diseased hearts. Diseased hearts are expected to have reduced sheet function because wall thickening is often reduced and ECM often become stiffer or disordered in these hearts. Reduced sheet function in diseased hearts may have two different kinds of roles. In dilated hearts without fibrosis, reduced sheet function may be resulted from the geometry change of the ventricle which could cause sheets to be flattened. Reduced sheet function in this case may help to reduce ventricular wall tension which will prevent/reduce the adverse remodeling process of the heart that could lead to heart failure. Thus, in these hearts, reduced sheet function may be an adaptive process that could prevent further deterioration of heart function. However, in hearts that have regional fibrosis, reduced sheet function will be

resulted from the disorder of ECM. The reduction of sheet function in this case will interfere with normal pumping function of the heart and cause the heart function to become more deteriorated. Thus, in these hearts, reduced sheet function will play a negative role which facilitates the adverse remodeling process of the heart. The above hypothesis can be tested by group study using the MRI techniques established in this thesis, and will be carried out in future studies. Another point of interest is the complex structure-function relation of myocardial sheets observed in our study. The heterogeneity and variability of sheet function is in contrast to the previously demonstrated uniformity of fiber shortening, and induces many intriguing questions. What is the global picture of myocardial sheets? How does these sheets affect the mechanical property of the myocardium? How is the global integration of the heterogeneous and variable function of sheets that finally leads to a healthy heart that pumping blood with eurhythmy? What are normal patterns of sheet function? What are abnormal patterns of sheet function? What is the standard for clinical diagnosis using sheet function? These puzzles remain to be solved in future works.

Bibliography

1. Stensen N. De musculis et glandulis observationum specimen, cum epistolis duabus anatomicis. Amsterdam: P le Grand, 1664
2. Lower R. Tractus de Corde. 1932 ed. London: Oxford University Press, 1669.
3. Senac JBD. Traite de la Structure du Coeur, de son Action, et de ses Maladies. Paris: J Vincemt, 1749.
4. Ludwig C. Ueber den Bau und die Bewegungen der Herzventrikel. Zeitschrift fur rationelle Medicin 1849; 7:189-220.
5. Pettigrew JB. On the arrangement of the muscular fibres in the ventricles of the vertebrate heart, with physiological remarks. Philosophical Transactions 1864; 154:445-500.
6. Krehl L. Kenntniss der Fullung und Entleerung des Herzens. Abhandl. Math. Phys. Kl. Koniglichen Saechs. Ges. Wiss. 1891; 29:341-362.
7. MacCallum JB. On the muscular architecture and growth of the ventricles of the heart. Johns Hopkins Hospital Reports 1900; 9:307-335.
8. Mall FP. On the muscular architecture of the ventricles of the human heart. Am J Anat 1911; 11:211-266.
9. Lev M, Simkins CS. Architecture of the human ventricular myocardium, technique for study using a modification of the Mall-MacCallum method. Laboratory Investigation 1956; 5:396-409.
10. Grant RP. Notes on the muscular architecture of the left ventricle. Circulation 1965; 32:301-308.
11. Torrent-Guasp F. The cardiac muscle. Madrid: Fundacion Juan March, 1973.
12. Hort W. Untersuchungen uber die Muskelfaserdehnung wand des Meerschweinchens. Virchow Arch. Pathol. Anat. Physiol. Klin. Med. 1957; 329:694-731.
13. Streeter DD, JR.,, Bassett DL. An engineering analysis of myocardial fiber orientation in pig's left ventricle in systole. Anat. Rec. 1966; 155:503-511.
14. Streeter DD, Spotnitz HM, Patel DP, Ross J, Sonnenblick EH. Fiber orientation in the canine left ventricle during systole and diastole. Circulation Research 1969; 24:339-347.

15. Streeter DD, Vaishnav RN, Patel DJ, Spotnitz HM, Ross J, Sonnenblick EH. Stress distribution in the canine left ventricle during diastole and systole. Biophysical Journal 1970; 19:345-363.
16. Streeter DD. Gross morphology and fiber geometry of the heart. In: Berne RM, ed. Handbook of Physiology. Bethesda, MD: American Physiological Society, 1979; 61-112.
17. Streeter DD, Ramon C. Muscle pathway geometry in the heart wall. Journal of Biomechanical Engineering 1983; 105:367-373.
18. Hort W. Makroskopische und mikrometrische untersuchungen am myokard verscheiden stark gefulter linker kammern. Virchows Arch. Path. Anat. Physiol. Klin. Med. 1960; 333:523-564.
19. Caufield JB, Borg TK. The collagen network of the heart. Laboratory Investigation 1979; 40:364-372.
20. LeGrice IJ, Smaill BH, Chai LZ, Edgar SG, Gavin JB, Hunter PJ. Laminar structure of the heart I: Ventricular myocyte arrangement and connective tissue architecture in the dog. American Journal of Physiology 1995; 269:H571-H582.
21. Waldman LK, Nosan D, Villarreal F, Covell JK. Relation between transmural deformation and local fiber direction in canine left ventricle. Circulation Research 1988; 63:550-562.
22. Rademakers FE, Rogers WJ, Guier WH, Hutchins GM, Siu CO, Weisfeldt ML, Weiss JL, Shapiro EP. Relation of regional cross-fiber shortening to wall thickening in the intact heart: three-dimensional strain analysis by NMR tagging. Circulation 1994; 89:1174-1182.
23. Arts T, Reneman RS, Veenstra PC. A model of the mechanics of the left ventricle. Annals of Biomedical Engineering 1979; 7:299-318.
24. Arts T, Prinzen FW, Snoeckx LHEH, Rijcken JM, Reneman RS. Adaptation of cardiac structure by mechanical feedback in the environment of the cell: a model study. Biophysical Journal 1994; 66:953-961.
25. Feigl EO. Coronary physiology. Physiological Review 1983; 63:1-206.
26. Prinzen FW. Gradients in fiber shortening and metabolism across the ischemic left ventricular wall. American Journal of Physiology 1986; 250:H255-264.
27. Bloomgarden DC, Young AA, Kraitchman DL, Fayad ZA, Blom AS, Ferrari VA, Axel L. Noninvasive assessment of regional myocardial fiber and cross-fiber strain using finite element modeling and magnetic resonance taggin. . International Society for Magnetic

Resonance in Medicine, 5th scientific meeting and exhibition. Vancouver, B.C., Canada, 1997; 385.

28. Sonnenblick EH, Ross JJ, Covell JW, Spotnitz HM, Spiro D. The ultrastructure of the heart in systole and diastole. Circulation Research 1967; 21:423-431.
29. Spotnitz HM, Spotnitz WD, Cottrell TS, Spiro D, Sonnenblick EH. Cellular basis of volume related wall thickness changes in the rat left ventricle. J Molec Cell Cardiol 1973; 6:317-331.
30. LeGrice IJ, Takayama Y, Covell JW. Transverse shear along myocardial cleavage planes provides a mechanism for normal systolic wall thickening. Circulation Research 1995; 77:182-193.
31. Costa KD, Takayama Y, McCulloch AD, and Cowell JW. Laminar fiber architecture and three-dimensional systolic mechanics in canine ventricular myocardium. Am J Physiol 1999;276 (Heart Circ, Physiol 45):H595-H607.
32. A. Einstein, Über die von der molekularkinetischen Theorie der Wärme geforderte Bewegung von in ruhenden Flüssigkeiten suspendierten Teilchen. Annalen der Physik 17, 549-560 (1905).
33. Edelman RR, Gaa J, Wedeen VJ, Loh E, Hare JM, Prasad P and Li W. *In vivo* measurement of water diffusion in the human heart. Magn Reson Med 1994;32:423-428.
34. Hahn EL. Spin echoes. Physical Review 1950; 30:580-594.
35. Carr H, Purcell EM. Effects of diffusion on free precession in NMR experiments. Physical Review 1954; 94:630-638.
36. Torrey HC. Bloch equations with diffusion terms. Physical Review 1956; 104:563-565.
37. Bloch F. Physical Review 1946; 70:460.
38. Stejskal EO, Tanner JE. Spin diffusion measurements: spin echoes in the presence of a time-dependent field gradient. Journal of Chemical Physics 1964; 42:288-292.
39. Callaghan P. Principles of nuclear magnetic resonance microscopy. Oxford: Clarendon Press, 1991.
40. Murphy J, Doane J. An NMR measurement of the diffusion anisotropy in a nematic liquid crystals. Molecular Crystal and Liquid Crystal 1971; 13:93-95.
41. Kruger G, Spiesecke H. Anisotropy of the diffusion coefficient in nematic liquid solutions measured by NMR techniques. Zeitschrift fur Naturforschung A (Astrophysik, physik und Physikalische Chemie) 1973; 28a:964-967.

42. Ukleja P, Doane J. The anisotropy of self-diffusion in the lamellar phase (using NMR). . Ordering in Two Dimensions. Lake Geneva, WI, USA, 1980.
43. Callaghan P, LeGros M, Pinder D. The measurement of diffusion using deuterium pulsed field gradient nuclear magnetic resonance. Journal of Chemical Physics 1983; 79:6372-6381.
44. Wesbey GE, Moseley ME, Ehman RL. Translational molecular self-diffusion in magnetic resonance imaging. II. Measurement of the self-diffusion coefficient. Investigative Radiology 1984; 19(6):491-498.
45. Finch E, Harmon J, Muller B. Pulsed NMR measurement of the diffusion constant of water in muscle. Arch Biochem Biophys 1971; 147:299-310.
46. Doran M, Hajnal JV, Van Bruggen N, King MD, Young IR, Bydder GM. Normal and abnormal white matter tracts shown by MR imaging using directional diffusion weighted sequences. Journal of Computer-Assissted Tomography 1990; 14:865-873.
47. Cleveland GG, Chang DC, Hazlewood CF, Rorschach HE. Nuclear magnetic resonance measurement of skeletal muscle: anisotropy of the diffusion coefficient of the intracellular water. Biophysical Journal 1976; 16:1043-1053.
48. Garrido L, Wedeen VJ, Spencer U, Kantor H. Anisotropy of water diffusion in the myocardium of the rat. Circulation Research 1994; 74:789-793.
49. Yang Y, Shimony JS, Xu S, Gulani V, Dawson MJ, Lauterbur PC. A sequence for measurement of anisotropic diffusion by projection reconstruction imaging and its application to skeletal and smooth muscle. . Proceedings of Society of Magnetic Resonance. Berkeley, California: Society of Magnetic Resonance, 1994; 1036.
50. Muller MF, Prasad PV, Bimmler D, Kaiser A, Edelman RR. Functional imaging of the kidney by means of measurement of the apparent diffusion coefficient. Radiology 1994:711-715.
51. Wu JC, Wong EC, Arrindell EL, Simons KB, Jesmanowicz A, Hyde JS. *In vivo* determination of the anisotropic diffusion of water and the T1 and T2 times in the rabbit lens by high-resolution magnetic resonance imaging. Invest. Ophthalmol. Vis. Sci. 1993; 34:2151-2158.
52. Moseley ME, Cohen Y, Kucharczyk J, Mintorovitch J, Asgari HS, Wendland MR, Tsuruda J, Norman D. Diffusion-weighted MR imaging of anisotropic water diffusion in cat central nervous system. Radiology 1990; 176:439-446.

53. Douek P, Turner R, Pekar J, Patronas N, LeBihan D. MR color mapping of myelin fiber orientation. Journal of Computer-Assissted Tomography 1991; 15:923-929.
54. Basser PJ, Mattiello J, LeBihan D. MR diffusion tensor spectroscopy and imaging. Biophysical Journal 1994; 66:259-267.
55. Scollan DF, Holmes A, Winslow R, and Forder J. Histological validation of myocardium microstructure obtained from diffusion tensor magnetic resonance imaging. Am J Physiol 1998;275 (Heart Circ Physiol 44):H2308-H2318.
56. Tseng WI, Reese TG, Smith RN, Halprin E, Wedeen VJ. Histologic correlation of myocardial diffusion tensor MRI: fibers and sheets both contribute. In: Proc ISMRM, 18th Annual Meeting. Philadelphia, 1999. p. 26.
57. Reese TG, Wedeen VJ, Weisskoff RM. Measuring diffusion in the presence of material strain. J. Magn Reson B 1996; August, in press.
58. Reese TG, Weisskoff RM, Smith RN, Rosen BR, Dinsmore RE and Wedeen VJ. Imaging myocardial fiber architecture *in vivo* with magnetic resonance. Magn Reson Med 1995;34:786-791.
59. Tseng WI, Reese TG, Weisskoff RM and Wedeen VJ. Cardiac diffusion tensor MRI *in vivo* without strain correction. Magn Reson Med 1999;42:393-403.
60. Purcell E, Torrey H, Pound R. Physical Review 1946; 69:37.
61. Suryan G. Proc. Indian Acad. Sci., 1951.
62. Singer JR. Blood flow rates by nuclear magnetic measurements. Science 1959; 130:1652-1653.
63. Morse OC, Singer JR. Blood velocity measurements in intact subjects. Science 1970; 170:440-441.
64. Zerhouni EA, Parish DM, Rogers WJ, Yang A, Shapiro E. Human Heart: tagging with MR imaging - a method for noninvasive assessment of myocardial motion. Radiology 1988; 169:59-63.
65. Young AA, Axel L. Three-dimensional motion and deformation of the heart wall: estimation with spatial modulation of magneitzation - a model based approach. Radiology 1992; 185:241-247.

66. Azhari H, Weiss J, Rogers W, Siu C, Zerhouni E, Shapiro E. Non-invasive quantification of principal strains in normal canine hearts using tagged MRI images in 3D. American Journal of Physiology 1993; 264:H205-H216.

67. Axel L. Noninvasive measurement of cardiac strain with MRI. Adv Exp Med Biol 1997; 430:249-256.

68. Rademakers F, Bulchalter M, Rogers W, Zerhouni E, Weisfeldt M, Weiss J, Shapiro E. Dissociation between left ventricular untwisting and filling accentuation by catesholamines. Circulation 1992; 85:1572-1581.

69. Young AA, Kramer CM, Ferrari VA, Axel L, Reichek N. Three dimensional ventricular deformation in hypertrophic cardiomyopathy. Circulation 1994; 90:854-867.

70. Marcus J, Gotte M, Rossum A, Kuijer J, Heethaar R, Axel L, Visser C. Myocardial function in infarcted and remote regions early after infarction in man: assessment by megnetic resonance tagging and strain analysis. Magnetic Resonance in Medicine 1997; 38:803-810.

71. Carr H, Purcell EM. Effects of diffusion on free precession in NMR experiments. Physical Review 1954; 94:630-638.

72. Hahn EL. Detection of sea-water motion by nuclear precession. Journal of geophysical research 1960; 65:776-777.

73. Moran PR. A flow velocity zeugmatographic interlace for NMR imaging in humans. Magnetic Resonance Imaging 1982; 1:197-203.

74. Moran PR, Moran RA, Karstaedt N. Verification and evaluation of internal flow and motion: true magnetic resonance imaging by the phase gradient modulation method. Radiology 1985; 154:433-441.

75. van Dijk P. Direct cardiac NMR imaging of heart wall and blood flow velocity. Journal of Computer Assisted Tomography 1984; 8:429-436.

76. Zhu Y, Drangova M, Pelc NJ. Estimation of deformation gradient from cine-PC velocity data. IEEE Trans Med Imaging 1997;16:840-851.

77. Zhu Y, Drangova M, Pelc NJ. Fourier tracking of myocardial motion using cine-PC data. Magn Reson Med 1996;35:471-480.

78. Zhu Y, Pelc NJ. Three-dimensional motion tracking with volumetric phase contrast CMR velocity imaging. J Magn Reson Imaging 1999;9:111-118.

79. Wedeen VJ. Magnetic resonance imaging of myocardium kinematics: technique to detect, localize and quantify, the strain rates of the active human myocardium. Magn Reson Med 1992;27:52-67.

80. Tseng WI, Reese TG, Weisskoff RM, Brady TJ, Wedeen VJ. Myocardial fiber shortening in humans: initial results of MR imaging. Radiology 2000;216:128-139.

81. Basser PJ, Mattiello J, and LeBihan D, MR imaging of fiber-tract direction and diffusion in anisotropic tissues. In: Proc SMRM, 12th Annual Meeting, New York, 1993. p 288.

82. Wedeen VJ, Weisskoff RM, Reese TG, Beache GM, Poncelet BP, Rosen BR, and Dinsmore RE. Motionless movies of myocardial strain-rates using stimulated echoes. Magn Reson Med 1995;33(3):401-408.

83. Stepisnik J. Measuring and imaging flow by NMR. Prog NMR Spectrosc 1985;17:187-209.

84. Nalcioglu O, Moran PR. Characterization of turbulent flow by NMR imaging. In: International Symposium on Turbulent Shear Flows (6th), Toulouse, France. 1987.

85. Callaghan PT, Stepisnik J. Frequency-domain analysis of spin motion using modulated-gradient NMR. J Magn Reson 1995;117:118-122..

86. Callaghan PT, Stepisnik J. Generalized analysis of motion using magnetic field gradients. Advances in Magnetic and Optical Resonance 1996;19: 325-388.

87. Muthupillair R, Lomas DJ, Rossman PJ, Greenleaf JF, Manduca A, Ehman RL. Magnetic-resonance elastography by direct visualization of propagating acoustic strain waves. Science 1995;269(5232):1854-1857.

88. Streeter DD Jr, and Hanna WT. Engineering mechanics for successive states in canine left ventricular myocardium. Circ Res 1973;33:654-656.

89. Smaill BH, Hunter PJ. Structure and function of the diastolic heart: material properties of passive myocardium. In: Class L, Hunter PJ, McCulloch A, eds. Theory of heart. New York: Springer-Verlag; 1991. p 1-29.

90. Hunter PJ, Nielsen PMF, Smaill BH, LeGrice IJ, Hunter IW. An anatomical heart model with applications to myocardial activation and ventricular mechanics. In: Pilkington TC, Loftis B, Thompson JF, Woo SL-Y, Palmer TC, Budinger TF, eds. High Performance Computing in Biomedical Research. Boca Raton, Fla: CRC press; 1993. p 3-26.

91. Meier GD, Ziskin MC, Santamore WP, and Bove AA. Kinematics of the beating heart. IEEE Trans Biomed Eng 1980;27:319-329.

92. Pelc NJ, Bernstein MA, Shimakawa A, Glover GH. Encoding strategies for three-direction phase-contrast MR imaging of flow. J Magn Reson Imaging 1991;1:405-413.

93. Kondo H, Masuyama T, Ishihara K, Mano T, Yamamoto K, Naito J, Nagano R, Kishimoto S, Tanouchi J, Hori M, et al. Digital suntraction high-frame-rate echocardiography in detecting delayed onset of regional left ventricular relaxation in ischemic heart disease. Circulation 1995;91:304-312.

94. Beyar R, Yin FC, Hausknecht M, Weisfeldt ML, Kass DA. Dependence of left ventricular twist-radial shortening relations on cardiac cycle phase. Am J Physiol 1989;257(4 Pt 2):H1119-H1126.

95. Wedeen VJ, Weisskoff RM, Poncelet BP. MRI signal void due to in-plane motion is all-or-none. Magn Reson Med 1994;32:116-120.

96. Wedeen VJ, Poncelet BP. MRI of brain parenchymal motion. In: Grant DM, Harris RK, editors. Encyclopedia of nuclear magnetic resonance. New York: John Wiley and Sons; 1996.

97. Feinberg DA, Mark AS. Human brain motion and cerebrospinal fluid circulation demonstrated with MR velocity imaging. Radiology 1987;163:793-799.

98. Poncelet BP, Wedeen VJ, Weisskoff RM, Cohen MS. Brain parenchyma motion: measurement with cine echo-planar MR imaging. Radiology 1992;185:645-651.

99. Enzmann DR, Pelc NJ. Brain motion: measurement with phase-contrast MR imaging. Radiology 1992; 185:653-660.

100. Sodickson DK, Manning WJ. Simultaneous acquisition of spatial harmonics (SMASH): fast imaging with radiofrequency coil arrays. Magn Reson Med 1997;38:591-603.

101. Pruessmann KP, Weiger M, Scheidegger MB, Boesiger P. SENSE: sensitivity encoding for fast MRI. Magn Reson Med 1999;42:952-962.

102. Osman NF, Kerwin WS, Mc Veigh ER, Prince JL. Cardiac motion tracking using CINE harmmoic phase (HARP) magnetic resonance imaging. Magn Reson Med 1999;42:1048-1060.

103. Stuber M, Fischer SE, Scheidegger MB, Boesiger P. Toward high-resolution myocardial tagging.

104. Hort W. Untersuchunged uber die Muskelfaserdehnung und das Gefuge des Myokards in der rechten Herzkammerwand des Meerschweinchens. Virchow Arch. Pathol. Anat. Physiol. Klin. Med. 329:694-731, 1957.

105. Dou JG, Reese TG, Tseng WI, Wedeen VJ. Cardiac diffusion MRI without motion effects. Magn Reson Med. 2002;48:105-114.

106. Basser PJ, Pierpaoli C. A simplified method to measure the diffusion tensor from seven MR images. Magn. Reson. Med. 1998;39:928-934.

107. Pauschinger M, Knopf D, Petschauer S, Doerner A, Poller W, Schwimmbeck PL, Kuhl U, Schultheiss HP. Dilated cardiomyopathy is associated with significant changes in collegen type I/III ratio. Circulation. 1999;99 (21):2750-6.

108. Neumann T, Vollmer A, Schaffner T, Hess OM, Heusch G. Diastolic dysfunction and collagen structure in canine pacing-induced heart failure. J Mol Cell Cardiol. 1999;31(1):179-92.

109. Tyagi SC. Extracellular matrix dynamics in heart failure: a prospect for gene therapy. J Cell Biochem. 1998;68 (4):403-10.

110. Masutomo K, Makino N, Sugano M, Miyamoto S, Hata T, Yanaga T. Extracellular matrix regulation in the development of Syrian cardiomyopathic Bio 14.6 and Bio 53.58 hamsters. J Mol Cell Cardiol. 1999:31 (9):1607-15.

111. Mujumdar VS, Tyagi SC. Temporal regulation of extracellular matrix components in transition from compensatory hypertrophy to decompensatory heart failure. J Hypertens. 1999;17 (2):261-70

112. Lunkenheimer PP, Redmann K, Cryer CW, Richter RD, Niederer P, Whimster WF, Torrent-Guasp F. The difficult access to morphology of the heart: clinical implications. Technology and Health Care 1994; 2:155-173.